EPA/600/R-12/547 | June 2012 | www.epa.gov/research

United States Environmental Protection Agency

Evaluation of the Seismic Characterization of Select Engineered Nanoparticles in Saturated Glass Beads

RESEARCH AND DEVELOPMENT

Evaluation of the Seismic Characterization of Select Engineered Nanoparticles in Saturated Glass Beads

Mohamed Nihad Rajabdeen[1]
Barbara Luke[1]
D. Dale Werkema Jr.[2]

[1]Department of Civil and Environmental Engineering
University of Nevada – Las Vegas
Las Vegas, NV 89119

[2]U.S. Environmental Protection Agency
Office of Research and Development
National Exposure Research Laboratory
Environmental Sciences Division
Las Vegas, NV 89119

U.S. Environmental Protection Agency
Office of Research and Development
Washington, DC 20460

EVALUATION OF THE SEISMIC CHARACTERIZATION OF SELECT ENGINEERED NANOPARTICLES IN SATURATED GLASS BEADS

Mohamed Nihad Rajabdeen[1], Barbara Luke[1], D. Dale Werkema Jr. [2]

1. Department of Civil and Environmental Engineering, University of Nevada – Las Vegas.
2. U.S. EPA, Office of Research and Development, National Exposure Research Laboratory, Environmental Sciences Division, Las Vegas, NV.

EXECUTIVE SUMMARY

A laboratory testing apparatus was developed for the study of seismic body wave propagation through nanoparticles dispersed in pore fluid that is essentially saturating glass beads. First, the responses of water-saturated glass bead specimens were studied to establish baseline signatures. Then the seismic responses in the presence of engineered nanoparticles of various concentrations dispersed in the pore fluid of the specimen chamber were studied to observe variances from baseline.

The testing apparatus incorporates piezoceramic bender elements to actuate and receive seismic body waves through a cylindrical column filled with glass beads and back-saturated at ambient pressure with liquid. The system was calibrated in air, water, and water-saturated glass beads. System repeatability was checked after the system was saturated and flushed once to soak and seat the beads. The water-saturated glass bead specimens were tested for compression, shear, and spectral response, from which baseline signatures were established. Criteria were proposed to evaluate the detectability of nanoparticle dispersions.

Nanoparticle dispersions of zinc oxide (nZnO), titanium dioxide ($nTiO_2$), and silver (nAg) were tested. The testing system showed itself to be capable of registering subtle changes in the response caused by varying consolidation states of the glass beads and pore fluid content. The presence of nZnO was detectable at 0.03%, 0.3%, and 2.7% concentrations for all the test methods except compression wave arrivals; nAg was detectable at 3.7% concentration only by compression wave amplitude and spectral

response and $nTiO_2$ showed only subtle detectability for spectral response at 4.9% concentration.

TABLE OF CONTENTS

LIST OF TABLES

LIST OF FIGURES

CHAPTER 1

INTRODUCTION

This study was part of a larger project concerning the detection of nanoparticles used in engineered nanomaterials as they disperse throughout the environment. This study addresses the potential for seismic methods to be implemented in detecting such nanoparticles in a natural environment. A testing system was built and calibrated in air, water, and essentially saturated glass beads. Testing was then conducted for the presence of various types of nanoparticles dispersed in the pore fluid of essentially saturated glass bead specimens.

1.1 Necessity of the Research

Nanotechnology is the manipulation and control of substances on the nanoscale. The nanoscale measures particles in nanometers, where one nanometer is one billionth of a meter. When particles from the nanoscale are compared to particles of the same material on the macro-scale, the physical and chemical properties often differ. This phenomenon enables new applications, processes and technology (National Nanotechnology Initiative, 2009).

According to the National Nanotechnology Initiative (2009), three types of nanoparticles exist: naturally occurring; incidental; and engineered. Naturally occurring nanoparticles for example, exist in the human body, which uses them to control many systems and processes. An example of this is hemoglobin, which is a protein nanoparticle

that is used to transport oxygen. Incidental nanoparticles are created as by-products of processes such as combustion and other industrial activities. When particles are purposefully manufactured on the nanoscale, they are known as engineered nanoparticles.

Nanotechnology is a growing industry which has the potential of improving the standard of living and benefitting society. Industries such as medicine, energy, and information technology are all currently exploring possibilities with nanoparticles (National Nanotechnology Initiative, 2009). As more industries start utilizing engineered nanoparticles, they have the potential to be released into the environment by various processes. The impacts of engineered nanoparticles on human health and the environment are unknown due to the fact that applications are novel and limited research has been conducted. This is where the primary environmental concern with engineered nanoparticles comes into play. There are no current proven methods of detecting the fate and transport of nanoparticles in the subsurface (Conlon, 2009). For this reason, new testing practices and detection techniques have to be explored.

Williams et al. (2005) used a column containing sand to monitor the effects of microbial activity on metal ions over a number of days. The microbial activities led to the development of nanoparticles along the sand surfaces and in assemblages formed within the pore spaces. Seismic and electrical techniques were applied to observe variances from initial readings caused by the development and presence of the nanoparticles. The authors found that subtle changes in grain size, consolidation state, and type of pore fluid saturation of the material can alter the velocity and amplitude of the seismic response to varying degrees. The results from the monitoring efforts by the authors led to development of this research in which a testing system is developed and optimized to

identify the presence of nanoparticles in essentially saturated glass beads by seismic methods.

1.2 Research Objectives

This project comprises two research objectives; first to design, build and optimize a laboratory seismic testing system for essentially saturated glass beads, and second to use the system to explore the seismic response of select nanoparticle dispersions in an essentially saturated granular matrix.

1.3 Research Questions

Three research questions are addressed in this study:

1. Which type of seismic waveform and function is most suitable for testing?
2. To what degree are test results repeatable?
3. Can the presence of select nanoparticle dispersions be detected by variations in the seismic response?

1.4 Report contents

Chapter 2 presents test column design criteria, and test system components and layout. It also addresses the composition of piezoceramic elements which were used to actuate and receive seismic energy, and how they were prepared for this research. Chapter 3 addresses signal processing, complications caused by near-field effects, and the

potential sources of error with signal interpretation. Chapter 4 reviews previous research efforts that have utilized bender elements, and presents suitable test methods for this research. Chapter 5 presents the calibration of the system in air and water. Chapter 6 presents the methods used to prepare the glass bead specimens. Chapter 7 presents the calibration of the system using water-saturated glass beads. Chapter 8 presents the testing of nanoparticle dispersions. Chapter 9 presents the conclusions and recommendations. Chapter 9 also presents new research questions that arose from this study.

CHAPTER 2

TESTING APPARATUS

This chapter addresses the composition of piezoceramic elements, how they actuate and receive seismic energy, and how they were prepared for this study. Also presented are the column design criteria, test system layout and other components of the testing system.

2.1 Piezoceramic Bender Elements

Piezoceramic bender elements are transducers that can be used interchangeably to either generate or receive seismic body waves. The bender elements convert electrical energy to mechanical energy and vice versa. Bender elements were first used to measure shear-wave velocity of clay specimens in 1978 by Shirley and Hampton (Clayton et al, 2004). From 1978 until today, piezoceramic bender elements have been the choice of transducer for use by many researchers when mechanical properties of sediments were required in the laboratory (Dyvik and Olsen, 1991).

Bender elements are also utilized because of their good coupling capability between the transducer and testing media (Lee and Santamarina, 2005) to measure variances in response as seismic energy is propagated through saturated granular media. Lee and Santamarina (2005) carried out a thorough study that addressed bender element installations, prevention of electromagnetic coupling, directivity of transmitted energy, resonance condition, detection of first arrival, and near-field effects. Da Fonseca et al.

(2008) list the methods available for testing with bender elements and provide advice for choosing the most suitable.

2.2 How Piezoceramics Work

A piezoceramic material generates and receives sound and voltage by the phenomenon known as the piezoelectric effect (e.g., Piezo Systems, 2009). Piezoceramic crystals have an asymmetrical lattice structure that leads to polarization densities when the crystal undergoes mechanical deformation (flexing; Birkholz, 1995). This in turn leads to a voltage difference being created across the crystal. Similarly, if a voltage difference were applied on opposing faces of the crystal, this would cause the crystal to flex.

This principle applies when piezoceramic elements are placed within test specimens in the following manner: as seismic body waves (i.e. S- and P-waves) strike the surface of the piezoceramic, the piezoceramic element flexes and this creates a voltage difference that can be captured electronically. When a voltage difference is applied across a piezoceramic bender element that is embedded within a granular specimen, the element vibrates, creating body waves that travel through the specimen (Blewett et al., 1999). Bender elements generate both shear (S) and compression (P) waves when they actuate in granular media, where S-waves are generated in the form of a frontal lobe and the P-waves as side lobes with respect to the bender element (Lee and Santamarina, 2005).

2.3 Bender Element Configuration

The bender elements were purchased from Piezo Systems Inc., and were 2-piezo layer transducers, made with PSI-5A4E piezoceramic, parallel-poled, using nickel electrodes and brass center reinforcement. The elements were 12.7 mm square and 0.5 mm thick. Two important parameters for the source bender elements are the free deflection and the maximum force generated for the voltage applied. An important parameter for the receiver bender element is the voltage generated by the force applied (Leong et al., 2005).

The force generated by the source and the voltage generated by the receiver are dependent upon the width of the bender elements. As the width increases, the force generated at the source increases and the voltage generated at the receiver decreases. Widths of bender elements typically range from 6 to 15 mm (Leong et al., 2005).

The free deflection and output voltage of the bender element for a given applied voltage is dependent upon the cantilever length. Keeping the cantilever short makes the resonance frequency of the bender element dependent on the bender element properties and the anchoring properties, whereas a long cantilever would make the resonance frequency dependent on the sediment properties (Lee and Santamarina, 2005). A shorter cantilever yields a higher resonant frequency and a shorter wavelength at resonance. A shorter cantilever length is preferred in this study so that resonant frequency will remain relatively constant for all testing media. The cantilever length used was 4.2 mm which is 1/3 the total length of the bender element.

Bender elements are high impedance devices and can therefore short electrically when exposed to moisture (Dyvik and Madshus, 1986). Figures 2.1 – 2.3 show the

process by which the bender elements were cased and water proofed: they were coated with a thin layer of polyurethane, then painted over with silver paint and carefully potted in vinyl caps using epoxy. The silver conductive paint coating is applied to help properly ground the bender element to minimize electrical crosstalk (Wang et al., 2007). Professor Carlos Santamarina and his colleagues at Georgia Tech recommended the waterproof polyurethane coating for better actuation and reception of signals. If the bender elements produce sound and have the resistivity of an open circuit (or very high resistance, on the order of Mega-Ohms) after the polyurethane and silver coatings are applied, they are properly prepared (Changho Lee, personal communication, 9/15/08). The final product of the bender elements potted with epoxy in vinyl caps was fixed within the testing system by applying RTV silicone. The silicone was applied on the outside of the vinyl cap of the potted bender element, which was then placed within the test system. Silicone was chosen due to its inert and waterproof properties (Zhihai et al., 2008). The different materials used for preparing and holding the bender element in the test system create impedance traps that prevent waves generated at the anchor from travelling through the structure of the test system to the receiver, and therefore causing error.

2.4 Column Testing System Design

The testing column was constructed from a clear PVC tube of 15.2 cm inside diameter (D), mounted on a PVC base, with an acrylic top cap made to fit snugly inside the column (Fig. 2.4). The top cap was fitted with a rubber O-ring. The base was mounted on four column supports, and had an inlet valve attached to it. The purpose of the inlet

was for pluming fluids into the column by gravity. The top cap had an outlet for drainage of excess liquid or air from the specimen. A handle was attached to the top cap.

The column geometry is comparable to that of an oedometer, which is an instrument used to measure the rate and amount of consolidation of a specimen as pressure is applied; however, the functions of an oedometer and our testing apparatus are different. Wave travel paths can be compared between the two systems. Apart from oedometers, other common test systems that have been used with bender element testing are triaxial testing systems and large tanks with the bender elements placed on stands within the tank.

When bender element testing is incorporated in an oedometer, the tip-to-tip distance between bender elements (L) and not the full height of the specimen must be taken as the travel path length (Fig. 2.4; Dyvik and Madshus, 1986). The dimensions of the testing system were selected considering three main design criteria as presented below.

The first criterion addressed the ratio of the column inner diameter (D) to the tip-to-tip distance (L) of the bender elements; the D:L ratio. Some D:L ratios used in previous research with oedometers modified for bender element testing are presented in Table 2.1. The range considered in this body of research was: $4.2 > D:L > 2.2$.

The second criterion addressed the relationship between (L) and the wavelength (λ) of the actuated signal; this relationship addresses the potential for P-wave coupling with S-wave arrivals (so-called “near-field effects”). According to Wang et al. (2007), this coupling effect can be avoided by configuring the test cell so that: $L:\lambda > 2$.

The third criterion was to use the shortest acceptable travel path length for the waves. This criterion was used to minimize signal attenuation between the source and the

receiver and to keep the volume of the testing system to a minimum in order to minimize the quantity of experimental treatment used, to control costs and minimize waste.

For the testing system, the only set parameter out of the two ratios (D:L and L:λ) was the diameter (D). The (L) value could be varied because the top cap was mobile in the vertical direction and (λ) could be adjusted by varying the actuation frequency of the source signal. The L value chosen for testing is presented in chapter 5. Calibration of the column in air and water was carried out approximately at the resonance frequency of the potted bender elements, because this improves the signal to noise ratio (Wang et al., 2007). For testing in saturated granular media, depending on whether P-waves or S-waves were targeted, the frequency and therefore wavelength parameters were adjusted within the criteria provided above, until the clearest signals were received.

2.5 Testing Layout

The testing system layout was comprised of the mechanical test cell, electrical components and a fluid system. Figures 2.5 through 2.7 illustrate the components.

2.6 Equipment

Equipment ancillary to the test column included:

- Function generator: Agilent 33220A
- Linear amplifier: Piezo systems Inc., EPA 104
- Bender elements: Piezo Systems Inc., described previously

- Filter-Amplifier: Krohn-Hite, 3364
- Signal analyzer: Dataphysics SignalCalc Dynamic Signal Analyzer
- Sonicator: Branson 5510
- Peristaltic pump: Ismatec C.P. 78023-10
- Digital caliper: Cen-tech 47257 (not shown in figures)

The process of actuating, transmitting and receiving a signal is as follows (Fig. 2.5 and 2.6):

- The source signal is generated via function generator
- The signal is amplified through a linear amplifier to increase signal to noise ratio
- The amplified signal is transmitted to the source bender element
- The source bender element converts the electrical signal to a mechanical wave
- The actuated mechanical wave is transmitted through the specimen to the receiver bender element
- The receiver bender element converts the mechanical wave to an electrical signal
- The electrical signal is filtered to reduce noise, and displayed and recorded on a digital signal analyzer

The fluid system layout (Fig. 2.7) is described in chapter 8.

Table 2.1. Key dimensions of oedometers modified for bender element testing, compared against dimensions of cell for this study

Reference	Specimen diameter (D, mm)	Tip-to-tip distance (L, mm)	D : L
Dyvik and Olsen (1991)	66.7	16	4.2
Zeng and Ni (1998)	152.4	68.6	2.2
Lee and Santamarina (2005)	70	32	2.2
Lee and Santamarina (2005)	100	19.8	5.1
Lee et al. (2007)	74	29	2.6
This study	**152.4**	**62.5**	**2.4**

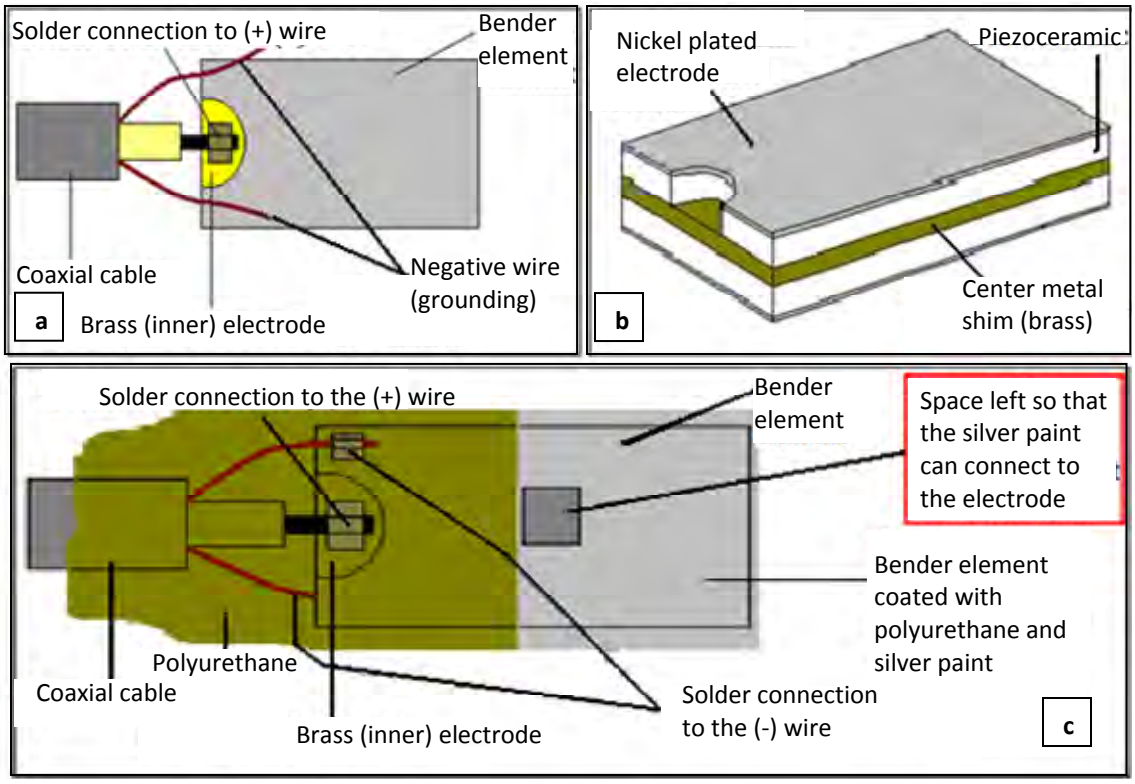

Figure 2.1. Bender element, waterproofing and grounding process

a: Mounted piezoceramic bender element with coaxial cable wiring
b: Isometric view of piezoceramic bender element showing layering
c: Bender element coated with polyurethane and high-purity silver paint for waterproofing and grounding.

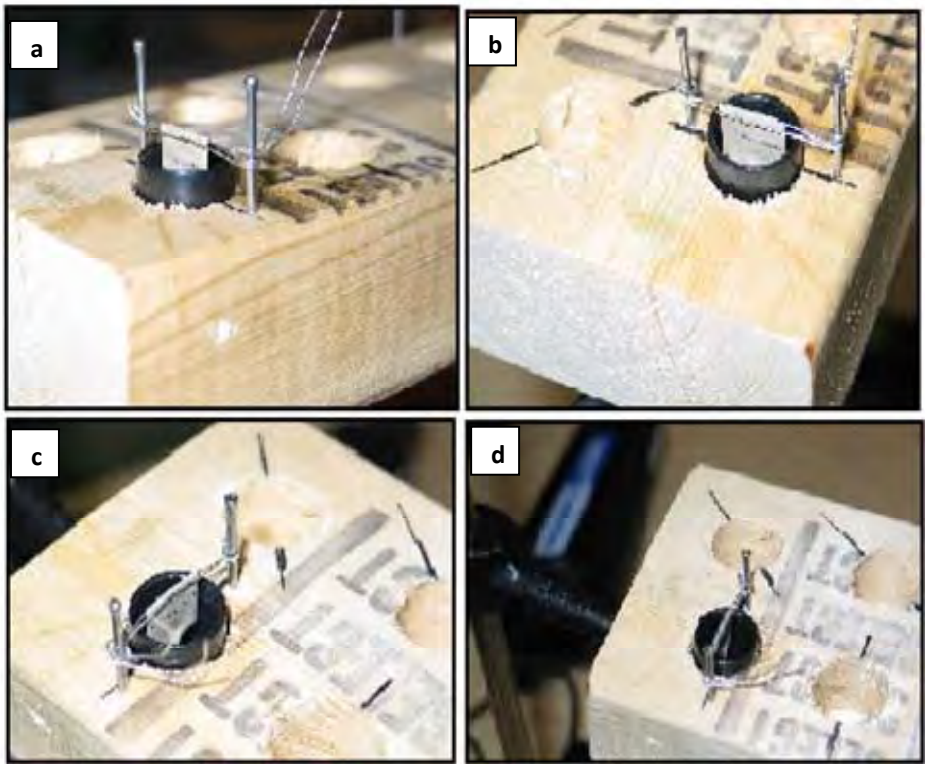

Figure 2.2. Bender element placed in a vinyl cap, at the required depth, and set in a wooden block mold, shown in four different views (a, b, c and d). The mold supported curing of epoxy used for anchoring bender element in the vinyl cap.

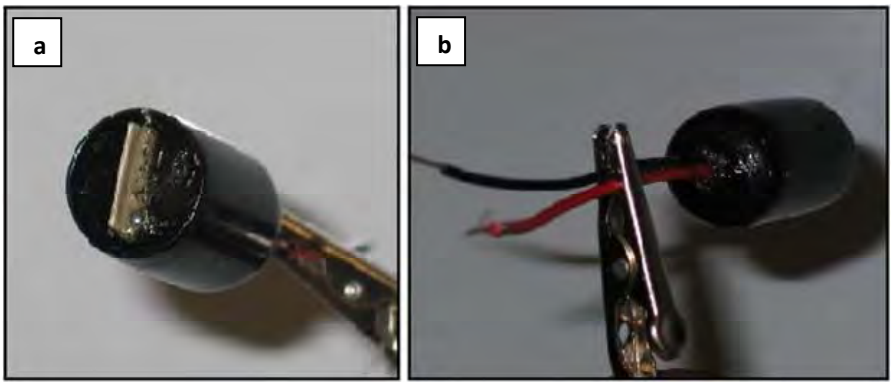

Figure 2.3. A bender element cased in a vinyl cap with epoxy

a: front view
b: rear view

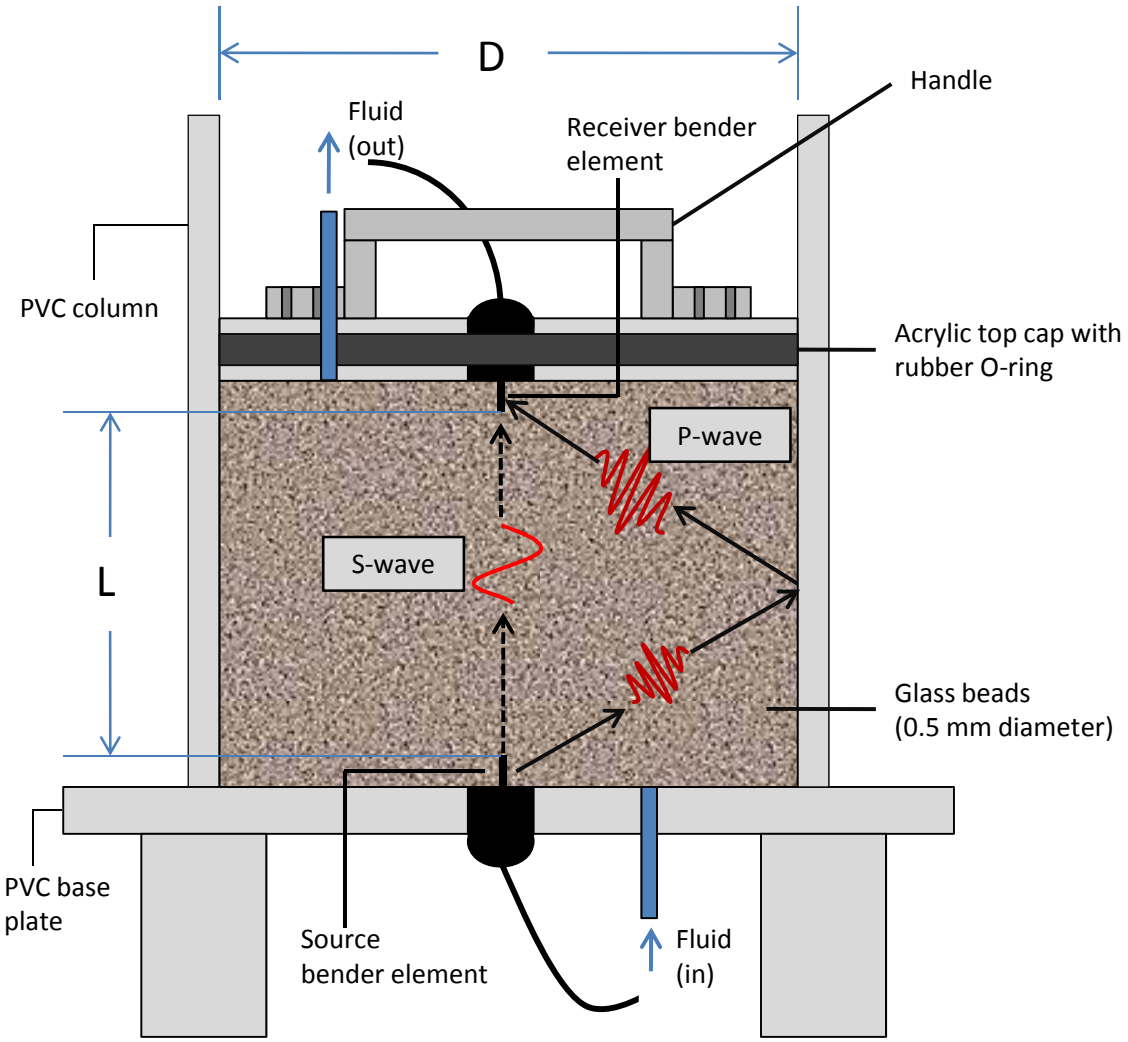

Figure 2.4. Schematic cross-section of test column showing anticipated P- and S-wave travel paths; D: Column inner diameter; L: Tip-to-tip distance.

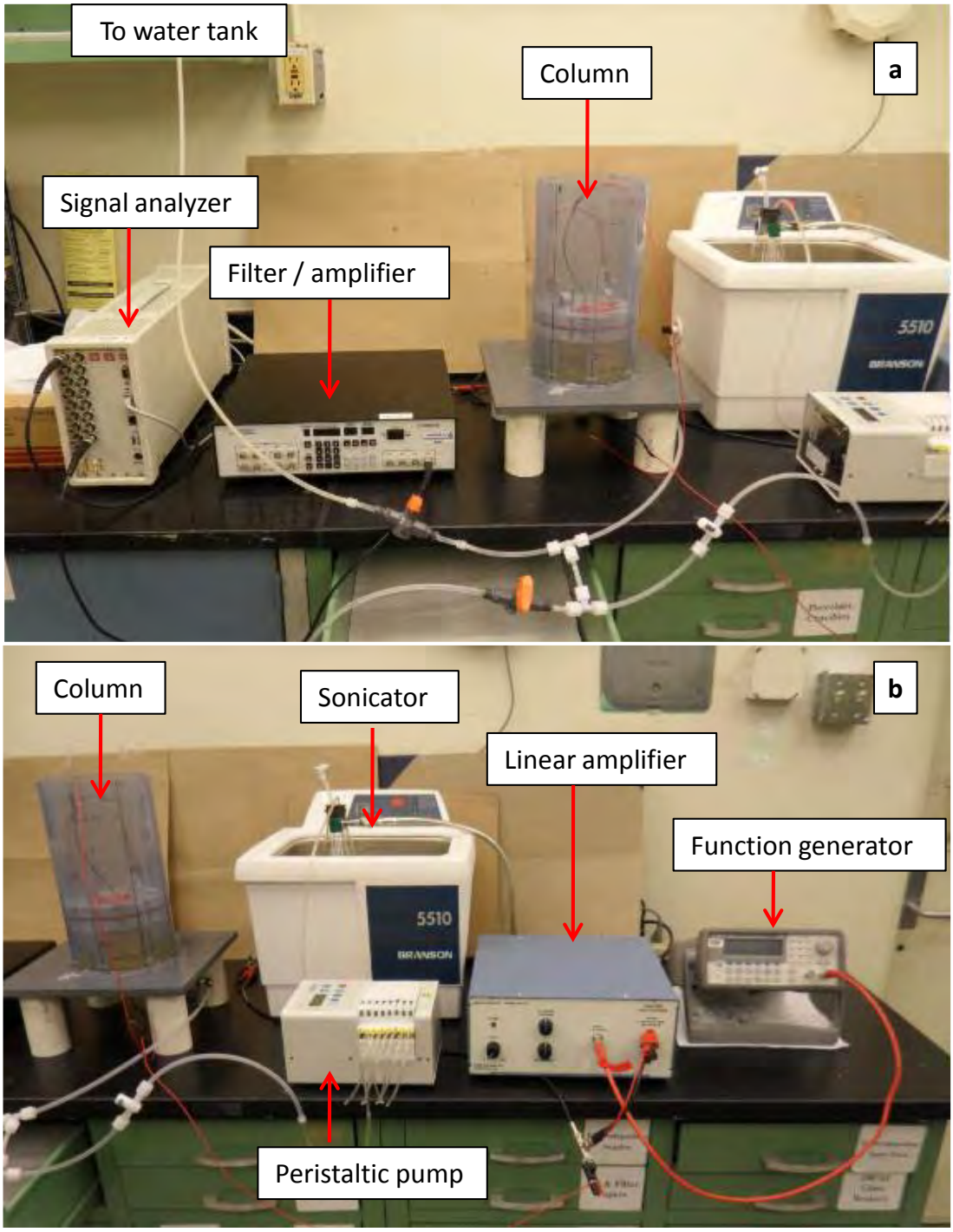

Figure 2.5. Complete testing system layout, shown in two halves, left (a) to right (b); equipment described in section 2.6. The nanoparticle tank is in the sonicator.

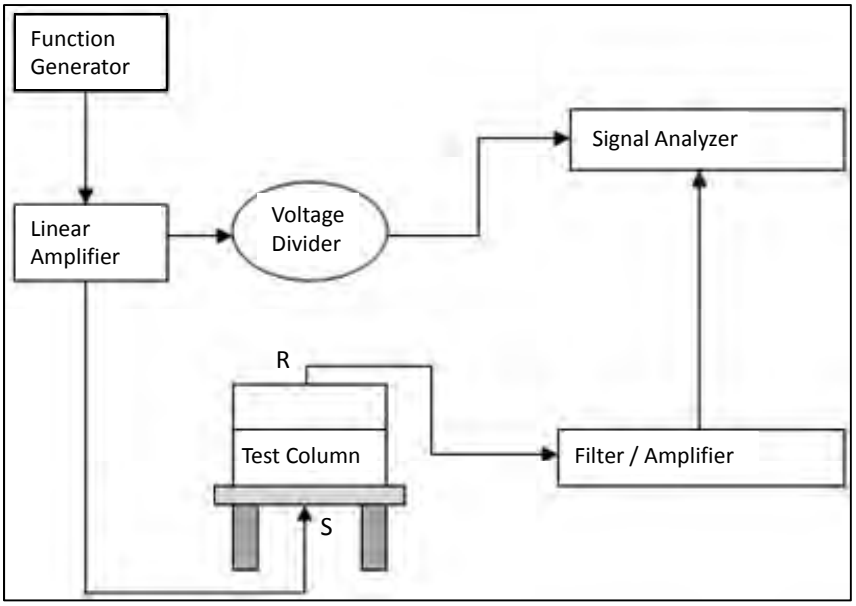

Figure 2.6. Electrical component layout of the testing system; connections between equipment were made using BNC cables; soldered coaxial cable connections to the bender elements were made as shown in Fig.2.1. S and R represent source and receiver bender elements, respectively.

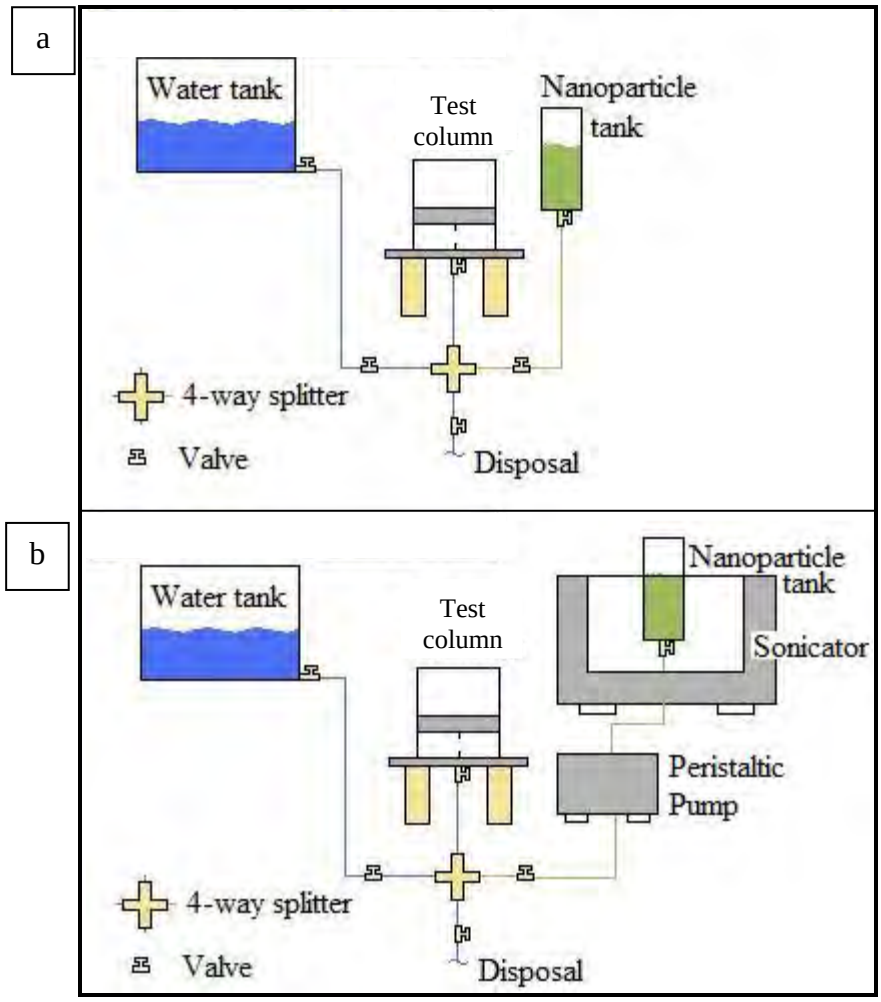

Figure 2.7. Fluid component of the testing system: layout

a: Pluming system used for testing nano-oxides
b: Pluming system used for testing nano-metals

CHAPTER 3

SIGNAL PROCESSING

This chapter outlines how the source signal was chosen, complications posed by near-field effects, other potential sources of error with signal interpretation, and the signal processing required to receive clear signals.

3.1 Source Signal

Received signals are distorted versions of the input signal due to the effects of transfer functions. The shape of the input signal is important in reducing unwanted effects (Arroyo et al., 2003). The most commonly used source waves with bender elements are sine and square waves (Leong et al., 2005).

Leong et al. (2005) used bender elements to determine the shear wave velocities of sand, mudstone, and kaolin specimens. The results were examined with respect to characteristics of the waveform type, magnitude, and frequency applied to the transmitter bender elements. The two types of waveforms considered were square waves and sine waves. The authors showed that when square waves are used as the source signal, the received signals do not resemble the transmitted signal because the rise time of a square wave is practically zero which corresponds to an infinite frequency, leading to uncertainty in arrival time. When sine waves were used as the source, there was less ambiguity in the arrival times of the received signals when compared with those of the square wave. The authors state that uncertainty in the interpretation of bender element

tests arises due to the quality of the received signal and for this reason a sinusoidal input is the preferred choice.

Jovičić et al. (1996) also carried out a study to determine whether sine or square waves were more appropriate to record the shear wave arrivals. The authors found that sinusoidal waves were the simplest way to obtain a bender element output that may be interpreted objectively, since the actuation frequency can be adjusted according to the required travel distance and test specimen stiffness to avoid near-field effects (described below). The authors claimed that square waves will always have near-field effects because they are comprised of a spectrum of frequencies, which make the square waves complex to analyze and near-field effects difficult to nullify.

Arroyo et al. (2003) also studied near-field effects with bender elements by analyzing multiple source waves. The amplitude of the near-field effects caused by sine waves was 10% of the output peak signal (S-wave) and that of the near-field effects caused by the square waves was 30% of the output peak, therefore 3 times larger than those caused by sine waves. These authors concluded that square waves were the least favorable option in terms of picking first arrivals and reducing near-field effects.

Therefore, from the literature it was evident that sine waves were more suitable source signals than square waves. Arroyo et al. (2003) and Jovičić et al. (1996) also considered distorted sine waves, which reduced the near-field effects even more than regular sine waves, but distorted sine waves were not considered for our research for practical reasons.

3.2 Signal Interpretation: Potential Sources of Error

Bender element testing involves numerous potential sources of error and biases. Identifying them in advance helps to reduce their effects.

3.2.1 Near-field Effects

Picking first arrivals of S-waves can be confounded by the effects of the near-field, which affect only V_S and not V_P (Brignoli et al., 1996). In a complex test system where received signals are not limited to plane wave propagation between source and receiver, near-field effects, which are the mixed radiations of P-waves and S-waves (Wang et al., 2007; Arroyo et al., 2003), occur. As the name implies, this confounding effect dies out as distance from the source increases because of the difference between P- and S-wave velocities. As stated earlier, S-waves are generated in the form of a frontal lobe and the P-waves as side lobes with respect to the bender element (Lee and Santamarina, 2005). As the direct-transmission S-waves arrive at the receiver bender element, so do P-waves reflected off the testing system walls. Wang et al. (2007) avoided the effects of P-wave interference on picking S-wave arrivals by placing the receiver at least two wavelengths away from the source. (This criterion was presented in section 2.4.)

A similar criterion was also found by Jovičić et al. (1996) when testing with sine waves. The authors found that the ratio of travel distance (L) and S-wavelength (λ) of the source signal can be optimized to limit near-field effects. For low values of L:λ, the near-field effects were present at the receiver and as the L:λ ratio increased, the effects of the near-field on the ability to pick shear arrivals decreased. This meant that the travel

distance of the shear wave, or the tip-to-tip distance between the source and receiver (L) had to be increased in order to significantly decrease the near-field effects for a given (λ).

For this study, as mentioned in section 2.4, the volume of the test system and the wave travel path had to be minimal. These conflicting requirements resulted in a mid-range selection of D:L (Table 2.1). Detecting the actual shear wave arrival is less a priority for this study than establishing a repeatable response ("signature").

3.2.2 Electrical Crosstalk

Electrical crosstalk can also be a major source of error. The wiring of the bender elements can influence how much electrical crosstalk is present. Parallel - aligned bender elements have a shielding effect when the outer electrodes are connected to the ground and so crosstalk can be significantly reduced (Lee and Santamarina, 2005). In our testing, the bender elements were aligned parallel to one another and a grounding setup presented by Wang et al. (2007) was implemented but crosstalk was still excessive; therefore further steps had to be taken to reduce it. A voltage divider was applied to the signal passing from the linear amplifier to the signal analyzer (Fig. 2.6.), and the source and receiver inputs on the analyzer were spaced as far apart as possible. With these two additional steps, the electrical crosstalk in the received signals was significantly reduced.

3.2.3 Boundary Conditions

Rigid boundary conditions also cause wave distortions due to the interference of the direct waves with reflected waves (e.g. Arulnathan et al., 1998). For example, for the

direct-transmission ray path, after the incoming energy first actuates the receiver bender element, the energy reflects off the plate on which the receiver bender element is mounted and is seen again as another arrival as it passes the receiver bender element in the opposite direction. In our experiment, the most significant reflecting surface for direct-transmission energy would be the top cap in which the receiver was mounted.

3.2.4 Mechanical Impedance Traps

Source bender elements generate a signal at the anchor in addition to what is generated along the length (Lee and Santamarina, 2005). In the absence of isolation or mechanical impedance traps, this signal could reach the receiver element by travelling along the cell walls and therefore introduce error in the received signal by short circuiting the test specimen altogether. The bender elements used in this research were prepared to minimize this error. As mentioned earlier, potting the bender elements using epoxy within a vinyl casing, and then fixing them onto the top cap and base plate with RTV silicone creates impedance traps which limit the transfer of mechanical wave energy (Lee and Santamarina, 2005).

3.2.5 Coupling Effects

Coupling between transducer and test medium is critical in bender element testing. Void formation around the source bender element is another potential source of error (Lee and Santamarina, 2005; Wang et al., 2007). Therefore care should be taken with installing the bender elements, and to densify and compact the specimen properly in order to minimize the production of voids between the element and the test specimen.

3.3 Testing System Delay

When making measurements with a complex testing system, any time offset in signal transmission caused by the testing system must be accounted for. This section describes system offsets and system delays caused by the testing system.

Here, we define system offset as the time difference between the time of actuation of the source signal (by the function generator) and the recorded time for the source sensor (on the signal analyzer). If the same system offset is present in the source signal and the received signal, the offsets cancel out. We define a system delay to result when the system offset of the source signal and the system offset of the received signal are unequal and so do not cancel.

To check for system offset and delay, the source and receiver bender elements were made to touch at the tips (Fig. 3.1); a bender element from the same production batch was substituted for the bender element from the base plate of the testing system for maneuverability purposes. By making the bender elements touch, the travel distance between them was zero so that the travel time for the signal to be received was also theoretically zero. With this configuration, in the absence of system delay, the actuation time of the source signal should be the same as the first arrival time of the received signal.

The time interval between pulses initially used for data collection was 10 ms. The source bender element was actuated with single sine pulses at 8 kHz and 5 V, with 10 ms intervals between pulses. This initial choice of time interval between pulses was increased in future tests (Sec. 7.4). The sine pulses were generated by using a burst

function, which allows the function generator to create individual sinusoidal pulses at predetermined intervals. The signals were amplified to 10 V. The amplification was applied to replicate planned testing in saturated glass beads, where the signal would be amplified to improve signal to noise ratio. Trials were carried out with no filtering, with a high-pass filter at 1 kHz and with a band-pass filter at 1 and 16 kHz. The high-pass filter presents a situation where the received signal is processed through the filter equipment once. The band-pass filter presents a situation where the received signal is processed through the filter twice.

The results without filtering are presented in Fig. 3.2; three repetitions are shown with each repetition consisting of the average of 1000 pulses. Averaging or stacking pulses to improve quality of received bender element signals was demonstrated by Wang et al. (2007). The number of averages used in this research was determined experimentally. The source signal was actuated at time 10 ms and the source initiation recorded on the signal analyzer was at time 9.98 ms, giving a negative offset of 20 μs. The received signal pick occurs one sample later than the source initiation time. The sampling interval was 10 μs; which was near the shortest possible sampling rate of 9.4 μs with the signal analyzer used. Therefore a 10 μs system delay is present, with the received signal trailing the source signal.

To test the cause of the negative system offset, a BNC cable was connected directly from the function generator to the signal analyzer, bypassing the linear amplifier and voltage divider (Fig. 2.6), and the same single sine pulse was applied at 10 ms intervals, with identical results. This test demonstrated that the system offset is not caused by the linear amplifier or voltage divider.

Results of the system offset/delay test using a high-pass filter at 1 kHz are presented in Fig. 3.3. Variations in amplitude and phase were present in the shape of the received signal with respect to the received signal without filtering (compare Fig. 3.2a to 3.3a), but they were well after the first arrivals. The same time offset and delay as without filtering were encountered.

The results of using the band-pass filter are presented in Fig. 3.4; these signals show the same system offset but a longer system delay. The source signal was received at 9.98 ms as before, and the received signal was at 10 ms, yielding a system delay of 20 μs (two samples), with the received signal trailing the source signal.

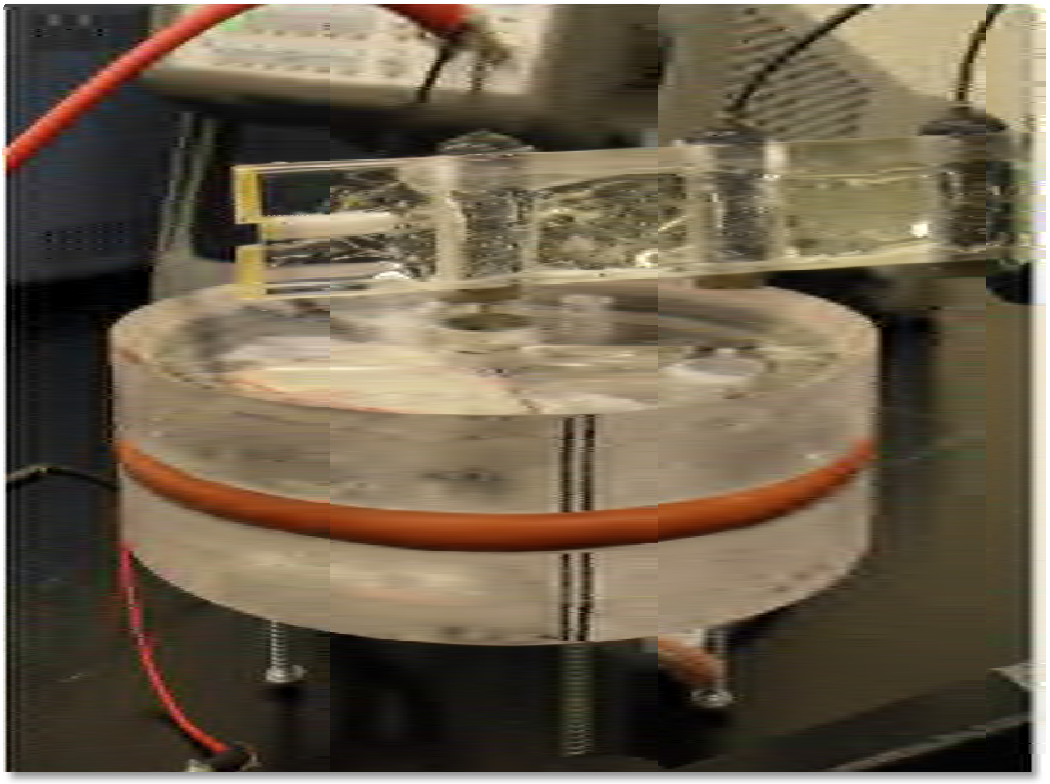

Figure 3.1. System delay test: source (top) and receiver (bottom, in top cap) bender elements touching to make the travel distance zero

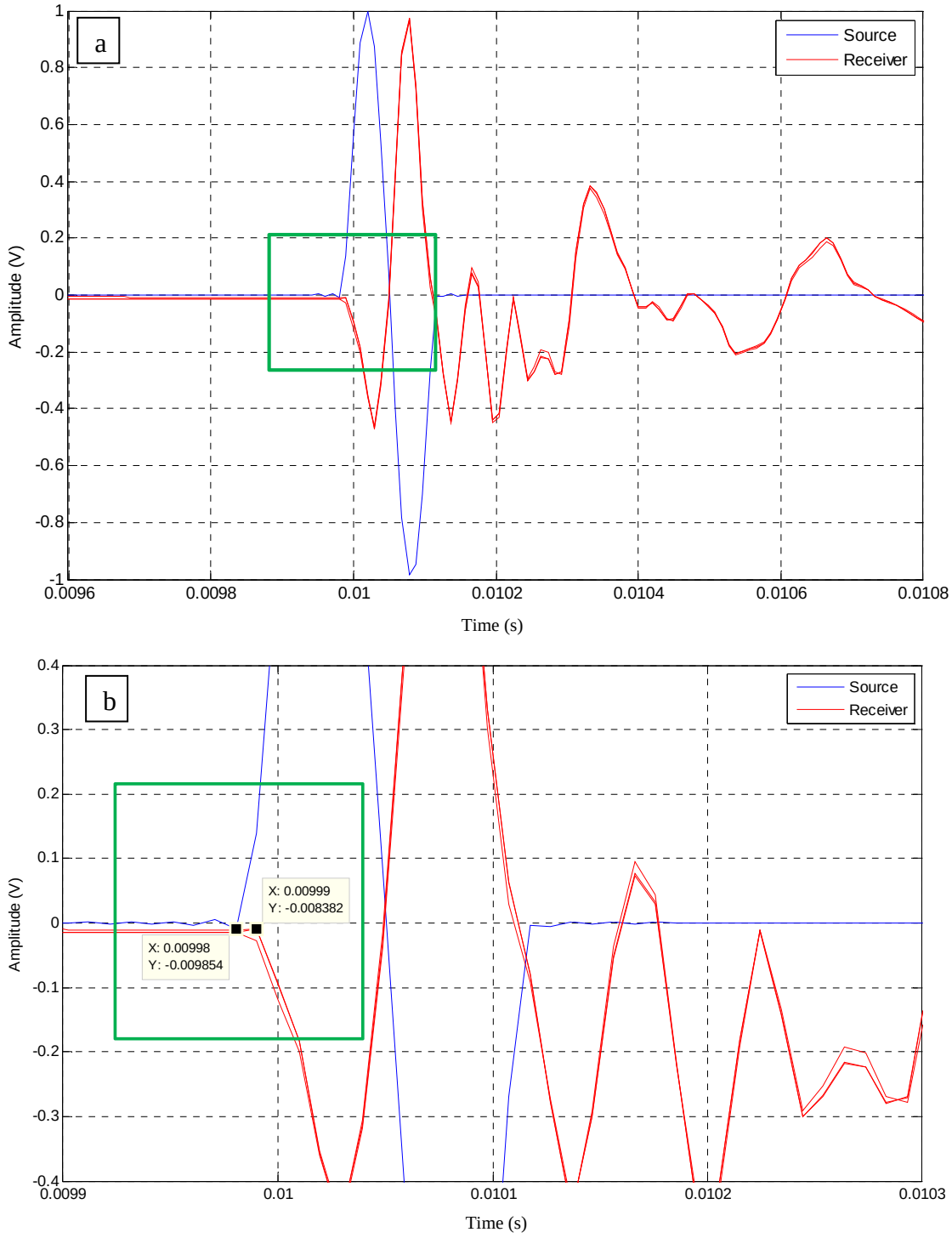

Figure 3.2. System delay test, no filter: pulse signal at 8 kHz, applied at time 10 ms. Three repetitions superimposed, 1000 recordings averaged per repetition.

a: Extended view, green box shows zoom window
b: Detail view demonstrating system offset of -20 µs with 10 µs system delay

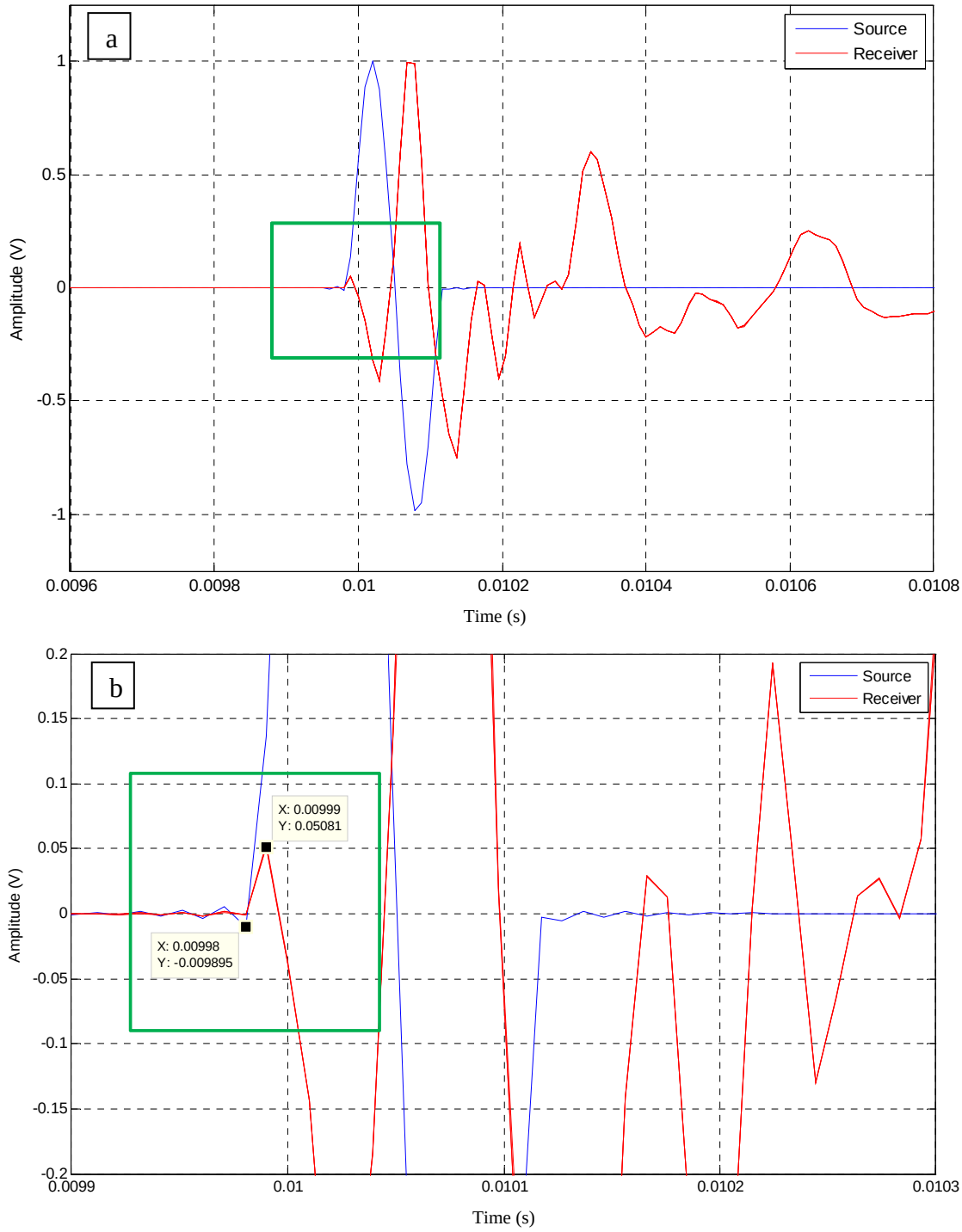

Figure 3.3. System delay test, high pass filter at 1 kHz: pulse signal at 8 kHz, applied at time 10 ms. Three repetitions superimposed, 1000 recordings averaged per repetition.

a: Extended view, green box shows zoom window
b: Detail view demonstrating system offset of -20 µs with 10 µs system delay

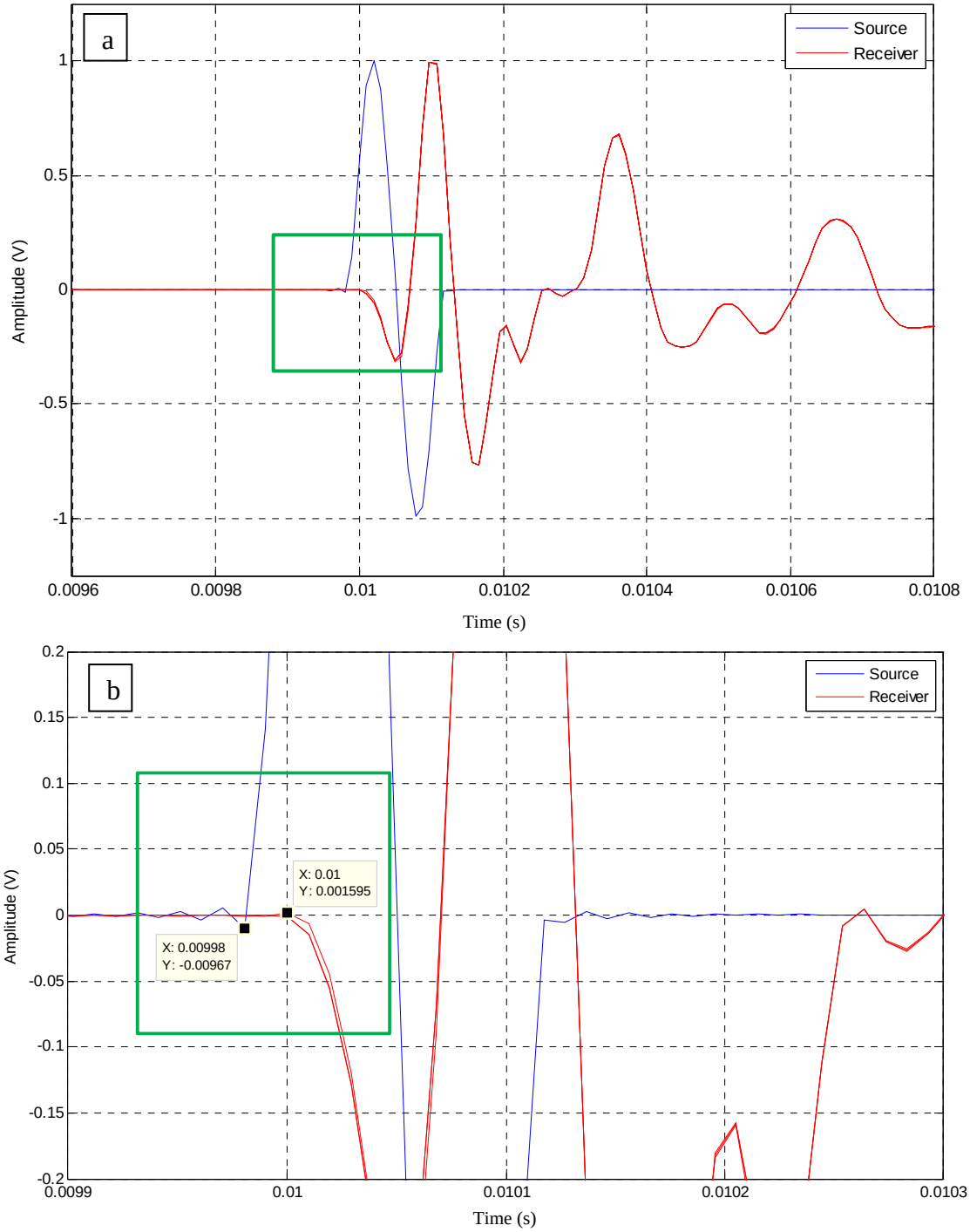

Figure 3.4. System delay test, band pass filter at 1 kHz and 16 kHz: pulse signal at 8 kHz, applied at time 10 ms. Three repetitions superimposed, 1000 recordings averaged per repetition.

a: Extended view, green box shows zoom window

b: Detail view demonstrating system offset of -20 µs with 20 µs system delay.

CHAPTER 4

TESTING METHODS: LITERATURE REVIEW

There are many methods available for testing with bender elements and researchers are not in complete agreement about which method is best. No standard exists for the testing procedures or for the interpretation of the results (Da Fonseca et al., 2008).

One appeal of bender elements for measuring mechanical properties of specimens is that the concept is simple; seismic energy is actuated and received by bender elements and the received signal is analyzed to identify the seismic signature of the system. Many researchers use bender element testing to find the shear wave velocity of the specimens being tested, from which other mechanical properties can be derived. It is important to point out that we are not primarily concerned with the received signal velocity, rather we seek a means to monitor for change in the response of the system in the presence of an experimental treatment. This change could be related to the frequency content and shape of the signals, in addition to velocity and amplitude as was seen in testing carried out by Williams et al. (2005).

This chapter presents the testing methods used by previous researchers in bender element studies to determine shear and compression wave velocities from which other mechanical specimen properties could be derived. The test methods are divided into time domain methods and frequency domain methods. No prior research on the analysis of frequency content and signal amplitude from bender element testing was found, although this topic was addressed in this study.

4.1 Time Domain Methods

This section analyzes time domain methods that have been used with bender element tests in the lab to determine velocities. Three methods were considered: first arrival; characteristic points; and cross correlation.

4.1.1 First Arrival

The first arrival method has been used successfully to determine the travel time with bender element testing by numerous researchers (Leong et al., 2005). For example, Lee et al. (2007) used the first arrival method in a modified oedometer cell to calculate the shear wave velocity from recorded data to estimate consolidation characteristics of a marine clay specimen. The first arrival method utilizes the length of the travel path between the source and receiver bender element and the travel time derived from the transmitted and received signals to calculate the velocity of the received energy. Picking the first arrival has been documented as a difficult task due to uncertainty associated with correctly picking the first deflection point (Arulnathan et al., 1998). The uncertainty results from signal attenuation, noise such as electrical crosstalk and, in some cases, near-field effects (Sec. 3.2).

4.1.2 Characteristic Points

The characteristic points method is like the first arrival method, except travel time is calculated from more easily identified points on the wave train than the point of first

arrival. This is done to avoid the uncertainty issues described above. The drawback with this method is that wave velocities are underestimated due to signal attenuation.

Clayton et al. (2004) used the characteristic points method in research concentrated towards improving the objectivity and repeatability of shear wave velocity measurements by bender elements. Experiments were carried out on Leighton Buzzard sand in a triaxial testing apparatus. The source was mounted at the base and receivers were mounted along the side wall and in the top cap. Discrete sine pulses were actuated at frequencies from 6 kHz to 30 kHz. The characteristic points considered were the first trough and subsequent peak associated with the first deflection. Travel times were determined from differences between timings for characteristic points of the received signals at successive receivers. The results showed better repeatability at higher frequencies (10 to 30 kHz) when compared with lower frequencies (6 to 10 kHz).

4.1.3 Cross Correlation

Cross correlation indicates similarities between the source and receiver waveforms. For well-correlated data, the time associated with the peak of the cross correlation relates directly to the transmission time of the wave, which is simply the difference in time from initiation to the peak of the computed function (Reynolds, 2000).

Viggiani and Atkinson (1995) used cross correlation to determine shear wave velocity of a reconstituted clay specimen in a triaxial testing apparatus from bender element testing. Source and receiver bender elements were placed in the end caps of the triaxial apparatus. The authors concluded that their results from the cross-correlation method were very accurate; however, the results could vary depending on the testing apparatus.

Lee and Santamarina (2005) found that the results can also vary when signals being correlated are not of the same nature. Distortions in the received signal with respect to the source signal complicate the correlation function and confound the determination of transmission time.

4.2 Frequency Domain

The frequency domain methods considered include discrete methods and the frequency sweep method.

4.2.1 Discrete Methods

Considering the use of bender element testing in the time domain, Greening and Nash (2004) found that problems caused by transient effects such as reflected waves are removed if impulsive signals are replaced with a continuous harmonic signal. Discrete methods use continuous sinusoids at select frequencies. According to Greening and Nash (2004) and Da Fonseca et al. (2008), discrete methods are time consuming but provide a way to determine the travel time of the system in the frequency domain without involving measurements of travel distance. Two types of discrete methods were considered; the continuous harmonic signal method and the π-point identification method.

4.2.1.1 Continuous Harmonic Signal Method

Like pulse signals, continuous signals can also be used to derive travel time between source and receiver (Rio, 2006), and hence, velocity. This is a manual process, meaning that to get results at different frequencies the signal has to be stepped manually. For each frequency, a continuous harmonic signal is actuated and data are collected via the signal analyzer. The travel distance remains fixed. At each frequency step, the phase difference between consecutive peaks and troughs of the source and receiver is calculated (Rio, 2006). The phase differences are then plotted against their respective frequencies. The slope of the plot is used to calculate the travel time.

4.2.1.2 π-Point Method

The π-point method is the reverse of the continuous harmonic signal method (Greening and Nash, 2004). Here the frequency of the sinusoid is varied until the received signals meet preselected phase differences (i.e. π and –π radians; Rio, 2006). As shown by Da Fonseca et al. (2008), in an ideal material (homogenous, isotropic) this process produces a linear relationship between phase angle and frequency, from which the slope is determined to calculate the travel time.

4.2.2 Frequency Sweep Method

The frequency sweep initially sweeps over a broad range in which the coherence between the source and receiver signal is used to determine an intermediate range over

which output signals produce optimal transfer of input energy. The signal analyzer correlates the source signal and received signal, and produces a coherence plot that ranges from 0 to 1 over the span of the frequency sweep. If the coherence is close to 1, more energy in the output signal is caused by the input signal and the two are well correlated (Da Fonseca et al., 2008). High coherence between the signals is necessary to obtain low variation in the results (Da Fonseca et al., 2008). Once the intermediate range is identified, the frequency sweep is concentrated on that range, from which plots of unwrapped phase angle with respect to frequency are used to determine the travel time. The frequency sweep method has the same outcome as the discrete methods, it is more efficient, and it also allows the calculation of the coherence function, which improves its reliability over the discrete method (Rio, 2006).

4.3 Test Methods: Summary

The first arrival, characteristic point, and cross correlation methods in the time domain are chosen for analysis, because of the applicability to this study and documented success. It was decided not to use either of the discrete methods because they were time consuming and required heavy signal processing. The frequency sweep method can be carried out quickly and with less signal processing effort (Greening and Nash, 2004).

CHAPTER 5

CALIBRATION IN AIR AND WATER

The system was first calibrated in air and water. This chapter presents the testing system set up, the testing methodology, data processing and the results.

5.1 Testing System Setup

As presented in section 2.4, three parameters were considered for test column design: D:L ratio; L:λ ratio; and minimizing L to minimize volume and signal attenuation. The L value chosen depends on the reference shear wave velocities, the D value was fixed and the λ depends on the actuation frequency, which was selected experimentally for the tests in air and water. The test system was optimized for shear wave transmission as opposed to compression wave transmission. This is because a test system optimized for S-wave transmission can still receive useful P-waves, which is not the case if the test system is optimized for P-waves. P-waves are better received with the bender elements close to each other, which would lead to significant near-field effects on the S-waves, and render them useless.

The bender element in the base plate was always used as the source, and the bender element in the top cap was always used as the receiver.

Lee and Santamarina (2005) reported that when bender elements with short cantilever lengths are used, the resonance frequency in air is higher than the resonance frequency in saturated granular media. In the current experiment, the resonance frequency was

identified by a sudden increase in sound from the actuating bender element during a frequency sweep and by observing the amplitude spectrum of the received signal. In air, the source bender element started to resonate at around 6 kHz and plateau around 8 kHz, reaching the peak displacement amplitude around 12 kHz (Fig. 5.1). In water, the resonance frequency of the source bender element peaked at approximately 8 kHz (Fig. 5.2). For this study in which the primary goal is to address testing with glass beads under essentially saturated conditions and ambient pressure, the frequency for testing was chosen to be 8 kHz. This frequency was used to calculate the value of L for the placement of the top cap, a value which was maintained for all testing in this study.

As discussed in Sec. 3.2.1, the ratio L:λ is selected to minimize near-field effects. To do so, a reference shear wave velocity was required. Patel et al. (2009) reported shear wave velocity (V_S) for water-saturated glass beads under ideal stacking conditions, achieved by placing the specimen on a vibration table, and at ambient pressure to be 150 m/s. Using this reference V_S, the actuation frequency (F_r) of 8 kHz and the following formula:

$$\boldsymbol{\lambda = {}^{V_S}/_{F_r}},$$

the reference λ was found to be 18.8 mm. This number presents the following possible values for L:

1. $L > 2\lambda \rightarrow L > 37.6$ mm
2. $4.2 > D{:}L > 2.2 \rightarrow 69.3 \text{ mm} > L > 36.3$ mm

These values address the criteria put forth in section 2.4. The value of L selected for this research represented a compromise between the conflicting design criteria discussed in sections 2.4 and 3.2.1. The distance from the top of the base plate to the bottom of the

top cap (H) was selected to be 70 mm, which yields a value for (L) of 62 mm, given 4 mm protrusion of each bender element. This (L) value gives a D:L ratio of 2.4. Note that measurements of (H) for top cap placement were made from outside the column using a digital caliper which is accurate to 0.1 mm, but the readings were rounded off to the nearest integer millimeter.

Three acrylic spacers were used to hold up the top cap at the required height for the air and water tests (Fig. 5.3). With the spacers in place, the average of five measurements of (H) was 71 mm, which differs from the target value by 1.5%.

5.2 Testing Methodology

The first-arrival and cross-correlation methods were used for calibrating the system. As described previously, individual sine pulses at 8 kHz at 10 ms intervals were used for actuating the source bender element. Each test was repeated three times, where the average of 1000 pulses was considered as one repetition.

The travel path lengths were determined as shown in Fig. 5.4. From them, the theoretical travel times were calculated by using expected values for P-wave velocity in air and water. As mentioned earlier, P-waves were assumed to be generated in the form of side lobes, therefore the reflected travel path was assumed (Lee and Santamarina, 2005).

Sengpiel (2010) reports compression wave speed in air at 70˚F to be 343 m/s. Santamarina et al. (2001) report compression wave speed in water at 70˚F to be 1480 m/s.

By using these data and assumptions the anticipated travel times were calculated. Except where noted, testing was done without filtering.

5.3 Results for Testing in Air

The time history and Fourier amplitude spectrum (to 500 Hz) of the received signal in air are presented in Fig. 5.5. The pulse signals are riding upon a low frequency background signal. The Fourier amplitude spectrum shows that the dominant frequency is 32 Hz with resonances at 58 Hz, 82 Hz, and 105 Hz. A high-pass filter with a cut off frequency of 1 kHz was applied to remove the disturbance; a lower cut off frequency might have been adequate but was not tested. The filtered time history is presented in Fig. 5.6; the low frequency background signal is removed. Figure 5.6 shows two consecutive pulses, which demonstrate that the energy from one pulse does not completely decay prior to the arrival of the next pulse. This affects the ability to make an accurate first arrival pick because it increases the background noise threshold. It is recommended that the interval between pulses be increased for any future testing in air to reduce these effects on the arrivals. Figure 5.7 is an amplification of data shown in Figure 5.6, which shows a first arrival and the source pulse, offset to facilitate comparison. The first data point on the received waveform demonstrating amplitude clearly greater than the background noise threshold occurs at approximately 0.51 ms. Two excursions of the waveform exceeded the background noise threshold prior to this time, but they were considered too close to the threshold to be counted as a first arrival. The first arrival time picked is 4% later than the anticipated arrival time (Table 5.1), assuming a reflected

travel path (Fig. 5.4) as expected for side-lobe energy actuation of P-waves from the faces of the bender elements as demonstrated by Lee and Santamarina (2005). Note that both the residual noise from the previous pulse which partially obscures the actual arrival and also the algorithm for picking arrivals cause the process to err on the slow side, leading to the chosen arrival time being later than the actual arrival. Note that a change in frequency and shape of the received signal within the background noise prior to the arrival pick might be interpreted as faint evidence of the direct-transmission arrival.

The source signal and the received signal were cross-correlated using the signal analyzer. The results for testing in air are presented in Fig. 5.8. When no filtering was used, the cross-correlation result had a dominant "V" shape. A 1 kHz high-pass filter was applied, and the "V" was removed. The filtered and the non-filtered results gave the same peak time, which was 30% slower than the anticipated reflected wave travel time (Table 5.1). This peak time is of course slower still than the anticipated direct wave travel time. Lee and Santamarina (2005) assert that the cross-correlation technique must either relate signals of the same nature or accommodate for the testing system's transfer functions. The received signal was a heavily modified version of the source sine pulse (e.g., Fig. 5.5). Unless the transfer function can be accounted for, or the received signal is filtered to mask effects of multiple reflections and other scattering that dominate the wave train at later times, the results of this cross-correlation analysis are not meaningful.

The tests in air determined the arrival time for compression wave velocity within approximately 4% of the anticipated time using the first arrival method with a 1 kHz high-pass filter and assuming a reflected travel path. The accuracy of results can be improved by reducing background noise.

5.4 Results for Testing in Water

Testing was repeated in room-temperature distilled water. The results for the first arrival method are presented in Fig. 5.9. Unlike for testing in air, there was no low-frequency carrier energy present. However, a first arrival pick could not be made because it appeared to coincide with electrical crosstalk. We know this was crosstalk because the initiation time was exactly the same and the duration is approximately the same as the source signal, 0.14 ms. This crosstalk effect was not observable in air because it was obscured by the background noise, which was significantly higher in air than in water (e.g., compare Figs. 5.6 and 5.9). The arrivals in air occur after the crosstalk effects die out.

To differentiate between the P-wave arrival and the electrical crosstalk, a set of trials was carried out where the travel distance through the water was varied, while all other features of the testing were kept constant. This process allowed differentiating between where the electrical crosstalk ends and the received signals begin. As the travel distance increases the arrival time for the P-waves should increase while the electrical crosstalk would remain constant. Four trials were carried out, where the first was at the initial spacing used (L = 62.5 mm), and the spacing of each successive trial was increased by 12.7 mm.

The results are presented in Fig. 5.10 and Table 5.2. The majority of the arrivals occurred at different times, and in the correct order with the shortest travel path arriving first. The first three spacings' arrivals were successively one time sample apart, and the third and fourth arrivals had the same arrival time. Due to the cross talk it was not

possible to pick the P-wave arrival with certainty. The anticipated direct and reflected wave arrival times for all the spacings used were within the duration of the crosstalk or just beyond it. The actual arrivals of both the direct and reflected P-waves could not be timed using the first arrival method because of the residual crosstalk and also because of the sampling rate. It should be noted that the received signal waveforms at all four spacings tested were similar in amplitude and frequency content between 0.3 and 0.5 ms, indicating a resonance condition in the test chamber that is independent of the parameter (H).

The results for cross correlation testing in water are presented in Fig. 5.11. Like in air, there was a low-frequency disturbance present, which was removed with a 1 kHz high-pass filter. As with tests in air, the cross-correlation results gave a peak time that was significantly later than the anticipated direct or reflected wave travel times (Table 5.3). Again, post processing of the received signal would be required in order for the cross-correlation computation to be meaningful.

Table 5.1. Anticipated and measured P-wave travel times in air

Wave travel path	Anticipated travel time (s)*	Method	Experimental travel time (s)	Difference
Direct	1.92E-04	First arrival	5.10E-04	62%
		Cross correlation	7.03E-04	73%
Reflected	4.91E-04	First arrival	5.10E-04	**4%**
		Cross correlation	7.03E-04	30%

*The anticipated travel time accounts for the 10 μs delay with the testing system.

Table 5.2. Test to differentiate electrical crosstalk from P-wave arrivals in water

Wave travel path	Path length (mm)	Anticipated travel time (s)*	Experimental travel time (s)	Difference
Direct	62.5	5.22E-05	8.79E-05	41%
	75.2	6.08E-05	9.77E-05	38%
	87.9	6.94E-05	1.07E-04	35%
	100.6	7.80E-05	1.07E-04	27%
Reflected	164.7	1.21E-04	8.79E-05	-38%
	169.9	1.25E-04	9.77E-05	-28%
	175.9	1.29E-04	1.07E-04	-20%
	182.6	1.33E-04	1.07E-04	-24%

*The anticipated travel time accounts for the 10 μs delay with the testing system.

Table 5.3. Cross correlation method: anticipated and measured P-wave arrivals in water

Travel path	Anticipated travel time (s)*	Experimental travel time (s)	Difference	Experimental Vp (m/s)
Direct	5.20E-05	4.20E-04	708%	392
Reflected	1.20E-04		250%	

*The anticipated travel time accounts for the 10 μs delay with the testing system.

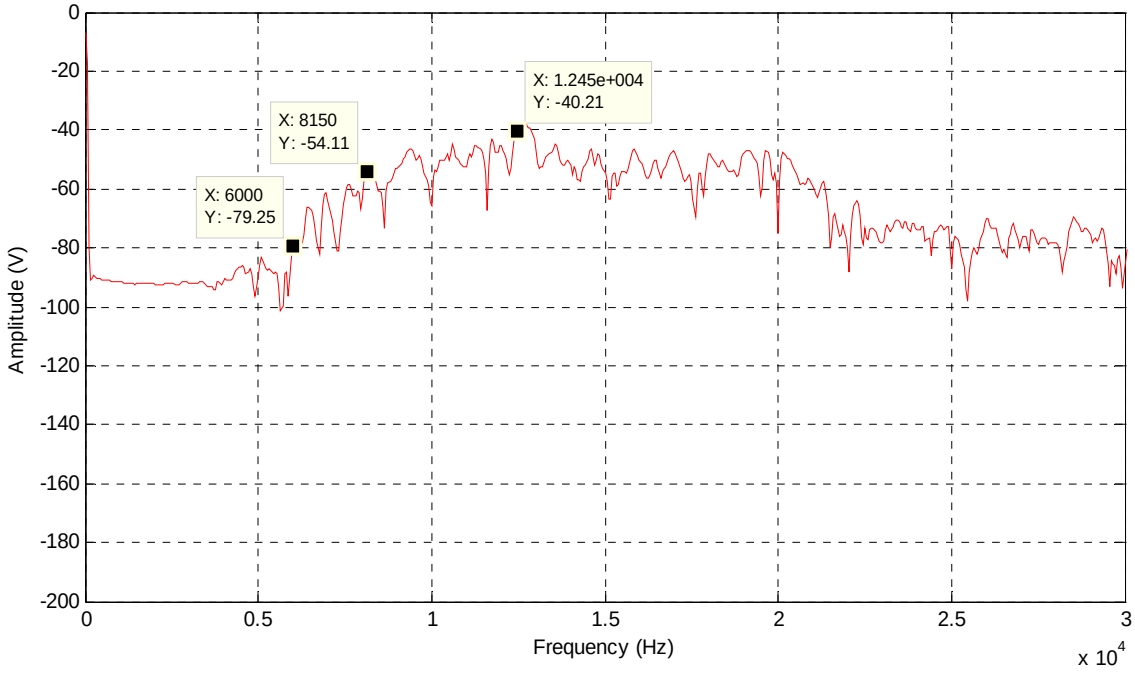

Figure 5.1. Frequency response for a 0-to-30 kHz sweep showing the resonance frequency of the test system in air; average of 1000 recordings

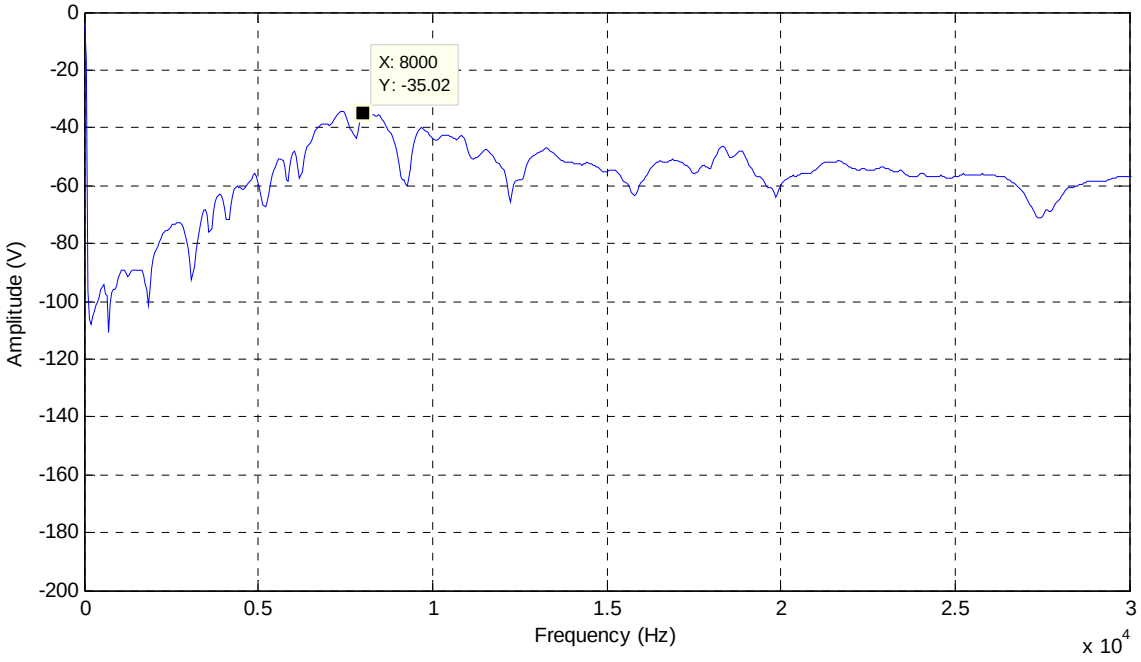

Figure 5.2. Frequency response for a 0-to-30 kHz sweep showing the resonance frequency of the test system in water; average of 1000 recordings

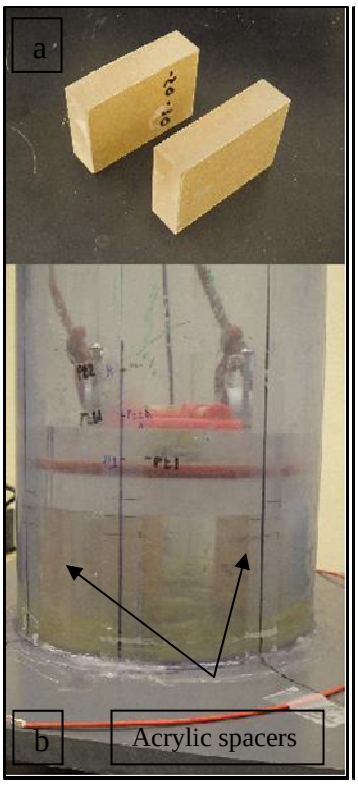

Figure 5.3. Acrylic spacers used for testing in air and water to hold top cap at the required height

a: Acrylic spacers;
b: Side view of column with spacers in place

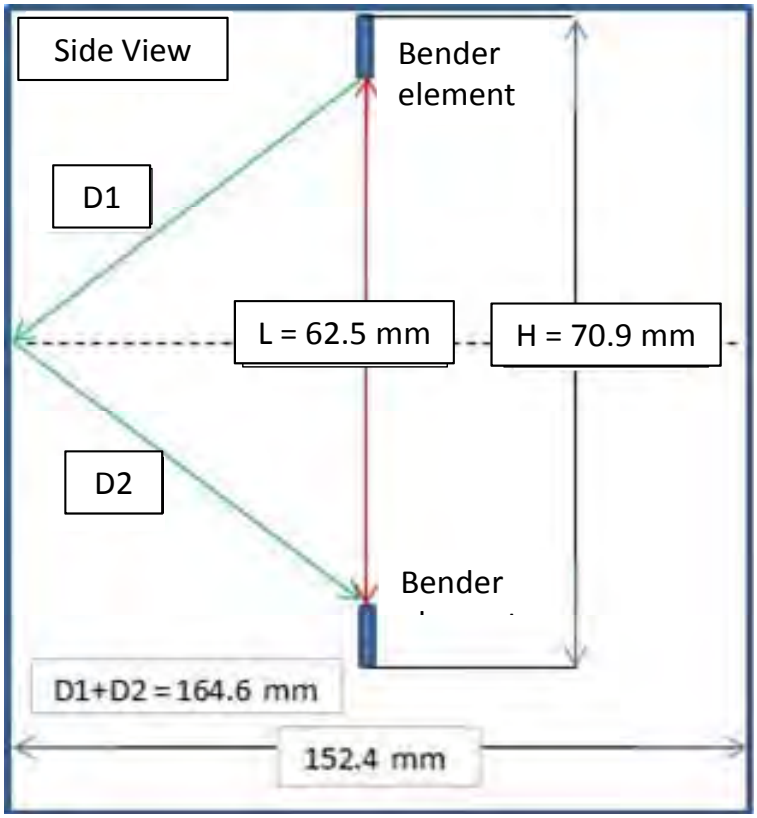

Figure 5.4. Direct (red) and reflected (green) travel paths

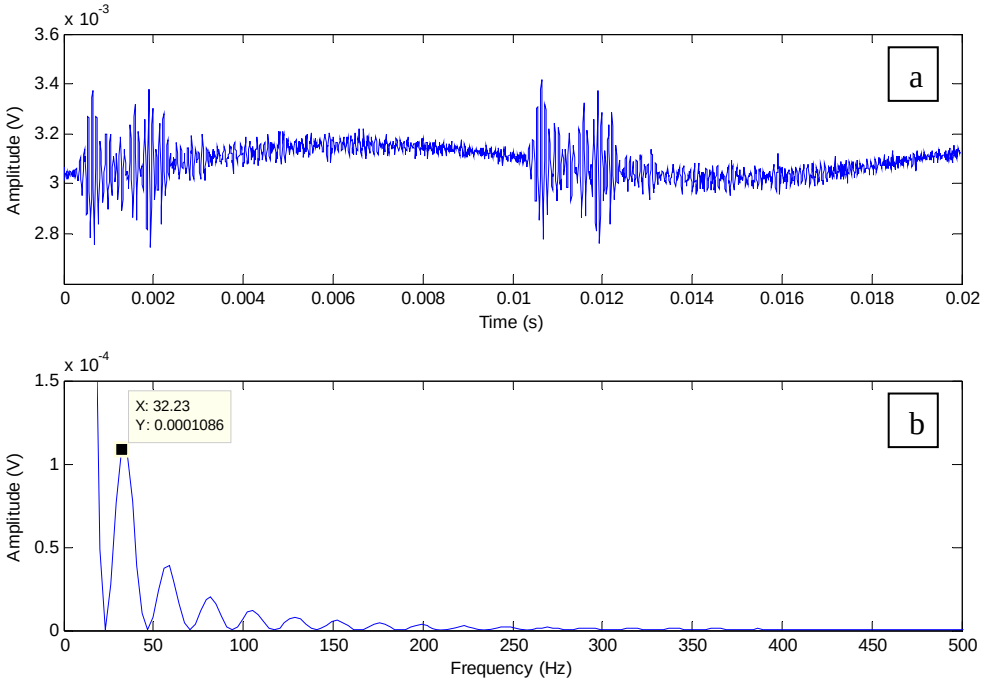

Figure 5.5. 8 kHz pulse signal in air with no filter applied, showing single repetition of 1000 recordings averaged per repetition.

a: Time domain result showing low frequency carrier harmonic
b: Frequency spectrum showing dominant carrier frequency at 32 Hz and its harmonics

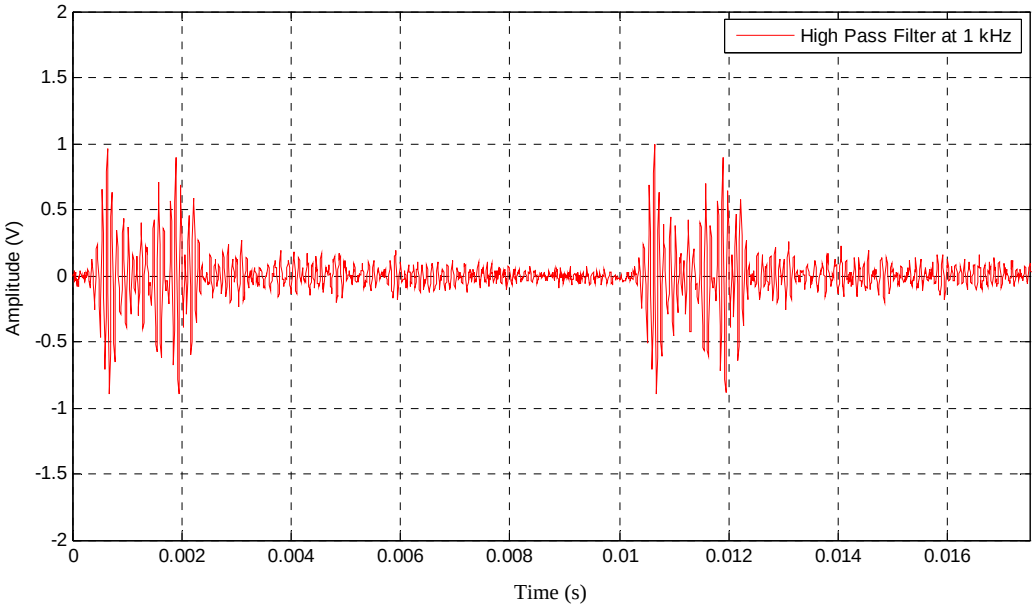

Figure 5.6. 8 kHz pulse signal in air with 1 kHz high-pass filter, showing single repetition of 1000 recordings averaged per repetition.

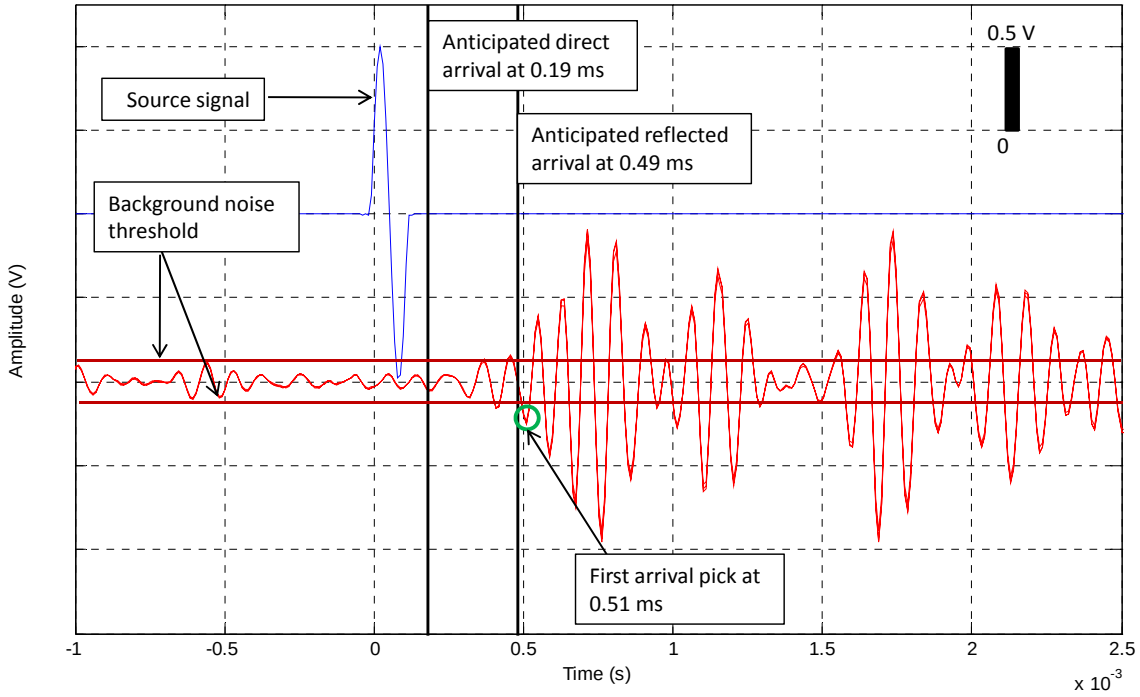

Figure 5.7. First arrival test in air with 1 kHz high pass filtering, shows three repetitions of an 8 kHz sine pulse with 1000 recordings averaged per repetition, arrival pick, source signal (offset for display purposes), anticipated arrival times, and background noise threshold.

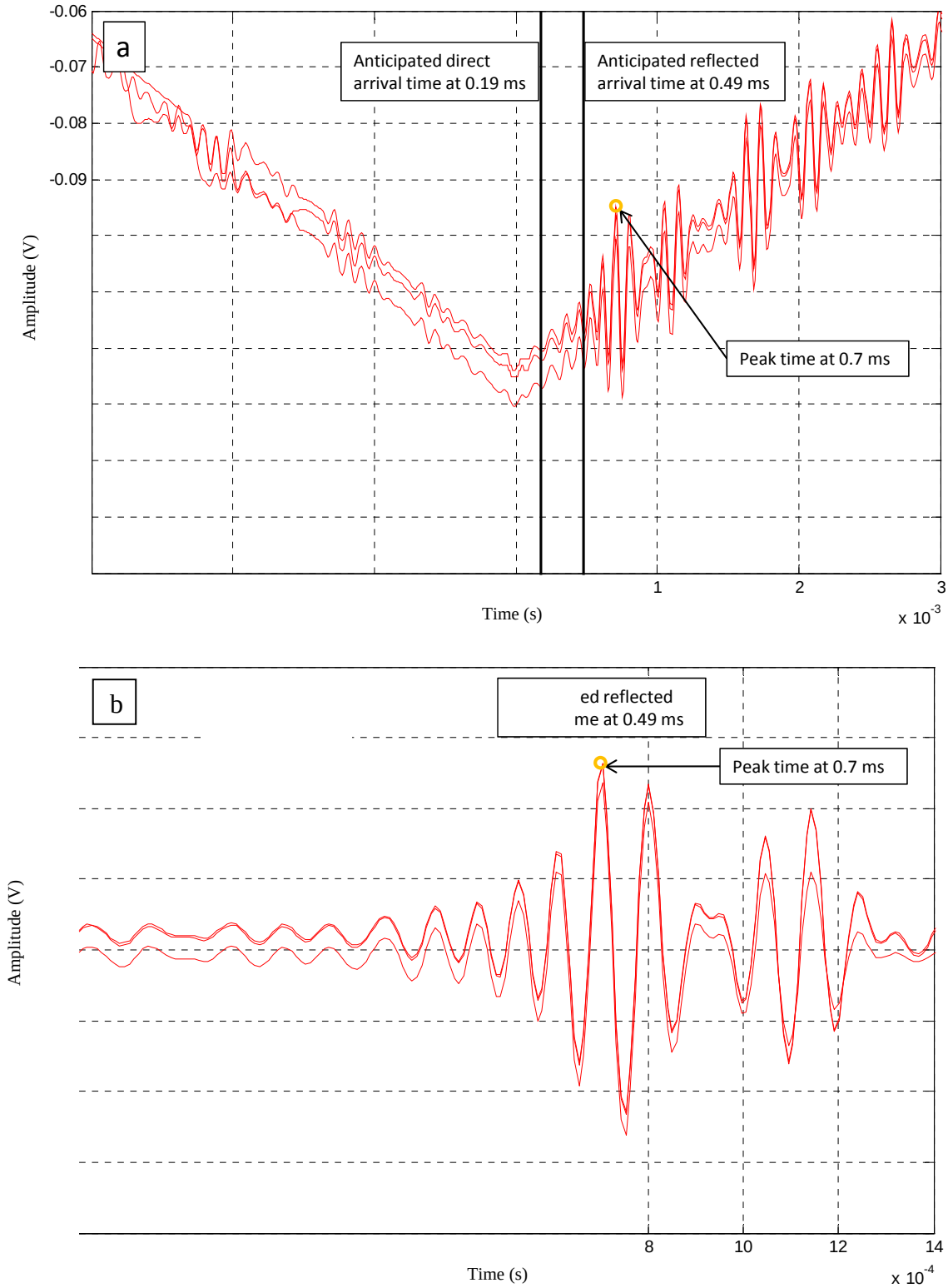

Figure 5.8. Cross correlation response in air showing peak times for three repetitions in air, 1000 recordings averaged per repetition.

a: No filtering applied
b: 1 kHz high-pass filter applied

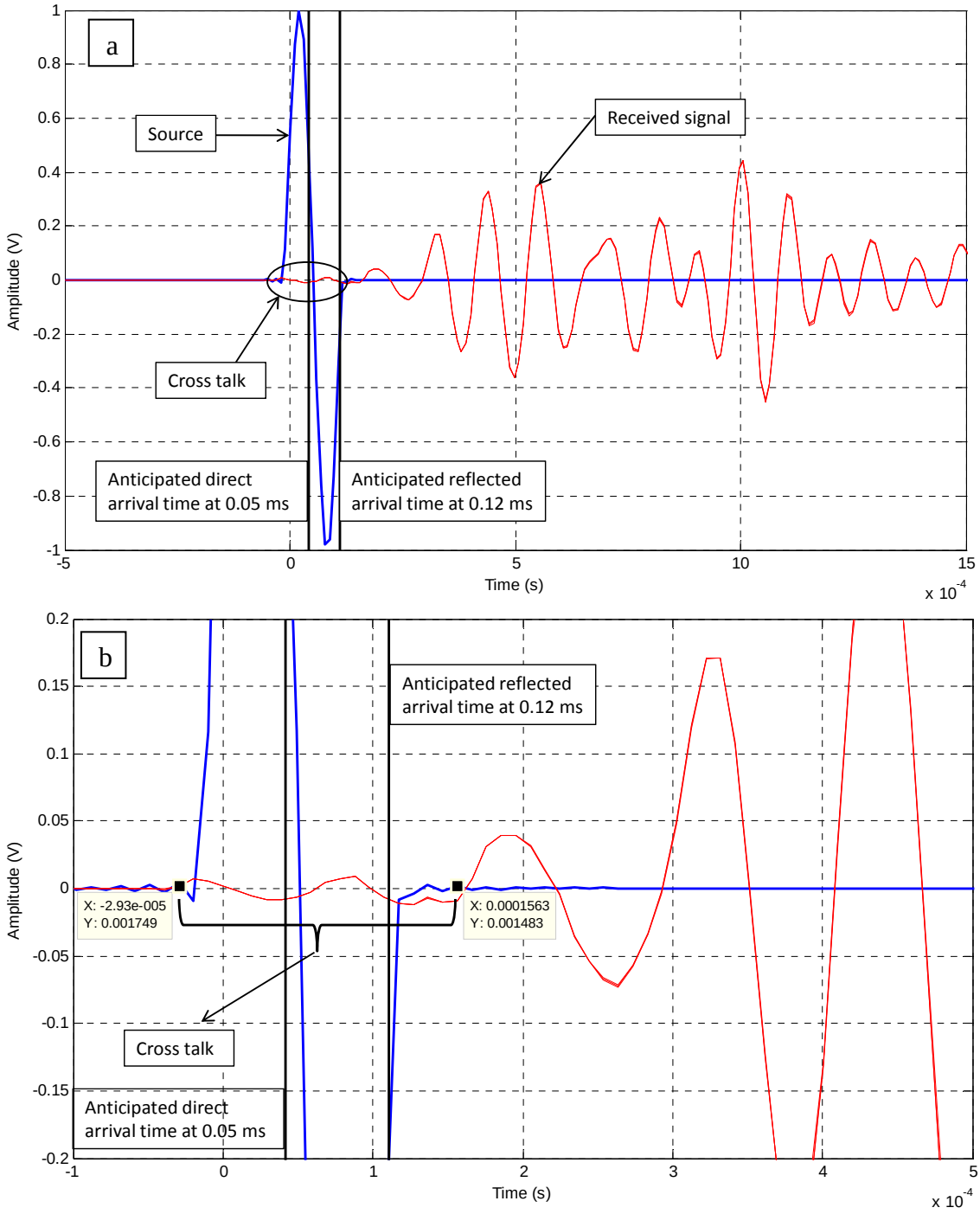

Figure 5.9. First arrival test in water with no filtering of an 8 kHz sine pulse, shows source (blue), receiver (red) with three repetitions of 1000 recordings averaged per repetition.
a: Expanded view
b: Detailed view

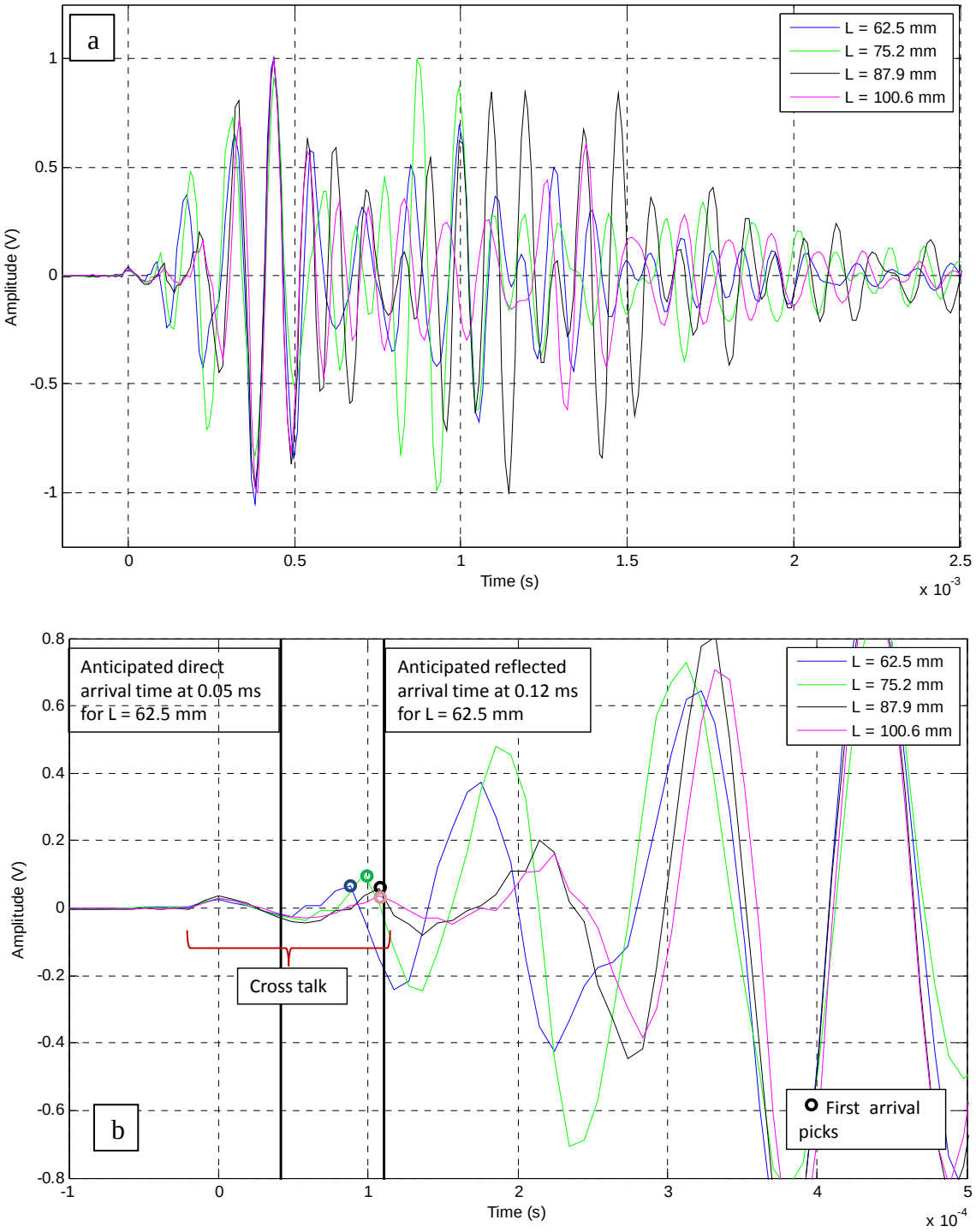

Figure 5.10. Differentiating electrical crosstalk from P-wave arrivals in water by varying the tip-to-tip distance, 1000 recordings averaged per received signal

a: Expanded view of entire received signal
b: Detail view showing crosstalk, anticipated arrival times for base case (L = 62.5 mm) and possible arrival picks

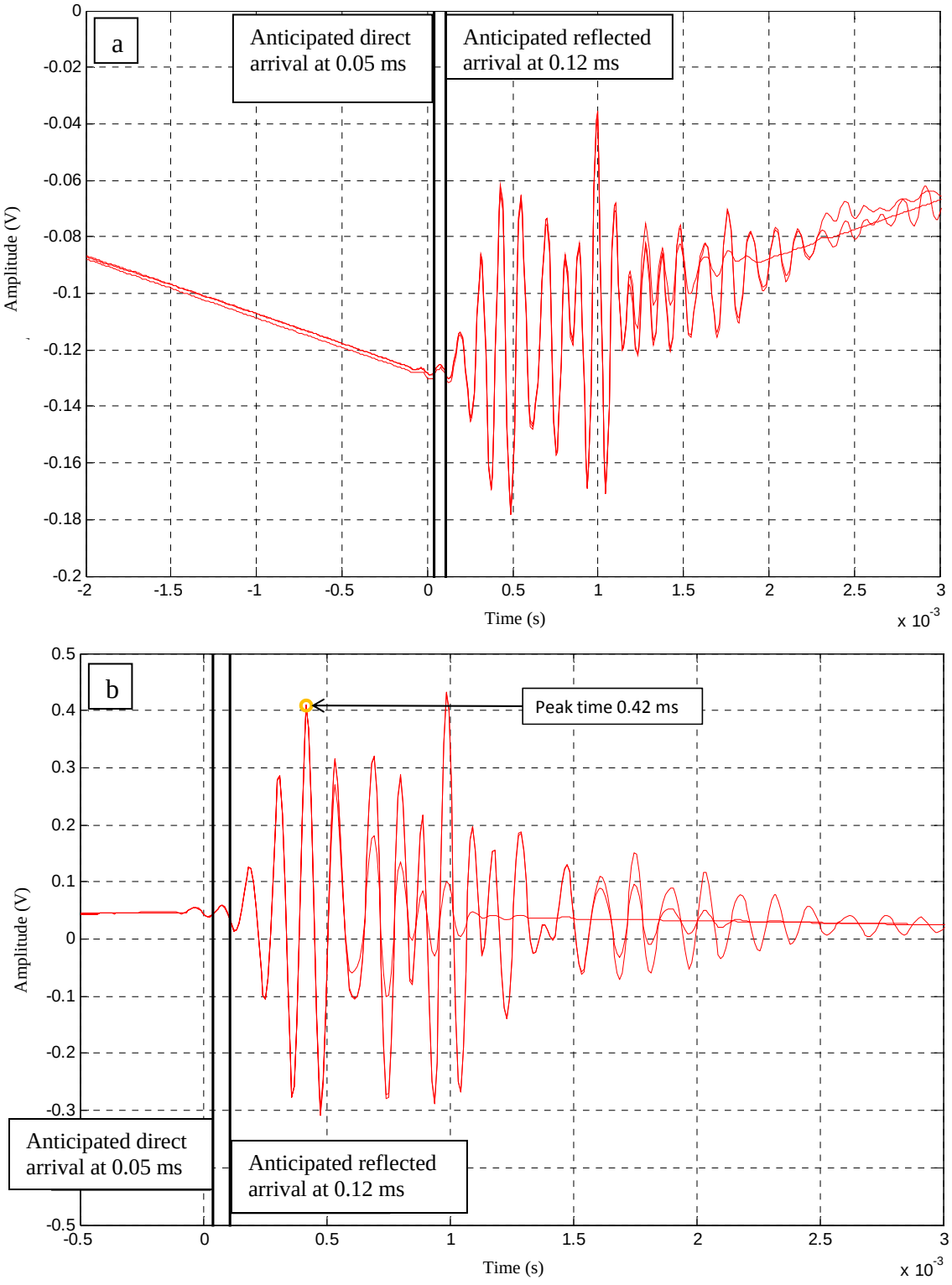

Figure 5.11. Cross correlation response in water showing peak times of three repetitions of 1000 recordings averaged per repetition.
a: No filtering applied
b: 1 kHz high-pass filter applied

CHAPTER 6

GLASS BEAD SPECIMEN PREPARATION

Prior to calibrating the testing system with water-saturated glass beads, a consistent method for preparing the glass bead specimens had to be established. Glass beads were used in testing because glass is inert and therefore minimizes variability caused by chemical interaction with the nanoparticles and the granular matrix. This chapter presents two methods tested for achieving repeatable specimens. Repeatability was judged by comparing the saturated unit weight of specimens prepared using the same techniques.

6.1 Methods of Specimen Preparation

The two methods used to prepare the specimens are called the dumping method and the stage fill method.

The glass beads used were 0.5 mm in diameter and purchased from Quackenbush Co., Inc. Distilled water was used for backfilling the pore spaces. For both methods, the glass beads and water to backfill were dispensed into the testing system to the desired heights. Once the glass beads were dispensed into the column and the top cap was placed and leveled, six measurements of specimen height H (Fig. 5.4) made with a digital caliper were averaged to establish the height of the test specimen. The samples were not fully saturated because there was no back-pressure applied and the water used was not de-aired. The water was plumed into the sample from the bottom until it was approximately 25 mm above the upper surface of the top cap and this is accounted for when calculating

unit weight; recall that the top cap had a port in it to allow water to flow out of the test cell (Fig. 2.4).

The mass of the glass beads and water dispensed into the column were recorded for each specimen; the average mass of three specimens was used as the reference mass. The moisture content, void ratio and saturated unit weight of the specimens prepared were calculated using the reference masses, the manufacturer-provided specific gravity of the glass beads (G_s =2.5) and the standard unit weight of water (γ_w = 9.8 kN/m^3); see appendix 1, pages 131 and 132 for details. The saturated unit weights ranged from 18 to 19 kN/m^3.

The specimens were tapped with a rod and the column walls were tapped on the side during sample preparation to reduce voids. Testing took place at atmospheric pressure and room temperature. No other external stresses were applied to the system.

6.2 The Dumping Method

Dry glass beads were poured into the dry column until they were near the required height. A flat disc was used to level the top surface and check if the required height (70 mm; Sec. 5.1) was achieved. This process was repeated until the required height was reached and then water was introduced slowly from the bottom. Three specimens were prepared; see appendix page 132 for details. The average saturated unit weight achieved was 18.9 kN/m^3 with deviation from the average ranging from 0.1% to 0.5%.

6.3 The Stage Fill Method

The stage fill method was described by Rajabdeen et al. (2011). The first step was to introduce water into the column to a depth of approximately 35 mm, then pour the glass beads into the column in approximately 10 stages. After each stage, more water was plumed into the column so that the water level was kept above the surface of the glass beads and the specimen was rodded and the column walls were tapped to reduce voids. When the glass beads reached the required height, the top cap was placed. Three specimens were prepared; see appendix page 132 for details. The average saturated unit weight achieved was 18.7 kN/m^3 with deviation from the average ranging from 0.0% to 0.2%.

6.4 Chosen Method

The two methods showed little variability in saturated unit weight, but higher variability was recorded with the dumping method. Therefore the stage-fill method was used to prepare the specimens for testing. A more robust method of sample preparation would involve the use of a vibration table for the initial seating and preparation of the glass beads as seen in work done by Patel et al. (2008).

CHAPTER 7

BASELINE TESTING GLASS BEADS IN WATER

This chapter addresses testing the system with water-saturated glass beads, to establish baseline seismic responses.

7.1 Test Setup and Preparation

Testing was conducted and baseline seismic responses were established in saturated glass beads by replicating the method presented by Rajabdeen et al. (2011). The specimen was prepared using the stage fill method. Once constructed, the water in the specimen was allowed to drain by gravity and was then refilled from the bottom. The purpose of this cycle is to soak and seat the glass beads. A first set of trials which consisted of three test methods was conducted (described below); each test method consisted of three repetitions, where 1000 recordings were averaged per repetition. The specimen was then drained again, re-wetted, and a duplicate set of trials was carried out to investigate repeatability. Three identical specimens were prepared and tested in this fashion.

The mass of water drained and added was measured at each stage. Under soaked conditions the specimen had an average saturated unit weight of 18.5 kN/m^3 and held an average of 30% water by weight; see appendix 1, page 133 for details. Variation between the saturated unit weights of consecutive tests was negligible.

7.2 Testing Methodology

The first step with the testing was to find the resonance frequency of the bender elements in the saturated glass beads. The resonance frequency was found by running a frequency sweep over a broad range from 0 to 30 kHz, and viewing the amplitude spectrum (Fig. 7.1). The peak amplitude occurred at approximately 8 kHz. The actuated signals were tailored to highlight either P-waves or S-waves. Operating at higher frequencies aids in analyzing P-waves (Deniz, 2008), and operating at lower frequencies aids in analyzing S-waves. For testing glass bead specimens with this system, the high and low frequency ranges were determined experimentally as presented in the results sections to follow. The source signal was amplified by a linear signal amplifier from 10 V to 30 V, to increase the signal-to-noise ratio.

7.3 Data Processing

The testing system was optimized to mitigate external noise. Preliminary tests were carried out without filtering (Fig. 7.2). The results show a low frequency background signal upon which the high frequency pulse signal is riding. An FFT of the received signal showed the background frequency was 38 Hz, which is close to the background frequency recorded when testing in air with no filtering (32 Hz). To remove this effect a high pass filter with a cut off frequency at 200 Hz was applied (Fig. 7.3); this value was found by trial and error. This high pass filter was applied for the rest of the tests

presented in this report. All the test result plots not presented in the main body of this report are in appendix 2.

7.4 Pulse Signals to Highlight P-Waves

Pulse testing was started at 8 kHz to identify a baseline seismic response for P-wave propagation; 8 kHz was chosen to approximately match the resonant frequency of the embedded bender elements. To maximize the time between the 8 kHz sine pulses and still capture the entire received signal, an interval of 15 ms was used. The interval was increased by 5 ms from the tests carried out in air and water, which showed residual effects of the first pulse obstructing the second pulse arrival. If the interval between pulses was increased any further, the entire received signal of the second pulse could not be recorded.

The results presented in Fig. 7.3 show overlaid plots of two trials on a specimen prepared and tested as described in section 7.1. The pulse interval was such that energy from each pulse had decayed to where it appeared to have minimal effect on the arrival of the subsequent pulse. The impact of the residual energy from one pulse on the onset of the next is demonstrated in appendix 3, by comparing the quiet time in-between pulses to background signals in the absence of any pulse.

Figure 7.4 is a representative result of time-domain testing targeting P-waves, which shows low-amplitude sinusoidal electrical crosstalk coinciding with the actuation of the source pulse and preceding two possible P-wave arrival picks. It should be noted that there is irregularity present at the initiation of the source sine pulse; the clarity of the

source signal can be improved by using a quicker sampling rate. Recall that the crosstalk was also observable in tests in water and showed energy decaying after approximately 0.14 ms (Fig. 5.9). The same is evident in Fig. 7.4, where the amplitude decreases at 0.14 ms until the signal leads into an increase in amplitude at 0.2 ms, which corresponds to a velocity of approximately 840 m/s, assuming a reflected travel path (length 16.5 cm; Fig. 5.4). Another significant increase in amplitude is seen corresponding to approximately 560 m/s (assuming a reflected travel path). This amplitude is clearly greater than the arrival corresponding to 840 m/s, and is judged as a separate second arrival.

The observed responses relate to the fast and slow P-waves first described by Biot (1956). Fast P-waves represent energy travelling through the pore fluid and slow P-waves represent energy travelling through the skeletal structure of the saturated granular media (Nakagawa et al., 1997). Slow P-waves have been difficult to detect in geomaterials, but have been well documented in artificial porous media such as glass beads (Nakagawa et al., 1997). Slow P-wave transmission through saturated glass beads has also been well documented by Plona (1980) and Plona et al. (1990), among others.

A fast P-wave travels in water at approximately 1480 m/s (e.g. Santamarina et al., 2001). Such an arrival in the current study, be it by direct or reflected path, would be masked by the crosstalk (Fig. 7.4). We conclude that the apparent arrival at the time corresponding to a velocity of 840 m/s is an aftereffect of the fast P-wave following a reflected path. The slow P-wave arrivals are not obscured by the crosstalk.

The velocities corresponding to the slow P-wave arrivals average 560 m/s (Table 7.1; Fig. 7.5). This value agrees reasonably well with the test results of Nakagawa et al. (1996) who measured slow P-wave velocity in a saturated sand sample at 200 – 500 m/s.

Consistency of testing configuration (e.g., placing glass beads, installing top cap) can be evaluated by considering differences in computed slow P-wave velocity between specimen preparations (Table 7.1). Deviations of slow P-wave velocities of the three specimens from the mean were no larger than 0.2 percent. The largest deviation represented just two time samples in the time history.

Referring to Fig. 7.4, test results from the first and second trials appear similar. Amplitudes are generally larger for trial 1. Phase shifts are noticeable but small and they do not become significant until well after the first arrivals. The time histories of the two trials are consistent from 0 to 0.7 ms. From 0.7 to 0.9 ms the shapes differ, but differences disappear for the largest energy excursion which peaks for both trials at about 1 ms. This large amplitude peak observed at 1 ms indicates the presence of a standing wave, and resonance effects. The standing wave appears at a different time from the tests in water, which occurred between 0.3 and 0.5 ms (section 5.4). This is because the different testing media in the two cases have different effects on the resonating wave.

To quantify the difference in amplitude between the signals of trials 1 and 2, the amplitude of the peak immediately following the slow P-wave arrival for each signal was noted (Fig. 7.6). The differences between the amplitudes of the peak points between trials (P1 and P2) are presented in Table 7.2 and Fig. 7.7. Amplitudes from trial 1 (P1) are 26% larger on average than from trial 2. Further, amplitudes of trial 1, ranging from 0.17 to 0.44 V, are more variable than trial 2 (P2), which range from 0.19 to 0.25 V. The range of amplitudes from trial 2 will be used as the baseline against which variances in the presence of nanoparticles will be compared. Specifically, peak slow P-wave amplitudes

outside the range 0.19 to 0.25 V will be taken as indication that the nanoparticles are affecting the measurement.

7.5 Pulse Signals to Highlight S-Waves

An optimum frequency for actuating pulse signals to highlight S-wave energy was found through experimentation. The results are presented in Fig. 7.8, which shows source actuation frequency increased from 1 kHz to 4 kHz in 1 kHz increments. A starting frequency of 1 kHz was used because this is the lowest possible actuation frequency when using a burst function with the function generator. The S-wave train became progressively more contaminated with high frequency energy with increasing actuation energy. The source frequency chosen for testing was 1 kHz.

Figure 7.9 shows a received signal for 1 kHz pulses actuated at 15 ms intervals. Decaying energy from the preceding pulse appears to still be present as the new pulse is received. The effects of the residual energy of the preceding pulse on the background noise are presented in appendix 3.

Figure 7.10 shows the anticipated shear wave arrival, the presence of near-field effects on received signals, and the first arrival picks that were made. The onset of the direct-transmission S-wave is obvious from its shape, although its arrival is preceded by low amplitude near-field effects. In this report, all the first arrival picks of the shear wave (direct travel path) were made at the first data point with positive amplitude in the onset shear wave energy. An arrival corresponding to the anticipated shear wave velocity (150 m/s) occurs at the beginning of what we interpret to be near-field effects. The reference

velocity was taken from the work of Patel et al. (2009) which does not acknowledge near-field effects. According to Arroyo et al. (2003), if near-field effects are not accounted for, typically shear wave velocity is overestimated. In this study, the direct travel path length (tip-to-tip distance (L)) was used to calculate S-wave velocities (Table 7.1 and Fig. 7.11). By accounting for near-field effects and given the picking algorithm, the shear wave velocities determined were between 25 and 35 m/s, which were much slower than anticipated values.

For each specimen, the S-wave velocities among repetitions differ by an average of 1.5%. Velocities are 5 to 13% higher for the second trial than the first trial. This consistent difference implies that the process of repetitive wetting and draining of the glass beads continually improves their seating. Such an effect would logically be visible with the S-waves and slow P-waves, which are both dependent upon the skeletal structure, but not with fast P-waves which depend only on the pore fluid. The fact that we observed this effect with S-waves but not slow P-waves needs further examination. The difference in velocities measured between the two trials implies that a change in S-wave velocity caused by the introduction of an experimental treatment would have to be larger than 13% or smaller than 5% to be detected with the system as it was configured in this initial test. Increasing the number of wetting and draining cycles prior to taking any measurements might decrease this sensitivity threshold.

Considering the measured shear wave velocity and the source actuation frequency of 1 kHz, the S-wavelengths ranged between 24 and 30 mm. The L values used for the testing were 61.2 mm on average and always greater than 60 mm; see appendix 1 page

135 for details. Thus the test design satisfied the criterion presented in Section 2.4 that L must be greater than two wavelengths.

To quantify the difference in amplitude between the received signals of trials 1 and 2, the peak-to-peak amplitudes of the S-wave pulse (ΔP) (Fig. 7.12) were observed (Table 7.2 and Fig. 7.13). Contrary to observations of the slow P waves, differences in amplitude between the two trials were not consistent. However, consistent with observations of the slow P waves, amplitudes of trial 1 (ΔP1), ranging from 1.20 to 2.41 V, are more variable than trial 2 (ΔP2), which range from 2.07 to 2.36 V. The range of amplitudes from trial 2 will be used as the baseline against which variances in the presence of nanoparticles will be compared. Specifically, peak-to-peak S-wave signal amplitude outside the range 2.07 to 2.36 V will be taken as indication that the nanoparticles are affecting the measurement.

7.6 Frequency Sweep Method

Frequency sweeps were run from 0 to 30 kHz. Figure 7.14 shows an example of the coherence plot, where for the most part, the coherence remains above 0.9 from 7 to 25 kHz for both trials.

7.6.1 Amplitude Spectrum Results

The Fourier amplitude spectra from first and second trials, computed using the dynamic signal analyzer, were compared by overlaying the two plots. The representative results are presented in Fig. 7.15. For all specimens, the spectra peak at 8 kHz (the resonant frequency of the potted bender elements) after which amplitude decreases

gradually. Two sharp dips in amplitude appear at approximately 11 and 13 kHz. Over the range where coherence was high, differences in spectral amplitude between the first and second trials were small. To quantify the sensitivity between trials, the difference between the amplitudes of the trials was found; these are referred to as the residual signals (Fig. 7.16). The residual signals of the three specimens were averaged to get a baseline residual signal between 7 and 25 kHz, to represent the difference between the two trials using only distilled water. For the presence of nanoparticles to be detected with this method, they would have to cause perturbations large enough to deviate significantly from this baseline signal.

7.6.2 Phase Angle Results

The phase component of the frequency domain data was observed by Da Fonseca et al. (2008) with bender-element testing on granitic residual soil and Toyoura sand using a triaxial testing apparatus. The authors reviewed common methods used for testing with and interpreting bender element data, and proposed an outline for testing to obtain reliable travel times. The method considers the slope of a best-fit straight line of the unwrapped phase angle against frequency over a selected frequency range demonstrating high coherence. This method of analysis is applied only to determine the travel time and velocity of the signal and not other aspects of the signature, although visual or computational comparisons of phase might be useful to document responses to experimental treatments.

For this study, the phase angles from the frequency sweeps were unwrapped using a function available on the signal analyzer. A representative result is presented in Fig. 7.17.

The plots do not give a single, simple, linear slope as was obtained by Da Fonseca et al. (2008). The four measurement results are offset with respect to one another but more or less parallel in the range of high coherence. Dips and rises in the phase angles disrupt the linearity, and different gradients of the slopes are observed. By visual inspection, the different gradients represented credible shear wave velocities, ranging from 70 to 200 m/s. However, the different gradients and velocities lend uncertainty. These differences from the more straightforward results reported by Da Fonseca et al. (2008) might be attributed to the fact that their testing was conducted on homogenous specimens in a triaxial apparatus under elevated effective stresses. This topic was not pursued any further in this study, but merits further investigation.

7.7 Summary: Detection Criteria

From the baseline tests carried out in this chapter, the following criteria to evaluate the detectability of nanoparticle dispersions are proposed. These criteria are tested in Chapter 8.

1. Water trial results: If results (applied to four tests: velocities and amplitudes from P- and S-waves) from two or more of three repetitions from the water trial are outside the range obtained for trial 1 (Chapter 7) by 5% or more, the water trial fails the test. Otherwise, the water trial is accepted.

2. Nano trial results:
    - Slow P-waves:
        - If the velocity deviates by more than 1% from the mean of the trial 2 baseline velocities (Chapter 7), the nanoparticle dispersion is detectible.
        - If significant phase differences between the received signals of the consecutive water and nano trials of a specimen exist, the nanoparticle dispersion is considered detectible. The degree of significance assessed is strictly qualitative, from visual inspection. Further testing would be required before quantitative criteria can be established.
        - If the zero-to-peak amplitude of the peak directly following the first arrival deviates by more than 5% from the range 0.190 to 0.248 V, the nanoparticle dispersion is detectible.
    - S-waves:
        - If the velocity is less than 5.3% quicker than the water trial velocity or more than 13.7% quicker than the water trial velocity, the nanoparticle dispersion is detectible. These numbers represent the extreme values of measured difference between trials 1 and 2 (Chapter 7), incremented by 5%.
        - If the peak-to-peak amplitude deviates by more than 5% from the range 2.07 to 2.36 V, the nanoparticle dispersion is detectible. These numbers represent the extreme values of trial 2 amplitudes (Chapter 7).

- Spectral response: If significant amplitude differences between the residual signal (from consecutive water and nano trials of a specimen, in the high coherence range of 7 to 25 kHz) and the baseline residual (Chapter 7) exist, the nanoparticle dispersion is considered detectible. As with phase difference evaluations, amplitude differences are strictly qualitative, from visual inspection, and further testing would be required before quantitative criteria can be established.

Table 7.1. Velocities associated with received pulse signals for water-saturated glass bead specimens

Specimen	Repetition	Compression (slow P-wave): 8 kHz pulse			Shear (S-wave): 1 kHz pulse		
		Trial 1 (m/s)	Trial 2 (m/s)*	Difference	Trial 1 (m/s)	Trial 2 (m/s)*	Difference**
1	1	562.4	562.4	0%	28.2	32.2	12%
	2				28.4	32.4	12%
	3				28.4	32.2	12%
2	1	560.3	560.3	0%	23.9	25.4	6%
	2				24.1	25.3	5%
	3				24.1	25.3	5%
3	1	561.0	561.0	0%	29.3	33.8	13%
	2				29.6	33.8	12%
	3				29.5	33.6	12%

*Trial 2 represents duplicate tests following drainage and rewetting of test specimen.
**Difference is Trial 2 relative to Trial 1

Table 7.2. Amplitudes associated with received signals for water-saturated glass bead specimens

Specimen	Repetition	Compression (slow P-wave): 8 kHz pulse			Shear (S-wave): 1 kHz pulse		
		Trial 1 (P1,V)	Trial 2 (P2,V)*	Difference	Trial 1 (ΔP1,V)	Trial 2 (ΔP2,V)*	Difference**
1	1	0.174	0.194	12%	2.41	2.07	-14%
	2	0.230	0.190	-18%	2.39	2.23	-7%
	3	0.267	0.185	-31%	2.40	2.19	-9%
2	1	0.379	0.219	-42%	1.94	2.19	13%
	2	0.327	0.201	-39%	2.06	2.18	6%
	3	0.350	0.228	-35%	2.09	2.17	4%
3	1	0.233	0.248	6%	1.20	2.34	95%
	2	0.416	0.221	-47%	1.75	2.34	34%
	3	0.441	0.242	-45%	1.86	2.36	27%

*Trial 2 represents duplicate tests following drainage and rewetting of test specimen.
**Difference is Trial 2 relative to Trial 1

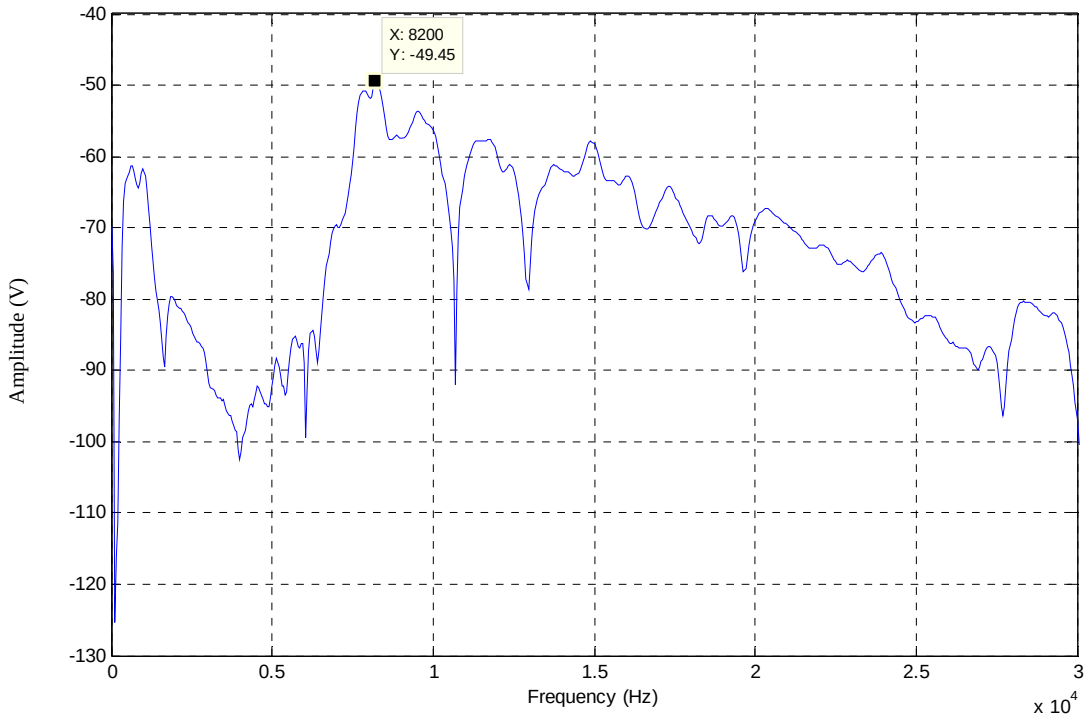

Figure 7.1. Frequency response for a 0-to-30 kHz sweep showing the resonance frequency of the bender element in a water-saturated glass bead specimen; result of 1000 recordings averaged, with no filtering applied.

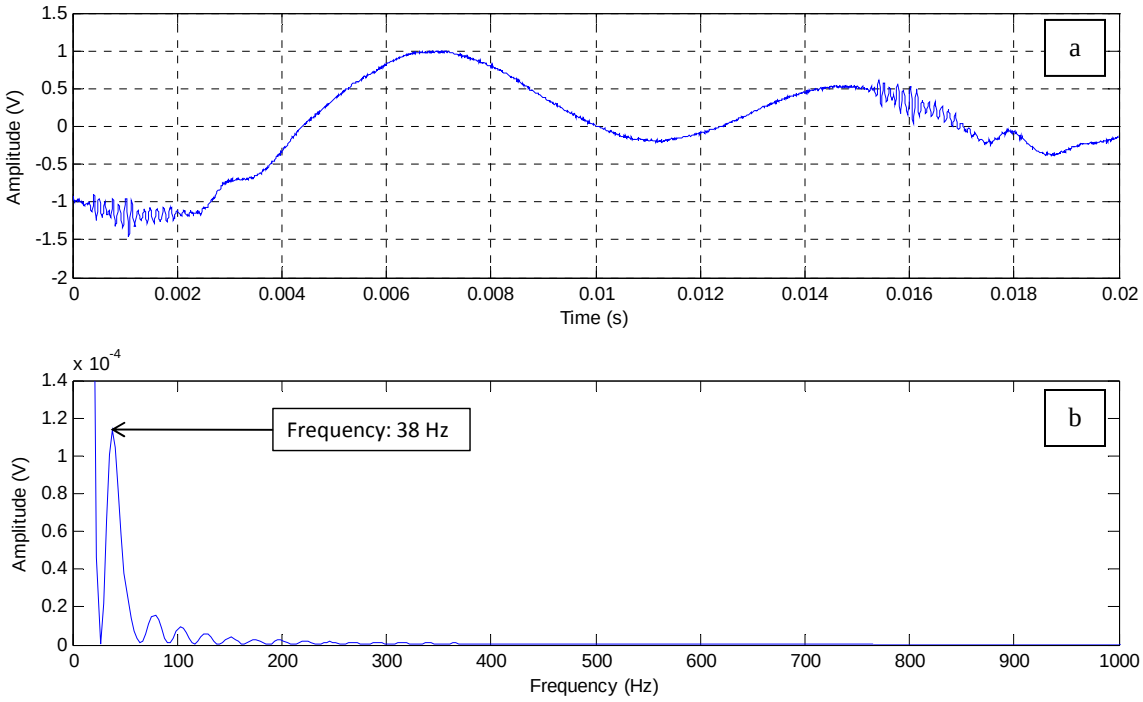

Figure 7.2. 8 kHz pulse signal (1000 recordings averaged) in a saturated glass bead specimen with no filter applied.

a: Time domain result showing low frequency carrier signal
b: Fourier amplitude spectrum to 1 kHz showing dominant carrier frequency at 38 Hz

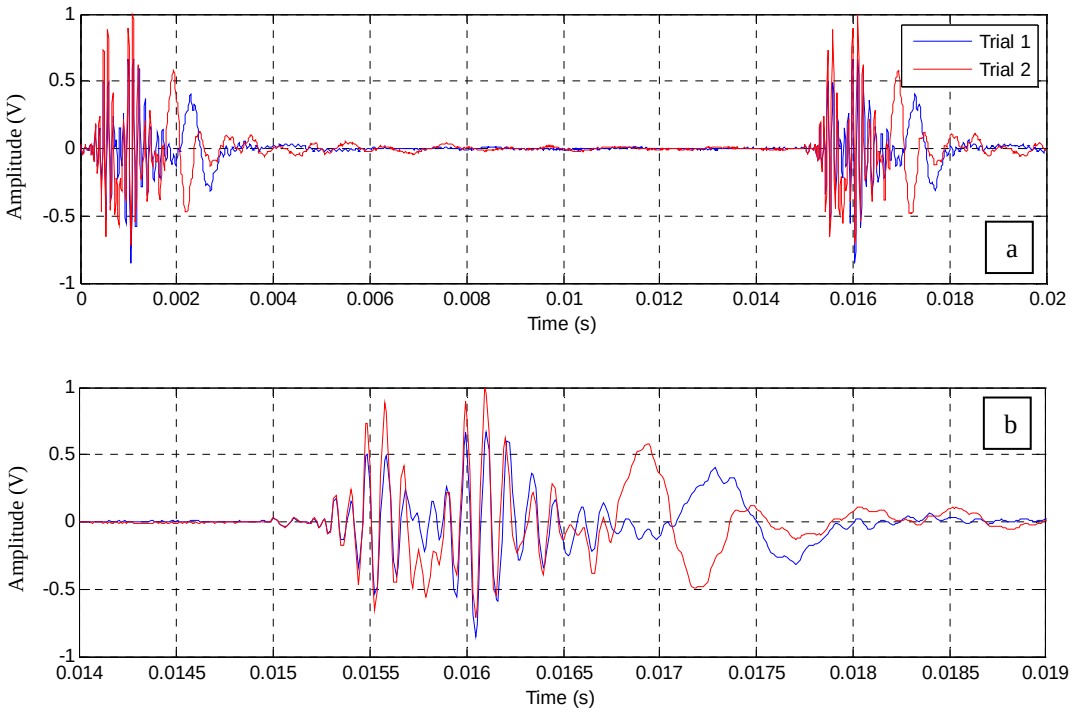

Figure 7.3. Representative result for consecutive 8 kHz pulses with 200 Hz high-pass filter applied, received signals of first and second trials are shown; result of 1000 recordings averaged for each.

a: Received signals showing two consecutive pulses and quiet time between pulses;
b: Detail view of a received pulse

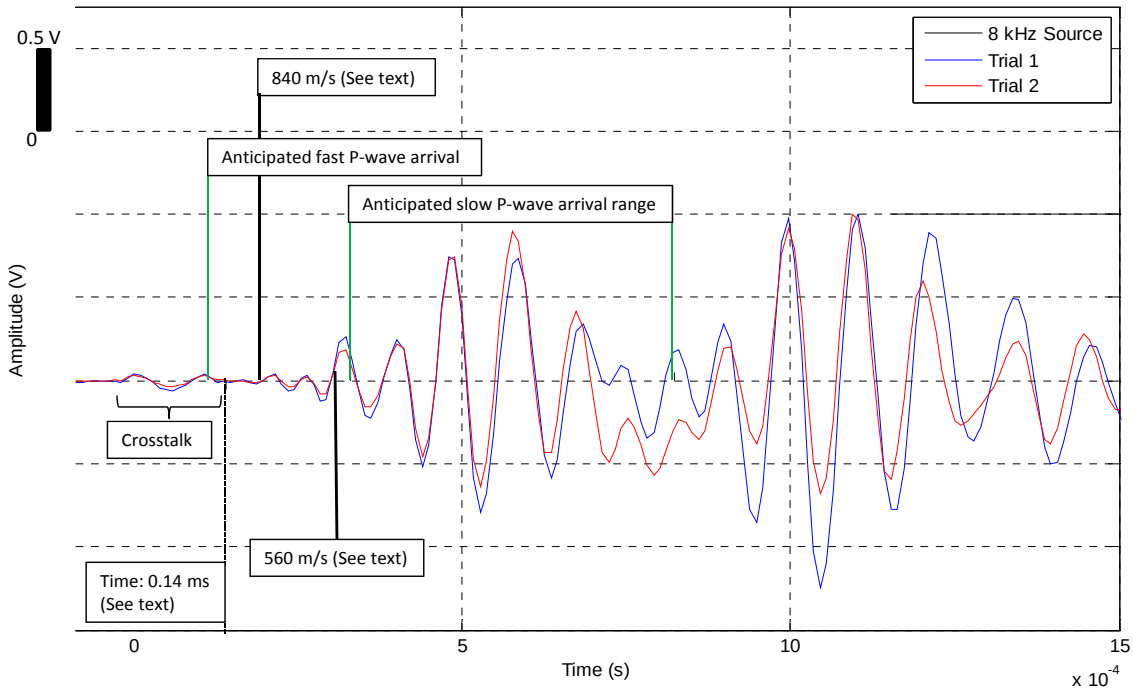

Figure 7.4. Representative result of an 8 kHz sine pulse and received signals of 1000 recordings averaged for each, emphasizing reflected-path P-wave propagation. Trials 1 and 2 are conducted sequentially under near-identical test conditions. Note the irregularity present at the initiation of the source sine pulse.

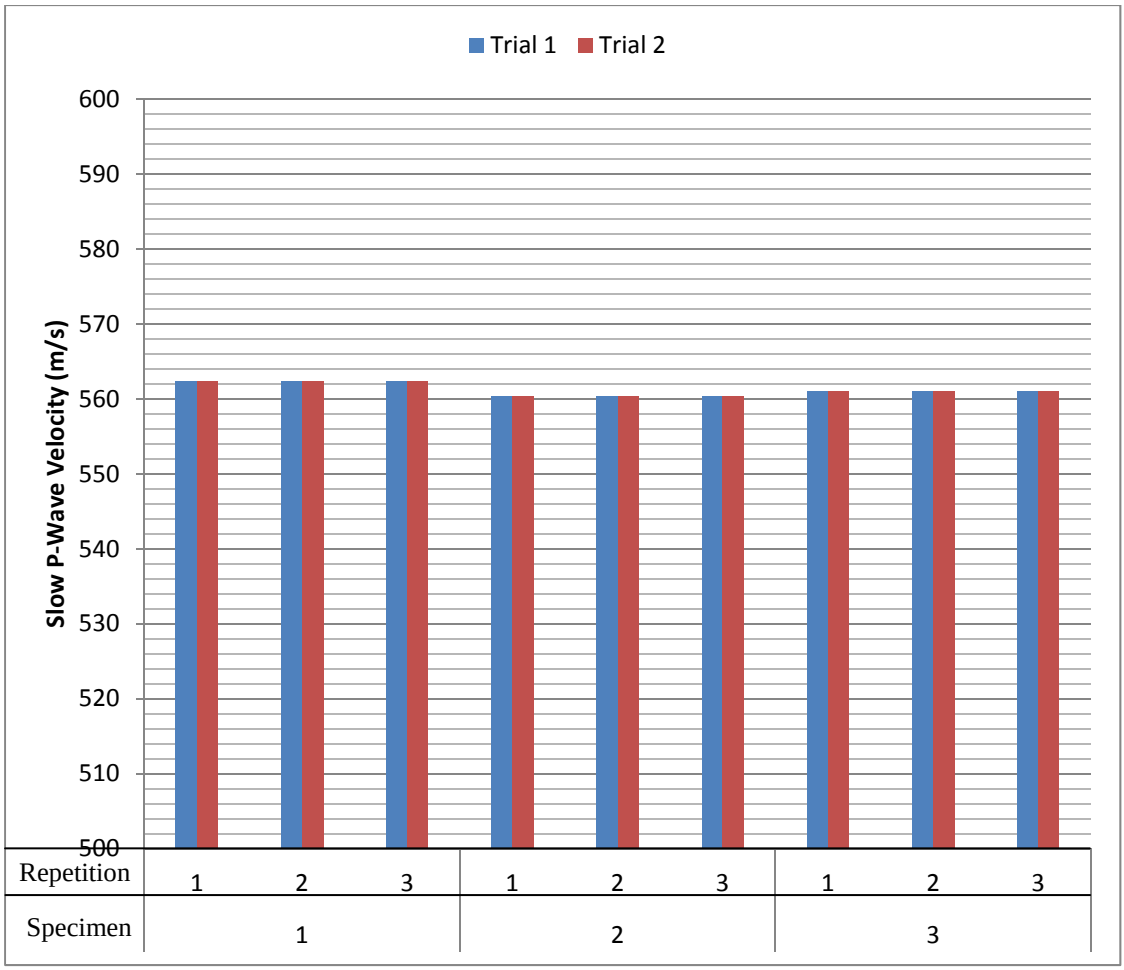

Figure 7.5. Summary of 8 kHz sine pulse highlighting P-wave velocities in water-saturated glass bead specimens.

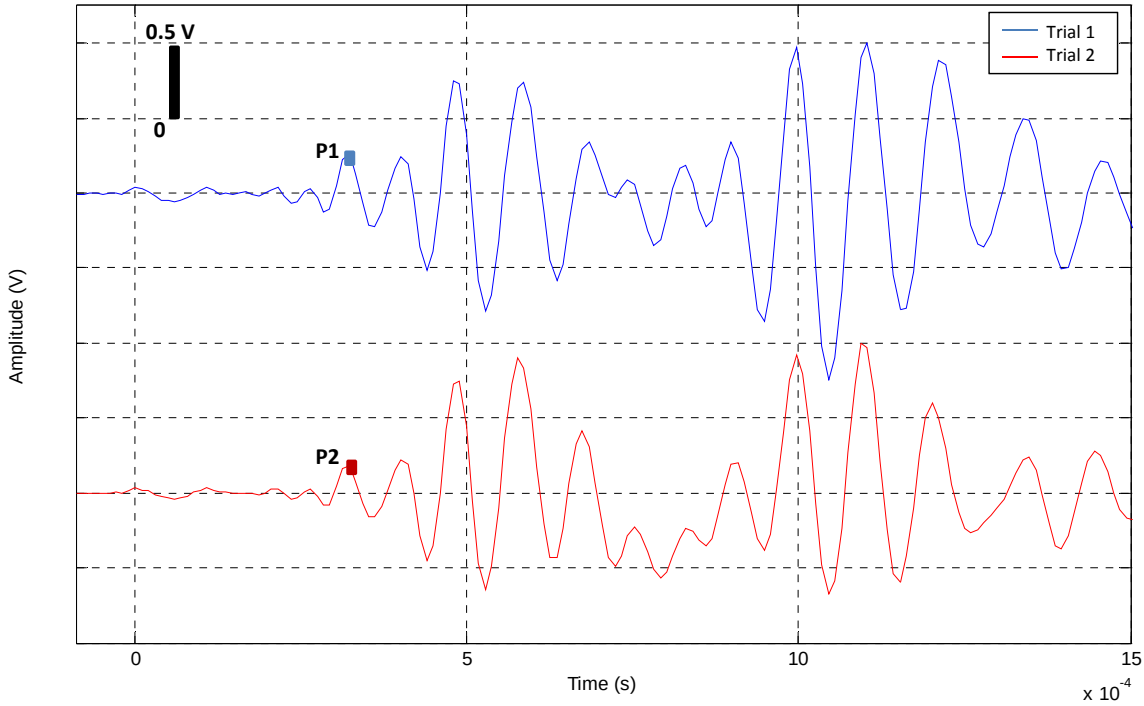

Figure 7.6. Representative picks of characteristic points used to compare the amplitudes of received slow P-wave signals, 1000 averages and 200 Hz high-pass filter.

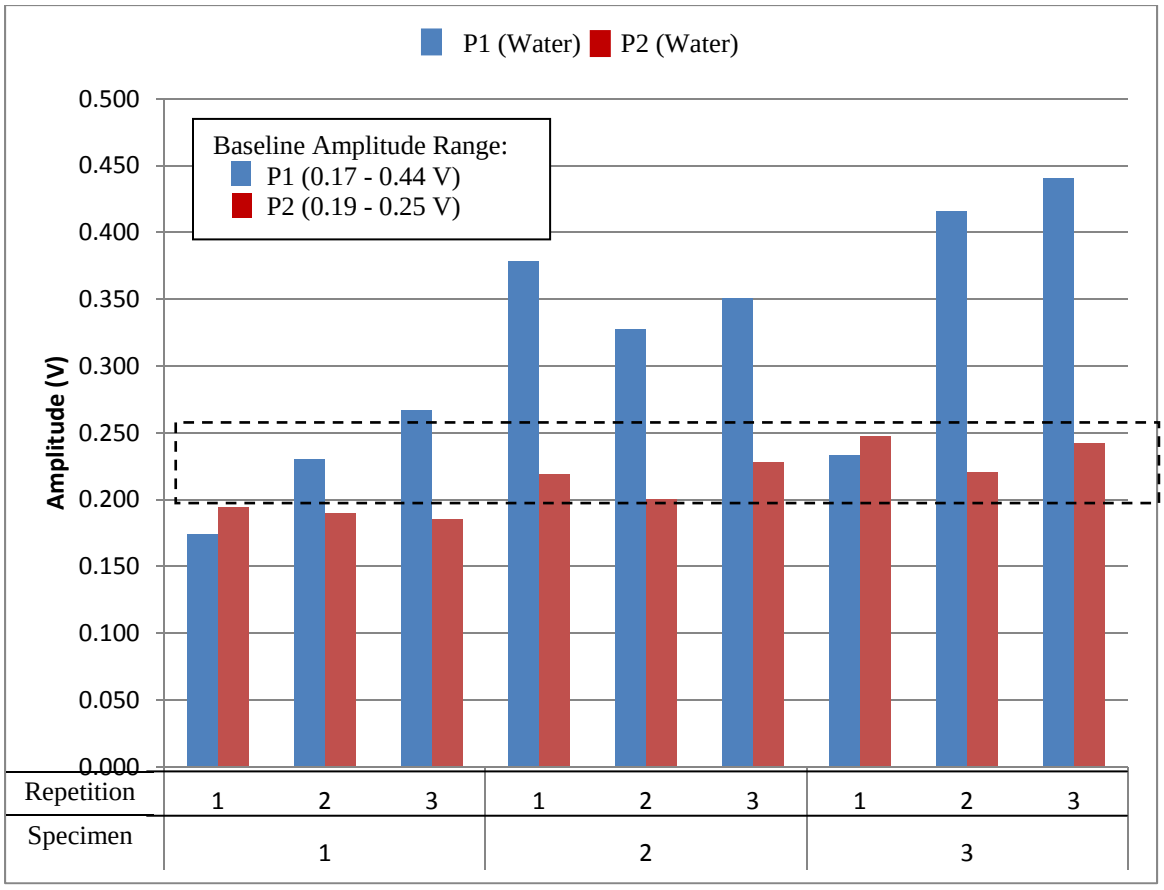

Figure 7.7. Summary of received signal amplitudes of characteristic points (described in text) from 8 kHz pulse signals highlighting P-waves in water-soaked glass bead specimens.

P1 refers to the amplitude values of P-waves from trial 1, P2 refers to the amplitude values of P-waves from trial 2, and the black dashed lines show the P2 amplitude range that defines the baseline for nano testing (chapter 8).

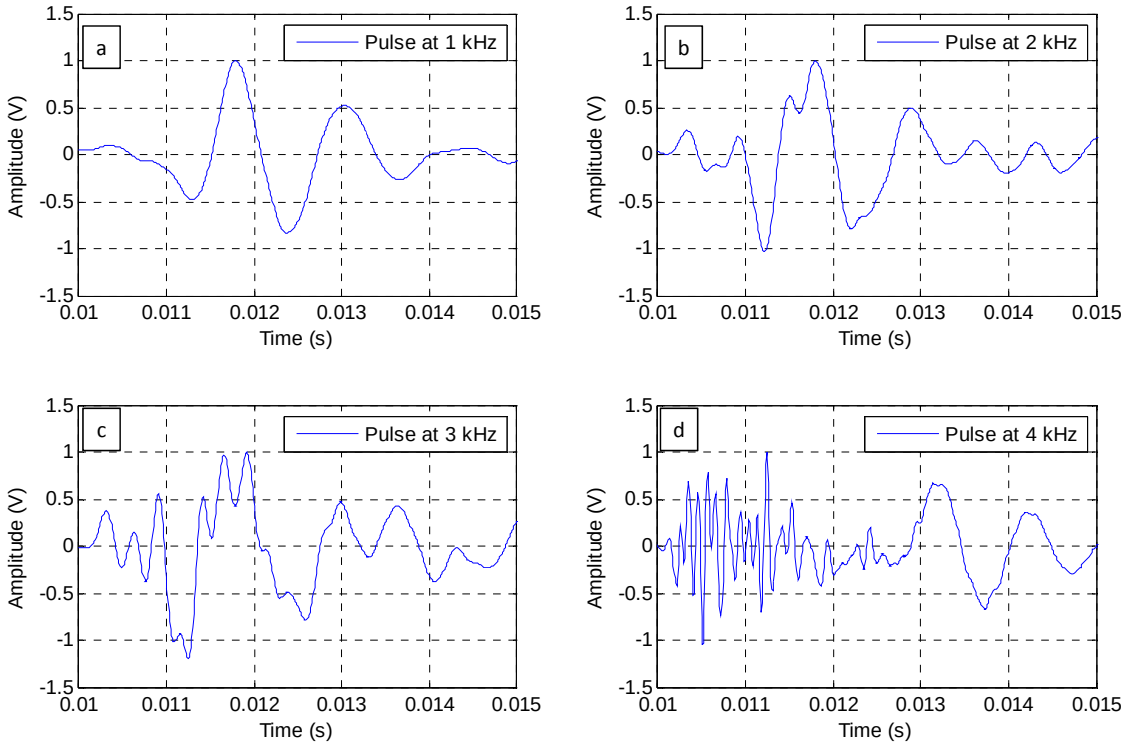

Figure 7.8. Check for optimal sine pulse frequency to test for shear in saturated glass beads; received signals are 1 repetition of 1000 recordings averaged per repetition, under 200 Hz high-pass filter.

a: Sine pulse at 1 kHz showing S-wave;
b: Sine pulse at 2 kHz showing S-wave, but not clearly;
c: Sine pulse at 3 kHz showing weak S-wave;
d: Sine pulse at 4 kHz showing dominant high frequency energy.

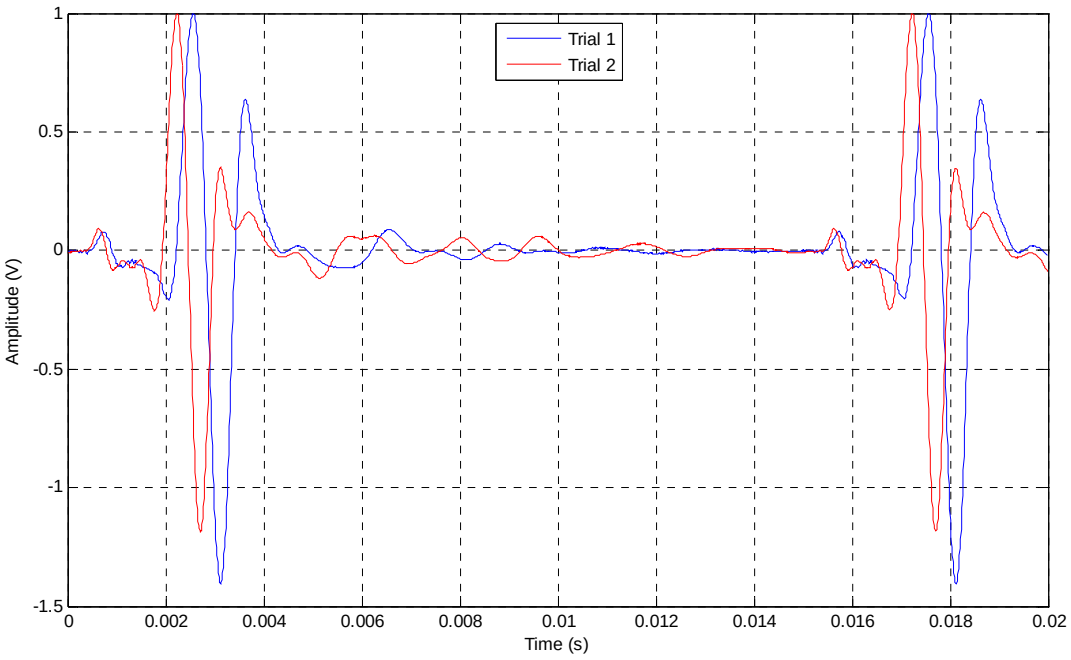

Figure 7.9. Representative result of a 1 kHz sine pulse test in saturated glass beads showing two consecutive pulses, demonstrating that disturbances due to the first pulse do not completely decay prior to the arrival of the second pulse. A single repetition from each trial is shown; 1000 recordings averaged per repetition.

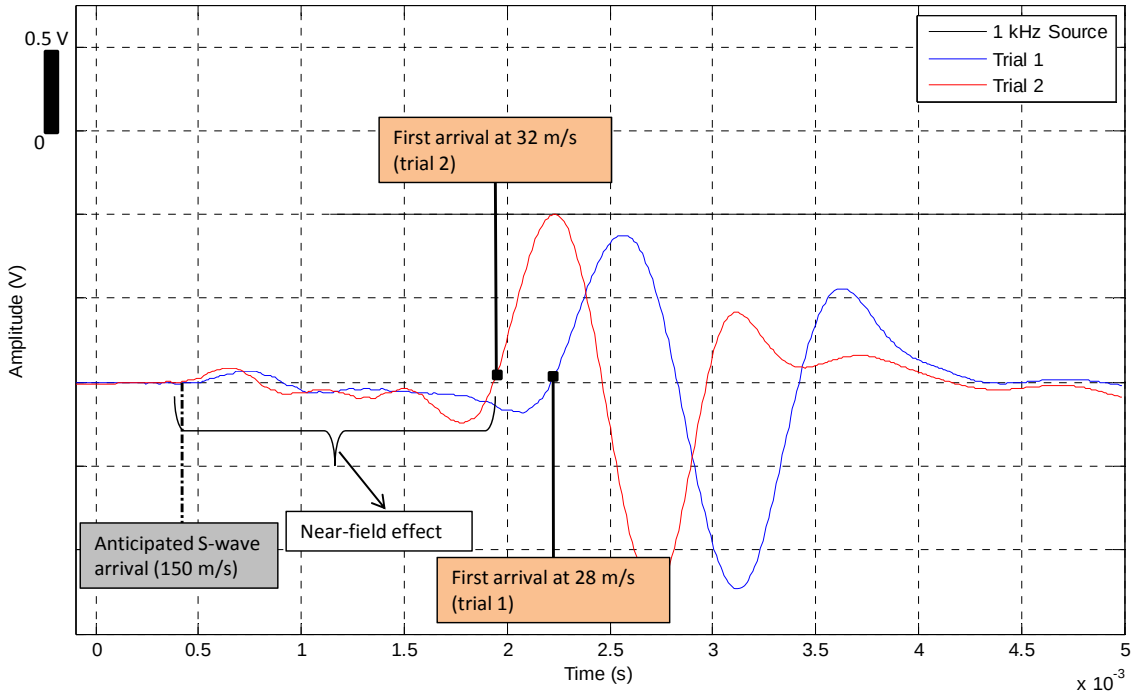

Figure 7.10. Representative result of 1 kHz sine pulse (shear); shows near-field effects, trial 2 first arrival earlier than trial 1 arrival; single repetition of 1000 recordings averaged per repetition, 200 Hz high-pass filter.

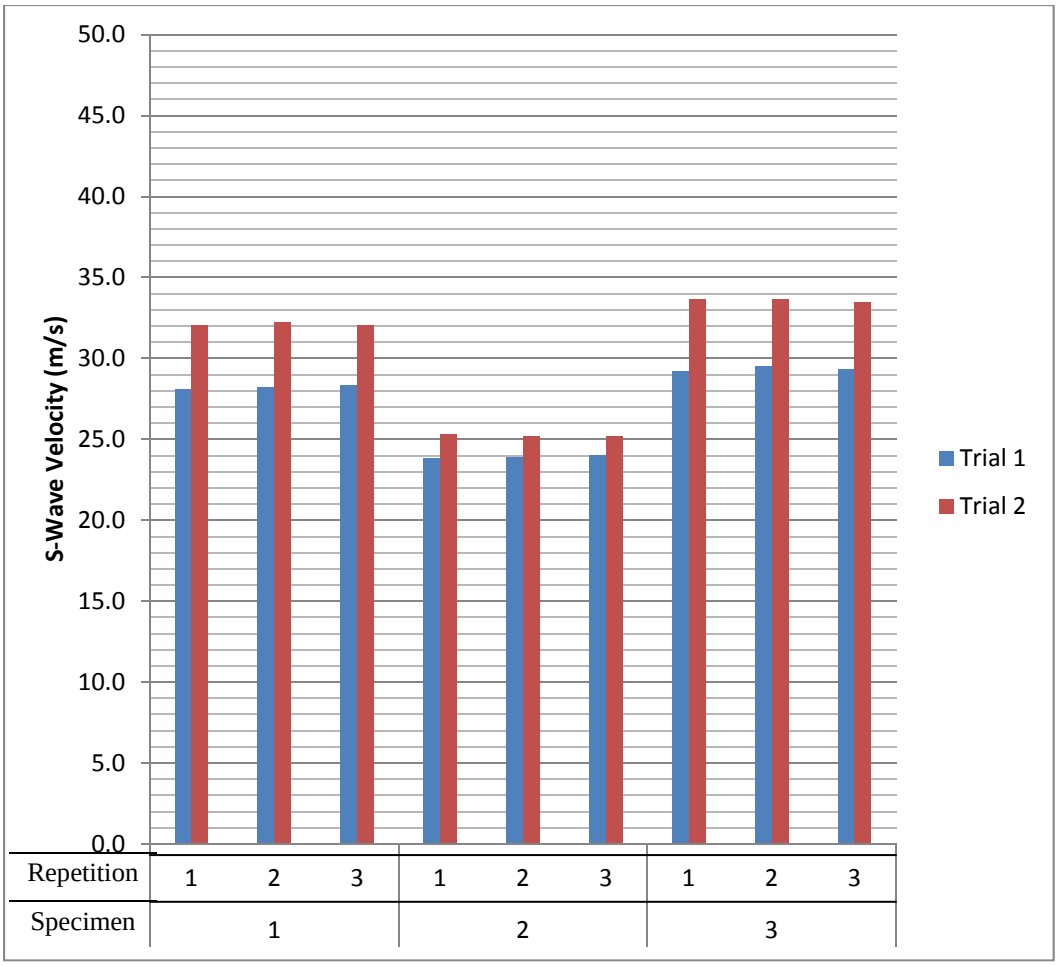

Figure 7.11. Summary of 1 kHz sine pulse highlighting S-wave (shear) received signal velocities in water-saturated glass bead specimens.

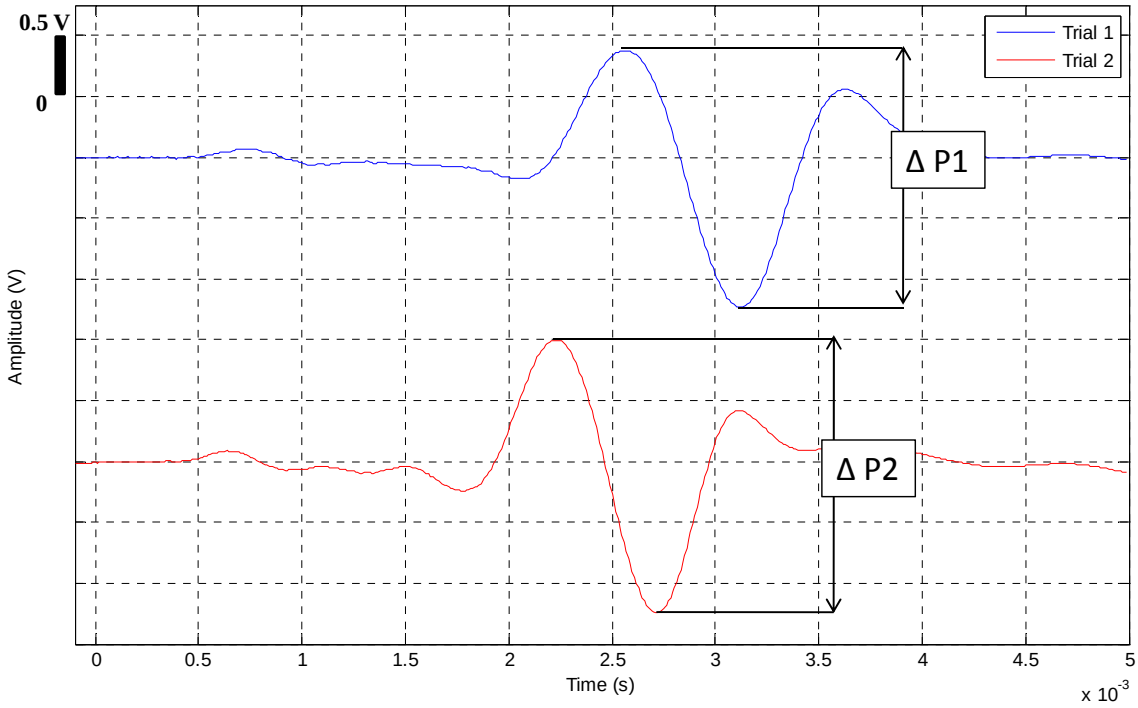

Figure 7.12. Representative picks of characteristic points used to compare the amplitudes of received S-wave signals, 1000 averages and 200 Hz high-pass filter.

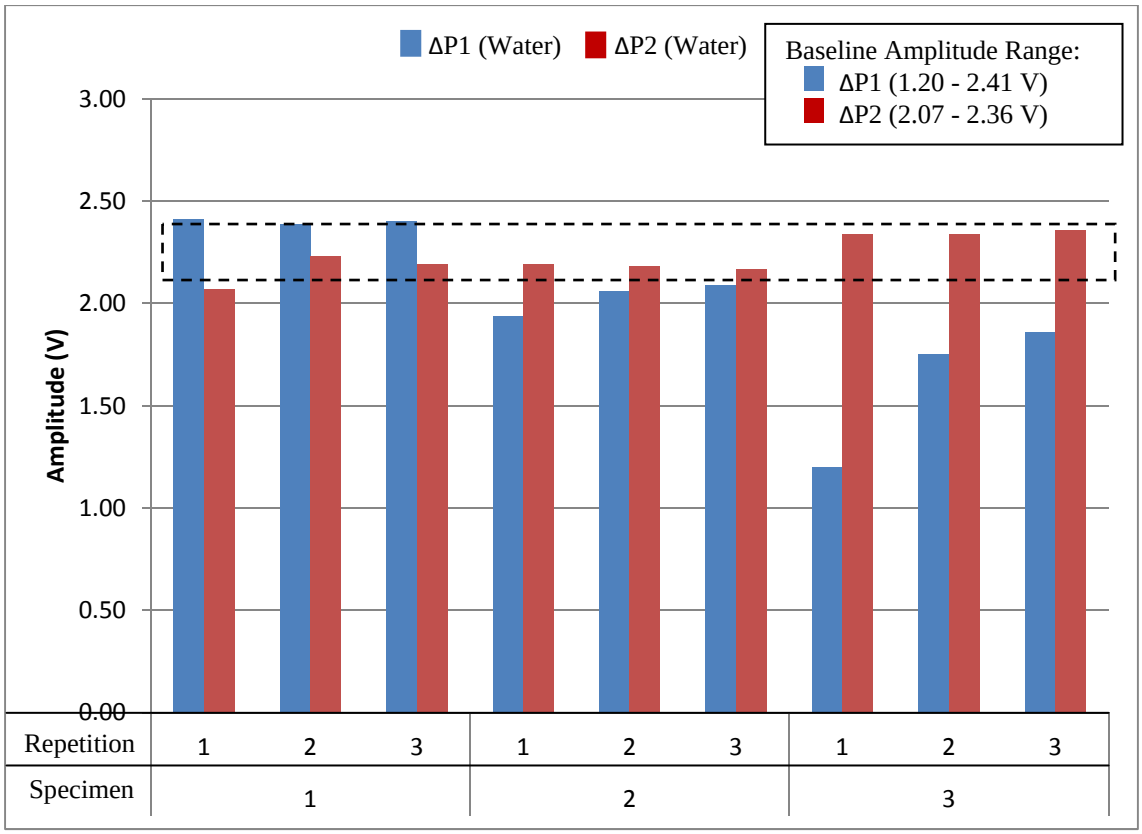

Figure 7.13. Summary of received-signal peak-to-peak amplitude differences from 1 kHz pulse signals highlighting S-waves in water-saturated glass bead specimens.

ΔP1 refers to the peak-to-peak amplitude of S-waves from trial 1 and ΔP2 refers to the peak-to-peak amplitude of S-waves from trial 2. The black dashed lines show the ΔP2 range, which defines the baseline for nano testing (chapter 8).

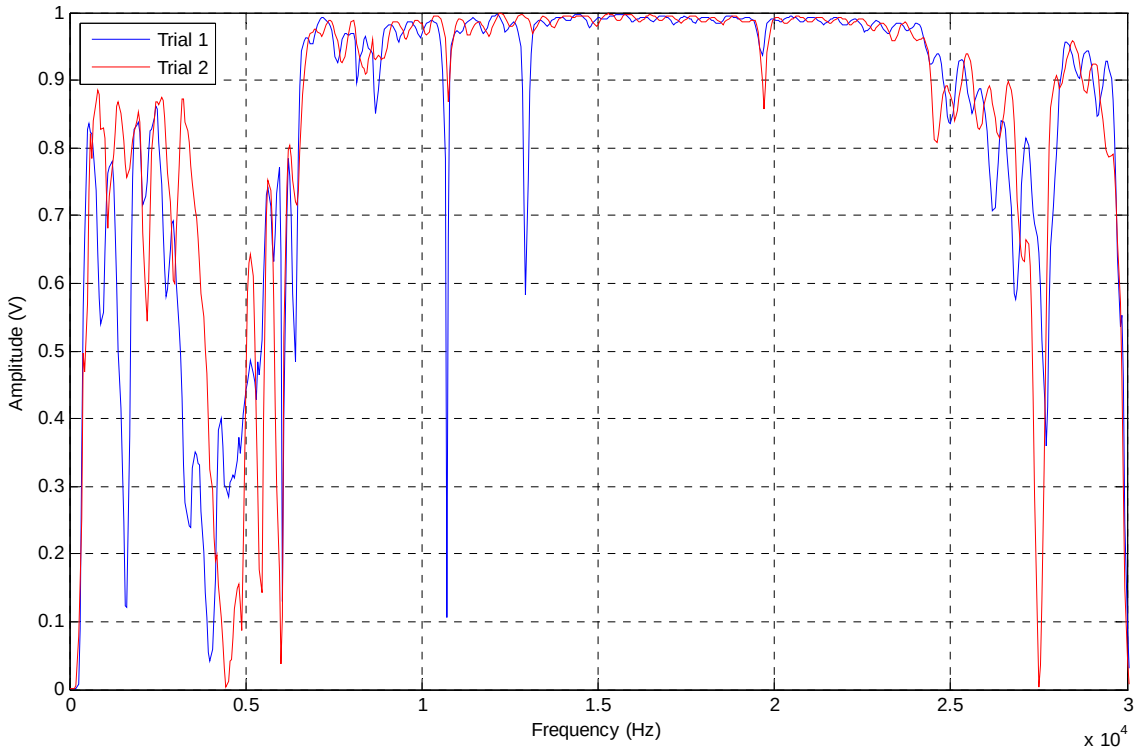

Figure 7.14. Representative coherence for 30 kHz sweep with 200 Hz high-pass filter in a water-saturated glass bead specimen, showing result of 1000 recordings averaged each, for Trials 1 and 2.

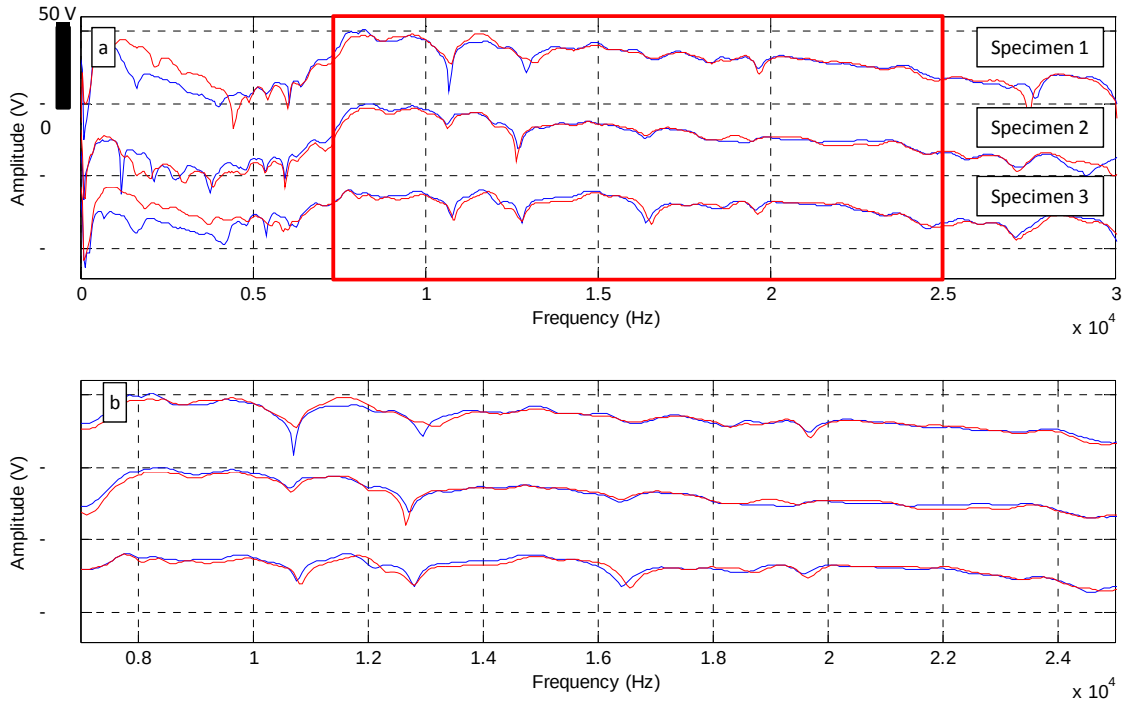

Figure 7.15. Representative amplitude spectrum of 30 kHz sweep for all water-saturated glass bead specimens; 1000 recordings averaged per repetition.

a: Shows entire frequency spectrum for the 30 kHz sweep, the box indicates the enlarged area for (b);
b: Shows the frequency range (7 to 25 kHz) analyzed to establish a repeatable signature between Trial 1 and Trial 2.

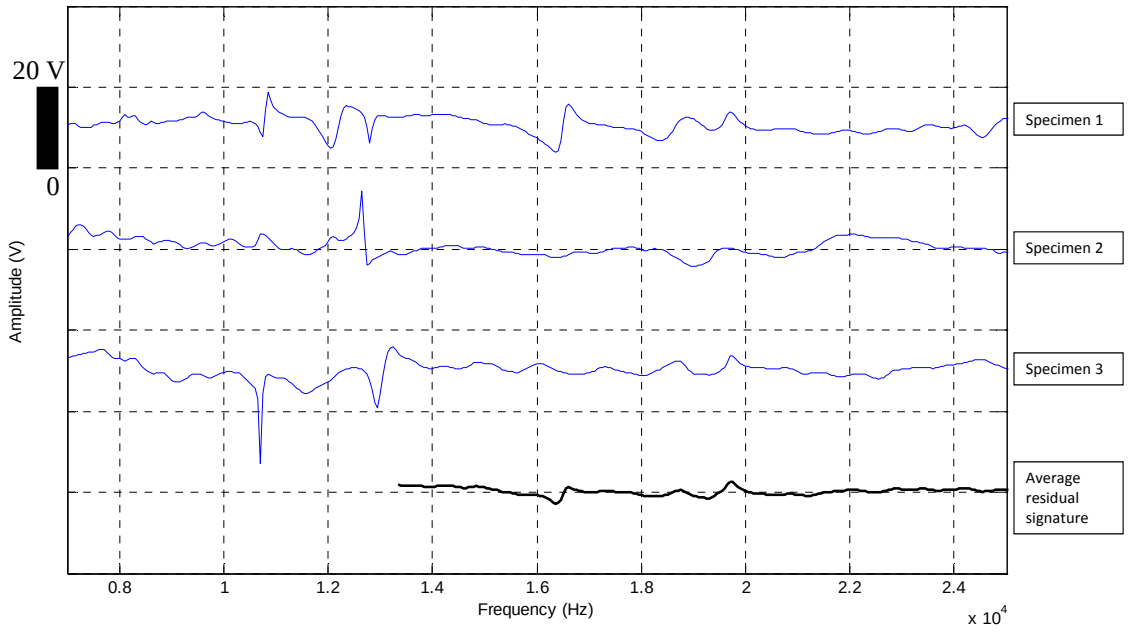

Figure 7.16. Residual signals equal to the difference between the spectral responses of trial 1 and trial 2 in water-saturated glass bead specimens, used to quantify the sensitivity of the test system. The average residual signal is the averaged result of the three residual signals of the specimens, and it is used as the baseline.

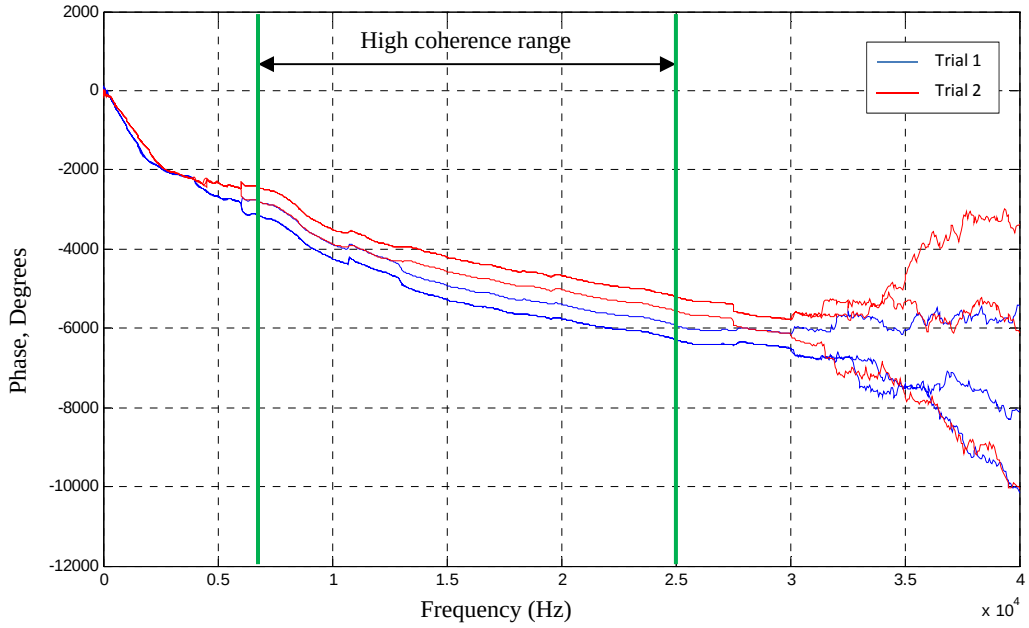

Figure 7.17. Representative result of unwrapped phase angles for trials 1 and 2 in water-saturated glass bead specimen, three repetitions of 1000 recordings averaged per repetition, high-pass filter at 200 Hz applied. Range of high coherence is expected from 7 to 25 kHz.

CHAPTER 8

TESTING WITH NANOPARTICLE DISPERSIONS

The nanoparticle study differed from the testing with glass beads in water described in Chapter 7 only in that nanoparticle dispersions in water were used in place of pure water for the second trial. Those tests with water presented in chapter 7 are referred to here as the baseline tests. The goal of the nanoparticle tests presented in this chapter was to check for responses that were outside of baseline; these might be attributable to the nanoparticles.

Three nanoparticles were tested: 1. zinc oxide (nZnO), 2. titanium dioxide ($nTiO_2$), and 3. silver (nAg). A fourth nanoparticle was also chosen for testing; zero-valent iron (nZVI). The nZVI considered was at 98% purity and in powdered form. After sonicating and preparing a dispersion, it was found that the nZVI settled quickly, in no more than 3 minutes. This implies that a nZVI plume in saturated granular media would not remain dispersed, it would rapidly settle. A dispersion with nZVI could not be created for testing purposes and testing with nZVI was forfeited.

8.1 Test Setup and Preparation

The nanoparticles were purchased from Nanostructured & Amorphous Materials, Inc. (www.nanamor.com). In this study, all concentrations are reported by weight. The oxides were received pre-dispersed in distilled water at concentrations of 20% for nZnO and 40% for $nTiO_2$; they had to be diluted to the required concentrations. The metals were in

powdered form, from which dispersions were created at the required concentrations. The concentrations of the nanoparticle dispersions plumed into the column had to be higher than the required concentration to account for water remaining in the column after draining out the water trial (trial 1). The glass bead specimens retained an average of 240 ml of water after draining, and the average volume of additional fluid required to backfill the specimens for the nano trial (trial 2) was 360 ml. (See appendix 1, page 133 for details.)

8.1.1 Pluming Process

Different methods were used for introducing different nanoparticle dispersions (Fig. 2.7). The nano-oxide dispersions were transferred to a funnel flask, which was placed at a higher elevation than the column so that the dispersion was plumed into the glass-bead-filled column by gravity. The nano-metal dispersions could not be plumed by this process because they clogged the valves in the column plumbing. An alternative method to keep the dispersion homogenized and stable for pluming presented by Joyce (2011) was adopted. The authors used a stirrer and peristaltic pump for pluming nano metal dispersions. We use a sonicator instead of a stirrer to keep the nanoparticles dispersed. The nano-metal dispersions were sonicated during the entire pluming process and no clogging of valves occurred.

8.2 Testing Methodology

The testing methods used were the same as those used for the baseline tests: 8 kHz pulse signals to highlight compression energy in the time domain; 1 kHz pulse signals to highlight shear energy in the time domain; and 30 kHz frequency sweep to observe spectral response. As discussed below, all materials were tested at a concentration in the range 3 to 5 %; in addition, the nZnO was tested at two lower concentrations. Concentrations, fluid volumes and other details of all test specimens are provided in appendix 1, page 134.

Following processes presented in Ch. 7, results of time-domain testing for all nanoparticle dispersions are summarized in Tables 8.1 and 8.2. The 8 kHz pulse testing results for velocity and amplitude are provided in Figures 8.1 and 8.2 respectively. The 1 kHz pulse testing results for velocity and amplitude are provided in Figures 8.3 and 8.4 respectively. Criteria presented in section 7.7 are applied to the results in order to evaluate the detectability of nanoparticle dispersions.

8.3 Validating Water Trials

Recall that the acceptability criterion for the water trials is presented in section 7.7. Compare water trial results against trial 1 results (Chapter 7) for velocities using Tables 8.1 and 7.1 and for amplitudes using Tables 8.2 and 7.2. Only one test failed the acceptance criterion: S-wave velocity for $nTiO_2$, which was 8% below the smallest value measured in trial 1 for all three repetitions.

8.4 Testing with nZnO

Testing with nZnO was conducted at three concentrations. Each set of tests is described below, in order from low to high concentration.

8.4.1 0.03% Concentration

Recall that the nZnO was pre-dispersed with water at 20% concentration. 2 ml of the dispersion was diluted with 498 ml water and placed on a stirrer for approximately 30 minutes to aid dispersion. This process yielded a 500 ml dispersion, of which 400 ml was expected to be required to fill the drained specimen. The following equation presents the dilution of the dispersed nZnO introduced into the column:

$$\left(\frac{0.4 \text{ ml nZnO}}{500 \text{ ml } H_2O + \text{nZnO}}\right) \times 100\% = 0.08\%$$

It was expected that 240 ml of water would remain in the column after draining the specimen following the water trial. This retained water would dilute the concentration of the nZnO further. The total concentration of nZnO in the column:

$$\left(\frac{0.08\% * 400 \text{ ml } (H_2O + \text{nZnO})}{400 \text{ ml } (H_2O + \text{nZnO}) + 240 \text{ ml}(H_2O)}\right) = 0.05\%$$

After draining the water trial, approximately 347 ml was retained in the column. As a result, only 185 ml of the nZnO dispersion was introduced, so that the concentration of nZnO tested was:

$$\left(\frac{0.08\ \% \ * \ 185 \text{ ml } (H_2O + \text{nZnO})}{185 \text{ ml } (H_2O + \text{nZnO}) + 347 \text{ ml } (H_2O)}\right) = 0.03\%$$

Between trials, the volumetric moisture content of the glass bead specimen decreased by 5% and saturated unit weight decreased by 0.55 kN/m^3.

For 8 kHz pulse testing to highlight P-waves, the received signals from the water and the nano trials had minimal divergence in phase, and had identical arrival times of slow compression waves and therefore did not satisfy the detection criteria (Figure 8.5). The nanoparticle dispersion was however considered detectible by P-wave amplitude.

For 1 kHz pulse testing to highlight S-waves, the received signals from the water and the nano trials had nearly identical arrival times of shear waves (Figure 8.6), which is significantly slower than baseline and therefore satisfy the detection criterion. The nanoparticle dispersion was not considered detectible by S-wave amplitude, although one of the three repetitions was significantly lower than the baseline range.

For 30 kHz sweep testing to highlight spectral responses in the high coherence frequency range, the residual signal from the nanoparticle dispersion deviated significantly from the baseline in the ranges 8 - 10, 12 – 15, and 21- 25 kHz (Figures 8.7 and 8.8). The largest deviation in voltage from zero occurred in the same frequency range for both nano test and baseline, 12 -14 kHz.

Overall, results from multiple tests showed some deviations from baseline with ZnO at 0.03% concentration. To check if patterns develop, testing was repeated with nZnO concentration increased by a factor of 10.

8.4.2 0.3% Concentration

23 ml of the nZnO dispersion was diluted with 577 ml water to yield a 600 ml dispersion of nZnO. The following equation presents the dilution of the dispersed nZnO introduced into the column:

$$\left(\frac{4.6 \text{ ml nZnO}}{600 \text{ ml } H_2O + \text{nZnO}}\right) \times 100\% = 0.8\%$$

After draining the water used for saturating the specimen to test in clean water, the water retained in the column was approximately 277 ml. The volume of nZnO dispersion utilized for saturating the specimen for the nano trial was approximately 213 ml. The total concentration of nZnO in the column:

$$\left(\frac{0.8\% \ * \ 213 \text{ ml}}{213 \text{ ml} + 277 \text{ ml}}\right) = 0.3\%$$

Between trials, the volumetric moisture content of the glass bead specimen decreased by 7% and the saturated unit weight decreased by 0.4 kN/m^3.

For 8 kHz pulse testing to highlight P-waves, the received signals from the water and the nano trials had minimal divergence in phase, and had identical arrival times of slow compression waves and therefore did not satisfy the detection criteria (Figure 8.9). The nanoparticle dispersion was also not considered detectible by P-wave amplitude, although one of the three repetitions was significantly lower than the baseline range.

For 1 kHz pulse testing used to highlight S-waves, the received signals from the water and the nano trials had nearly identical arrival times for the shear waves (Figure 8.10), and therefore satisfy the detection criterion. The nanoparticle dispersion was also considered detectible by S-wave amplitude: amplitudes for all three repetitions satisfy the detection criterion.

For frequency response testing, the residual signal from the nanoparticle dispersion had only slight deviations from the baseline; no significant change was identified (Figures 8.11 and 8.12).

Detectability findings for nZnO at the mid-range concentration were consistent with the lower concentration only for P- and S-wave velocities. Next, testing was repeated with nZnO concentration increased again by approximately a factor of 10.

8.4.3 2.7% Concentration

150 ml of nZnO dispersion was diluted with 150 ml water to prepare a 300 ml dispersion. After draining the water used for saturating the specimen to test in clean water, approximately 246 ml of water remained in the column. The entire volume of 300 ml nZnO dispersion at 5.6% concentration was utilized for saturating the specimen for the nano trial, and an additional 75 ml of clean water was required to fill the pore spaces. The total concentration of nZnO in the column:

$$\left(\frac{5.6\ \% \ * \ 300\ \text{ml}}{300\ \text{ml} + 246\ \text{ml} + 75\ \text{ml}}\right) = 2.7\%$$

Between trials, the volumetric moisture content of the glass bead specimen did not change and the saturated unit weight increased by 0.06 kN/m^3.

For 8 kHz pulse testing to highlight P-waves, the received signals from the water and the nano trials had minimal divergence in phase, and had identical arrival times of slow compression waves (Figure 8.13), and therefore did not satisfy detection criteria. The nanoparticle dispersion was however considered detectible by P-wave amplitude, with amplitudes for all three repetitions above baseline range.

For 1 kHz pulse testing to highlight S-waves, the received signals from the water and the nano trials had nearly identical arrival times and satisfy the detection criterion (Figure 8.14). The nanoparticle dispersion was not however considered detectible by S-wave amplitude: none of the repetitions satisfy the detection criterion.

For frequency response testing, the residual signal from the nanoparticle dispersion deviated significantly from the baseline between approximately 7 to 12 kHz (Figures 8.15 and 8.16). The residual signal remained below the baseline until 18 kHz.

8.5 Summary: nZnO Testing

Considering the three concentrations tested with nZnO, the slow P-wave arrival times consistently lacked variation from the baseline results. Results for the slow P-wave amplitudes were inconsistent: amplitudes increased above baseline in the presence of nZnO at the low and high concentrations but not for the mid-range concentration. And the increase in amplitude for nZnO at high concentration was smaller than that from the nanoparticle dispersion at low concentration.

The S-wave arrival times increased by 5% with respect to the baseline results in the presence of nZnO at all concentrations, demonstrating a lack of dependence on concentration. The S-wave amplitudes showed a decrease in amplitude with respect to baseline for the mid-range concentration but no significant deviation from baseline for the low and high concentrations.

Spectral response analysis of the residual signal from nZnO at the mid-range concentration showed less variation from the baseline when compared with the

nanoparticle dispersion at low and high concentrations. The perturbations observed with the nanoparticle dispersion at high concentration were larger in magnitude when compared to the deviations observed at low concentration.

In the interest of efficiency, the rest of the nanoparticle dispersion tests were conducted only in the high concentration range.

8.6 Testing with $nTiO_2$ at 4.9% Concentration

70 ml of the $nTiO_2$ dispersion at 40% concentration was diluted with 330 ml water and placed on a stirrer for approximately 30 minutes to aid dispersion; a 400 ml dispersion was prepared. After draining the water used for saturating the specimen to test in clean water, the water retained in the column was approximately 156 ml. The volume of $nTiO_2$ utilized for the nano trial was approximately 370 ml. The total concentration of $nTiO_2$ in the column:

$$\left(\frac{7\% \ * \ 370 \text{ ml}}{370 \text{ ml} + 156 \text{ ml}}\right) = 4.9\%$$

Between trials the volumetric moisture content of the glass bead specimen decreased by 1% and the saturated unit weight increased by 0.05 kN/m^3.

For 8 kHz pulse testing to highlight P-waves, the received signals from the water and the nano trials had minimal divergence in phase, and had identical arrival times of slow compression waves, and therefore did not satisfy detection criteria (Figure 8.17). The nanoparticle dispersion was also not considered detectible by P-wave amplitude; although one of the three repetitions was significantly lower than the baseline range.

For 1 kHz pulse testing to highlight S-waves, the water trial results failed to satisfy the baseline acceptance criteria. The arrival times of the received signals from the nano trials (Figure 8.18) did not satisfy the detection criterion. The nanoparticle dispersion was also not considered detectible by S-wave amplitude: two of the three repetitions did not satisfy the detection criterion.

For frequency response testing, the only significant deviation of the residual signal of the nanoparticle dispersion from the baseline is around the resonance frequency (8 kHz) (Figures 8.19 and 8.20).

Overall, the results indicate that $nTiO_2$ at the concentration tested is not detectible with seismic methods, except possibly by spectral response.

8.7 Testing with nAg at 3.7% Concentration

The nAg was at 99% purity and in powdered form. The dispersion volume required was 400 ml. The concentration of nAg after dispersing 25.0 g in 400 ml water:

$$\frac{25000 \text{ mg nAg}}{(400 \text{ ml } H_2O)} = 62.5 \frac{\text{mg}}{\text{ml}} = 6.3\%$$

The 25 grams of nAg was placed in a flask, and 400 ml of distilled water was added to it. The flask was then placed in a sonicator for approximately 300 minutes; this duration was chosen experimentally to ensure thorough dispersion.

After draining the water used for saturating the specimen to test in clean water, the water retained in the column was approximately 246 ml. The volume of nAg dispersion required for filling the pore spaces of the specimen was approximately 347 ml. The total concentration of nAg in the column:

$$\left(\frac{6.3\ \%\ *\ 347\ \text{ml}}{347\ \text{ml}\ +\ 246\ \text{ml}}\right) = 3.7\%$$

Between trials the volumetric moisture content of the glass bead specimen did not change and the saturated unit weight decreased by 0.06 kN/m^3.

For 8 kHz pulse testing to highlight P-waves, the received signals from the water and the nano trials had minimal divergence in phase, and had identical arrival times of slow compression waves (Figure 8.21), and therefore did not satisfy the detection criteria. The nanoparticle dispersion was however considered detectible by P-wave amplitude, with amplitudes for all three repetitions above baseline range.

For 1 kHz pulse testing to highlight S-waves, the arrival times of the received signals from the nano trials (Figure 8.22) did not satisfy the detection criterion. The nanoparticle dispersion was not considered detectible by S-wave amplitude: all three repetitions did not satisfy the detection criterion.

For frequency response testing, the residual signal from the nanoparticle dispersion deviated significantly from the baseline at the resonance frequency (8 kHz) and between 12 – 13 kHz (Figures 8.23 and 8.24).

In summary, the presence of nAg at 3.7% concentration was detectable only by P-wave amplitude and possibly spectral response.

8.8 Overall Analysis: Nanoparticle Detectability by Seismic Methods

Three nanoparticle dispersions were tested: nZnO, nTiO_2, and nAg. Only nZnO dispersions were tested at multiple concentrations levels which are referred to here as low (0.01 to 0.05%), medium (0.1 to 0.5%) and high (1 to 5%). The nAg and nTiO_2

dispersions were tested only at high concentration. A summary of the time domain tests carried out, and the outcomes stating which nanoparticle dispersions are detectible, and by what method, are presented in Table 8.3.

An overall comparison of the 8 kHz sine pulse received signals for all the nanoparticle dispersions tested and one of the three baseline specimens tested is presented in Figure 8.25. This testing addressed slow P-wave arrival times and zero-to-peak amplitude differences. The arrival times showed no change from baseline for any nanoparticle dispersion. The amplitudes, however, showed differences from baseline. The nZnO was considered detectable at low and high concentration, but not at medium concentration. The nAg was considered detectable, but the $nTiO_2$ was not.

An overall comparison of the 1 kHz sine pulse received signals for all the nanoparticle dispersions tested and one of the three baseline specimens tested is presented in Figure 8.26. This testing addressed S-wave arrival times and peak-to-peak amplitude differences. The presence of nZnO at all concentration levels was detectable by S-wave arrival times, which were outside the bounds (trailing) established for the baseline by approximately 5%. The presence of nAg was not detectable by S-wave arrival time, and the same was true for $nTiO_2$, however, these results are uncertain due to the water trial of that specimen not satisfying the baseline acceptance criteria. The presence of nZnO was detectable by S-wave amplitudes at medium concentration, but not at low or high concentrations. This conflicting outcome is not understood and merits further study. The presence of $nTiO_2$ was not detectable by S-wave amplitude and neither was nAg.

An overall comparison of the residual spectral responses in the presence of all the nanoparticle dispersions tested and one of the three baseline specimens tested is presented

in Figure 8.27. Testing for spectral response with a 30 kHz sweep addressed Fourier amplitudes. The baseline was established by computing the residual (difference between consecutive tests on the same specimen, separated only by draining and refilling the pore fluid) upon water-saturated specimens (Fig. 7.16). In the presence of nZnO, spectral responses fluctuated with respect to concentration levels, with the largest deviation from baseline at high concentration and the smallest at mid-range. In the presence of $nTiO_2$, the spectral response was not distinguishable from baseline, except at around 8 kHz, which is resonance. In the presence of nAg, some local amplitude spikes surpassed baseline. Further tests for spectral response are needed to obtain quantifiable criteria, from which detectability can be established.

Table 8.1. Velocities associated with received pulse signals from water and nanoparticle dispersions in glass bead specimens

Specimen	Repetition	Compression (slow P-wave): 8 kHz pulse			Shear (S-wave): 1 kHz pulse		
		Water Trial (m/s)	Nano Trial (m/s)	Difference	Water Trial (m/s)	Nano Trial (m/s)	Difference
nZnO (0.03%)	1	561.7	561.7	0.0%	27.1	27.2	**0.4%**
	2				27.3	27.3	**0.0%**
	3				27.2	27.3	**0.4%**
nZnO (0.3%)	1	562.4	562.4	0.0%	26.4	26.3	**0.4%**
	2				26.7	26.7	**0.0%**
	3				26.9	26.7	**0.9%**
nZnO (2.7%)	1	561	561	0.0%	31.0	31.0	**0.0%**
	2				31.0	31.1	**0.5%**
	3				30.8	31.0	**0.5%**
$nTiO_2$ (4.9%)	1	560.6	560.6	0.0%	**22.0**	24.2	10.0%
	2				**22.0**	24.2	9.7%
	3				**22.0**	24.3	10.1%
nAg (3.7%)	1	561	561	0.0%	26.3	28.4	8.2%
	2				26.5	28.6	7.8%
	3				26.2	28.6	9.1%

Red bold text indicates water trial outside range from baseline trial 1,
Black bold text in yellow box indicates detectable nano trial where the response was lower than baseline range.

Table 8.2. Amplitudes associated with received pulse signals from tests in water and nanoparticle dispersions in glass bead specimens

Specimen	Repetition	Compression (slow P-wave): 8 kHz pulse			Shear (S-wave): 1 kHz pulse		
		Water Trial (P1, V)	Nano Trial (P2, V)	Difference	Water Trial (ΔP1, V)	Nano Trial (ΔP2, V)	Difference
nZnO (0.03%)	1	0.35	**0.68**	95%	**0.33**	**0.77**	133%
	2	0.28	**0.41**	47%	1.94	2.04	5%
	3	0.28	**0.42**	49%	2.00	2.11	5%
nZnO (0.3%)	1	**0.00**	**0.00**	-75%	**0.75**	**0.73**	-3%
	2	0.23	0.23	-1%	1.77	**1.73**	-2%
	3	0.38	0.25	-33%	1.85	**1.56**	-16%
nZnO (2.7%)	1	0.24	**0.32**	35%	1.82	2.21	21%
	2	0.34	**0.35**	3%	2.20	2.25	2%
	3	0.34	**0.35**	3%	2.17	2.25	4%
nTiO (4.9%)	1	**0.14**	**0.16**	16%	1.87	**1.72**	-8%
	2	0.18	0.22	23%	2.27	2.07	-9%
	3	0.19	0.23	22%	2.24	2.07	-8%
nAg (3.7%)	1	0.27	**0.32**	18%	1.62	2.13	31%
	2	0.41	**0.42**	3%	2.52	2.21	-12%
	3	0.41	**0.42**	4%	**2.55**	2.22	-13%

Red bold text indicates water trial outside range from baseline trial 1,
Black bold text in green box indicates detectable nano trial where the response was higher than baseline range,
Black bold text in yellow box indicates detectable nano trial where the response was lower than baseline range.

Table 8.3. Summary of detectability of nanoparticle dispersions in glass bead specimens using time domain methods

Specimen	P-wave Velocity	P-wave Amplitude	S-wave Velocity	S-wave Amplitude
nZnO (0.03%)	No	**Yes**	**Yes**	No
nZnO (0.3%)	No	No	**Yes**	**Yes**
nZnO (2.7%)	No	**Yes**	**Yes**	No
$nTiO_2$ (4.9%)	No	No	**N/A**	No
nAg (3.7%)	No	**Yes**	No	No

Green box indicates detectible nanoparticle dispersions
Orange box indicates unusable nanoparticle dispersion

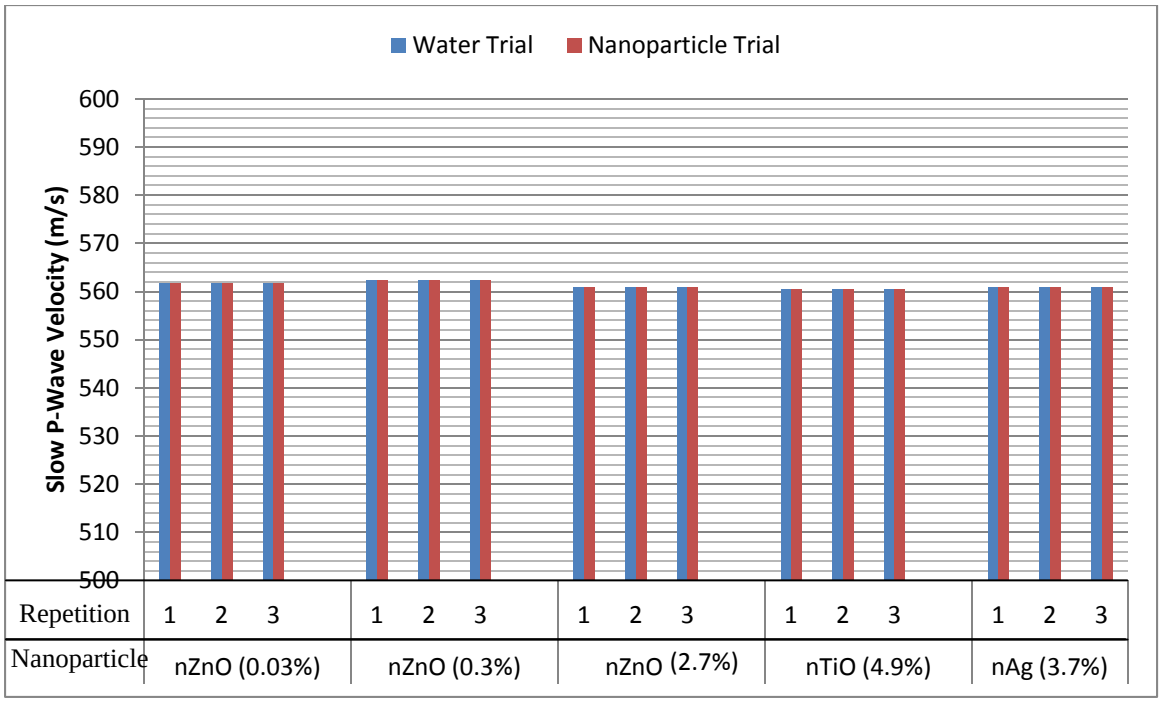

Figure 8.1. Summary of 8 kHz results highlighting slow P-wave velocity for all nanoparticle dispersions.

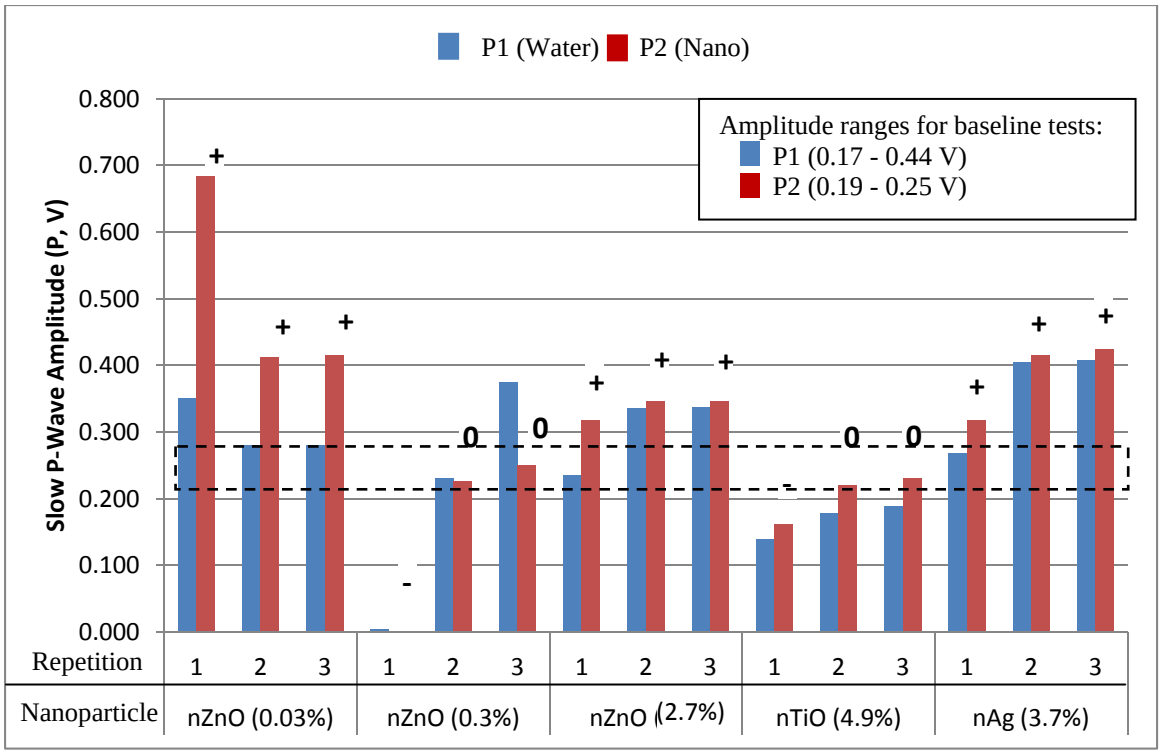

Figure 8.2. Summary of P-wave characteristic point amplitudes from 8 kHz pulse tests in water and in the presence of nanoparticle dispersions in saturated glass bead specimens. The signs indicate an increase (+), decrease (-) or no change (0) in amplitude for the P-waves in the presence of nanoparticles from the baseline trial 2 result. The black dashed lines show the baseline against which to compare nano test amplitudes (from Sec. 7.4).

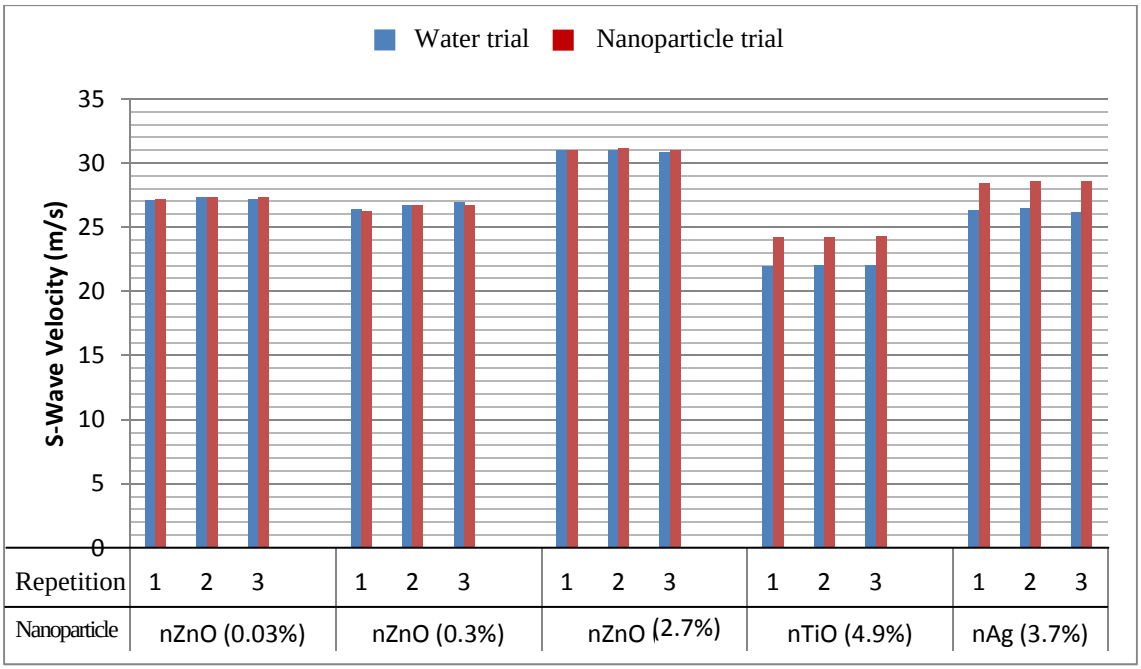

Figure 8.3. Summary of 1 kHz results highlighting S-wave velocity for all nanoparticle dispersions.

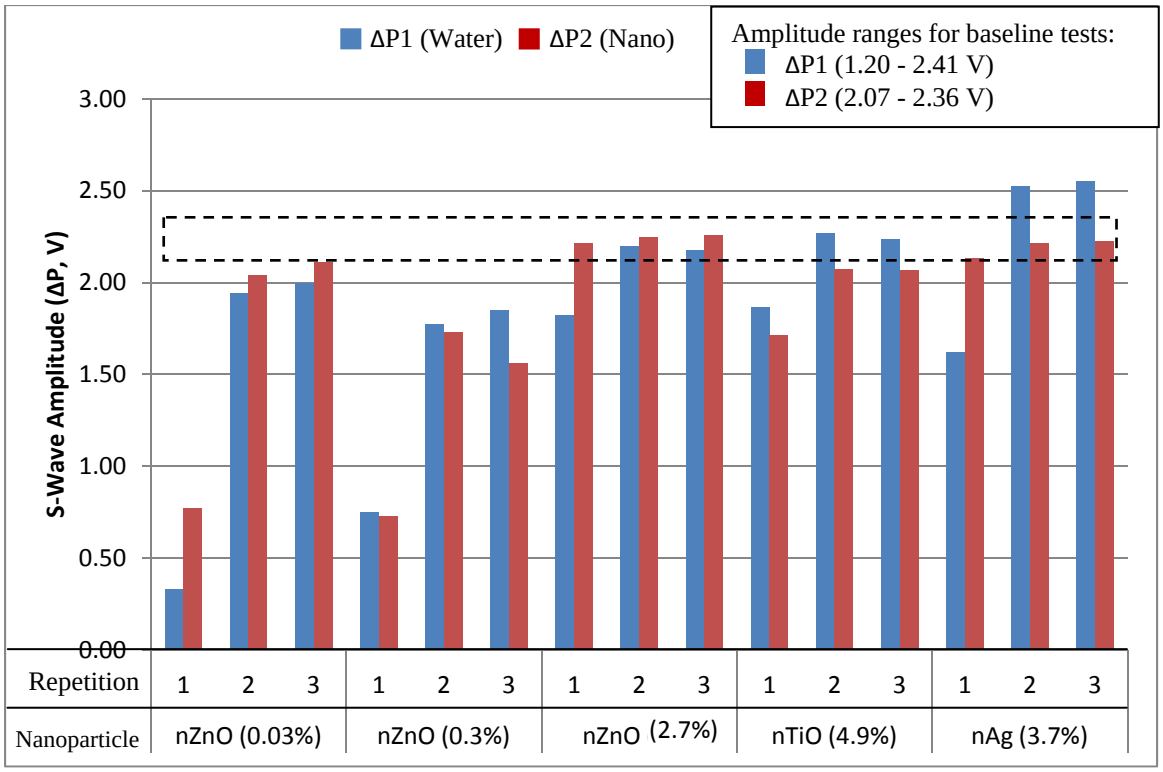

Figure 8.4. Summary of S-wave amplitudes from 1 kHz pulse tests in water and in the presence of nanoparticle dispersions in saturated glass bead specimens. The black dashed lines show the ΔP2 baseline amplitude range (from Sec. 7.5).

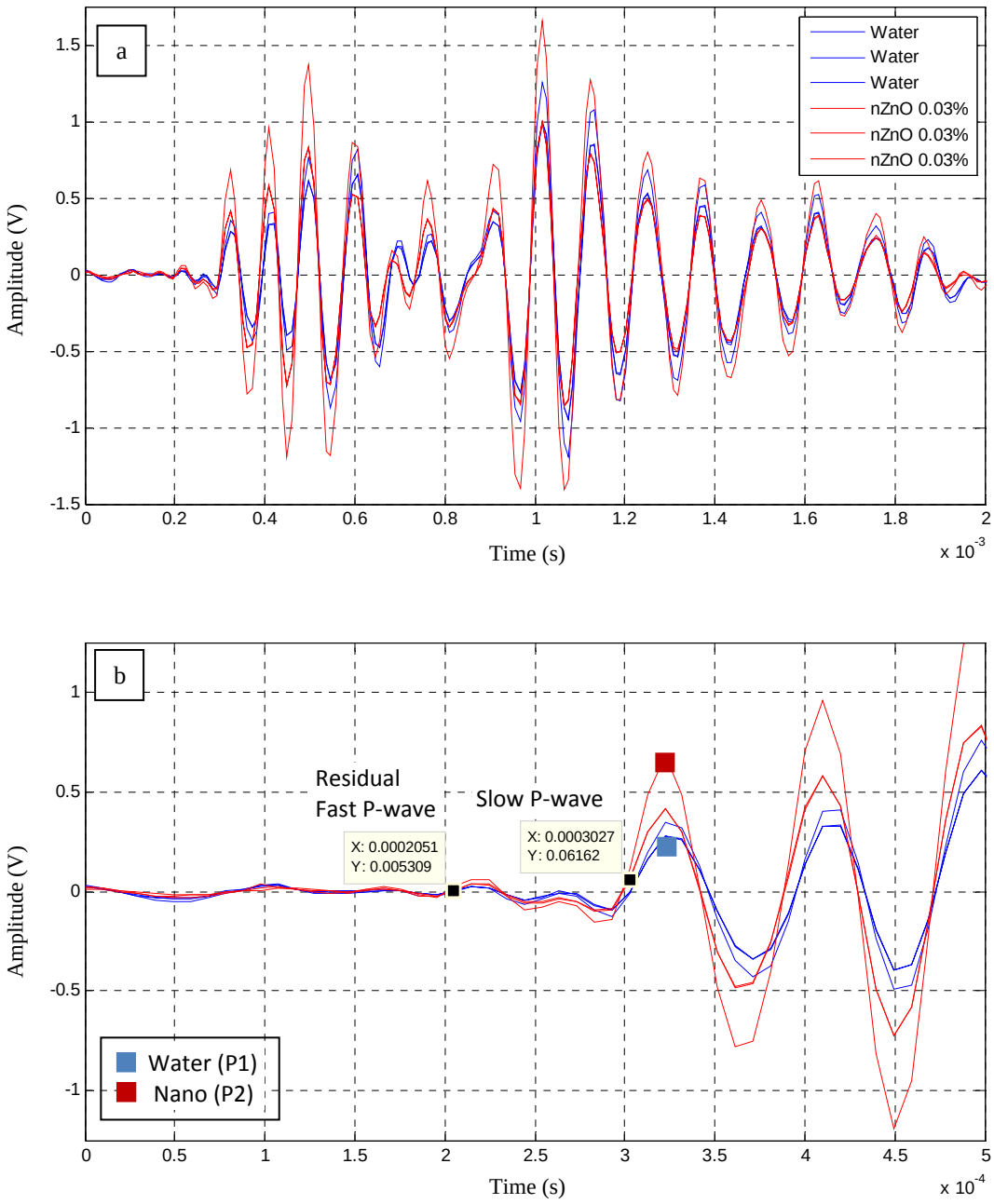

Figure 8.5. 8 kHz sine pulse with 200 Hz high-pass filter applied in saturated glass bead specimen for testing differences in compression with water and nZnO at 0.03% dispersion, showing three repetitions of 1000 recordings averaged per repetition.

a: Expanded view of entire received signal; note amplitude variation between the three repetitions of each trial
b: Detail view showing representative picks for characteristic amplitude points, residual fast P-wave and slow P-wave arrivals

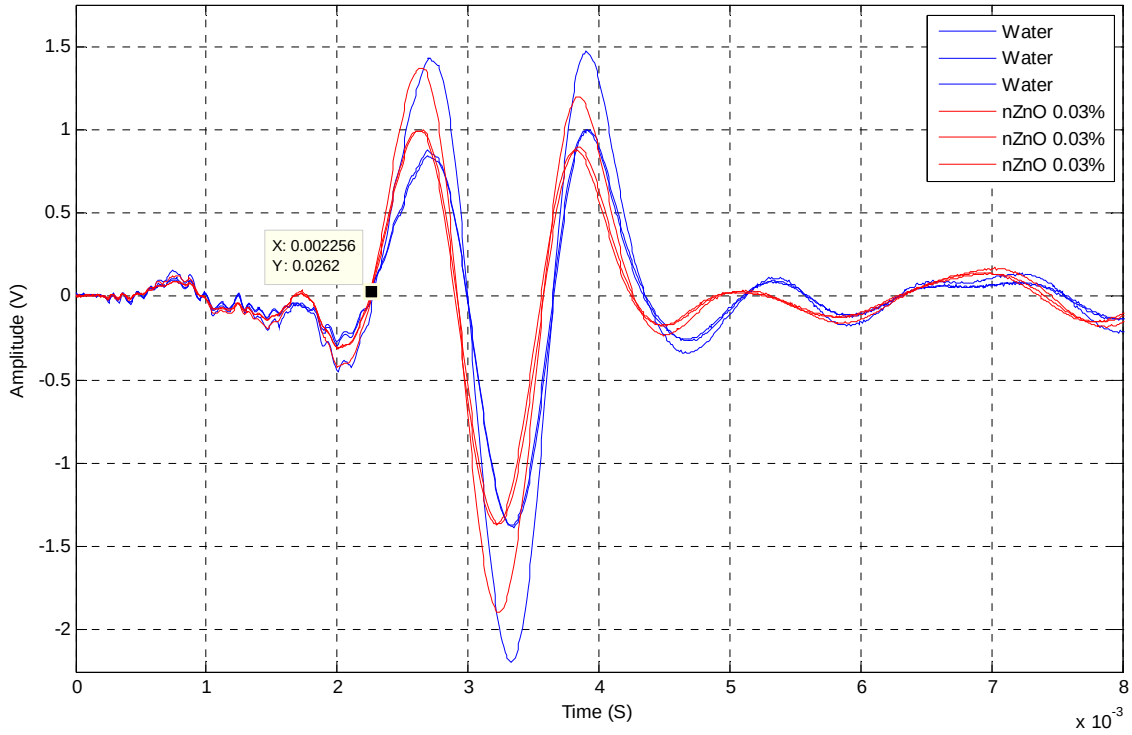

Figure 8.6. 1 kHz sine pulse with 200 Hz high-pass filter in saturated glass bead specimen for testing shear in the presence of water and nZnO at 0.03% dispersion, showing three repetitions of 1000 recordings averaged per repetition, and consistent first arrival pick.

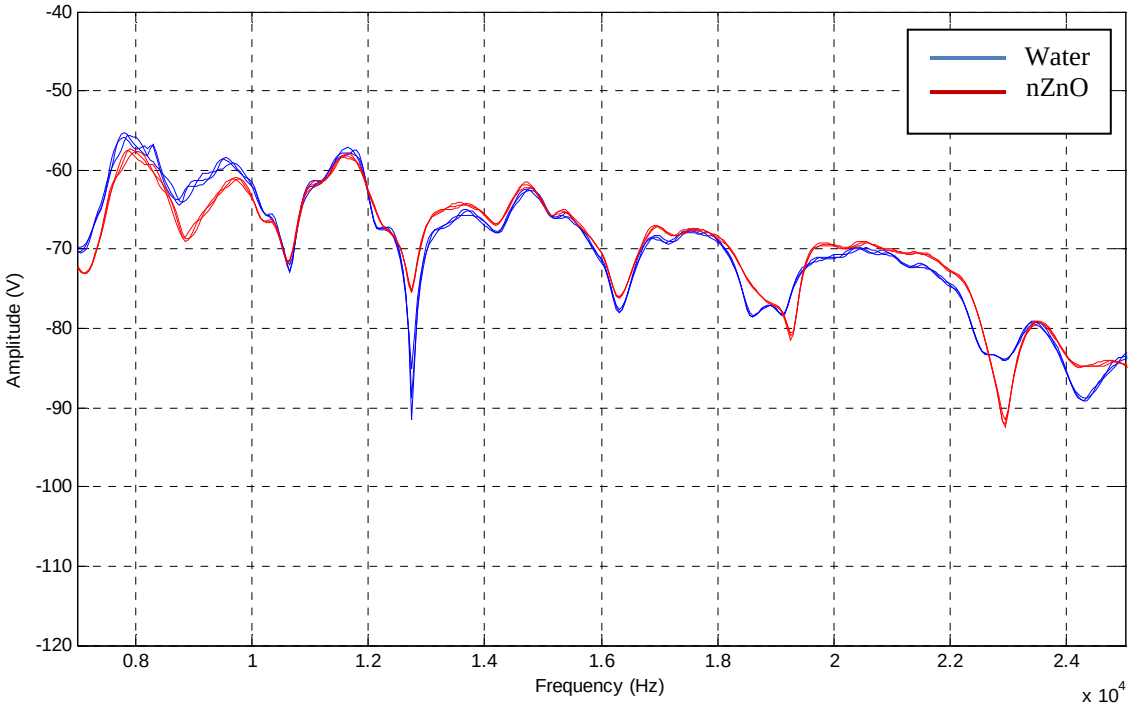

Figure 8.7. 30 kHz sweep with 200 Hz high-pass filter, testing spectral response in a saturated glass bead specimen in water and in the presence of nZnO at 0.03% dispersion, showing three repetitions of 1000 recordings averaged per repetition.

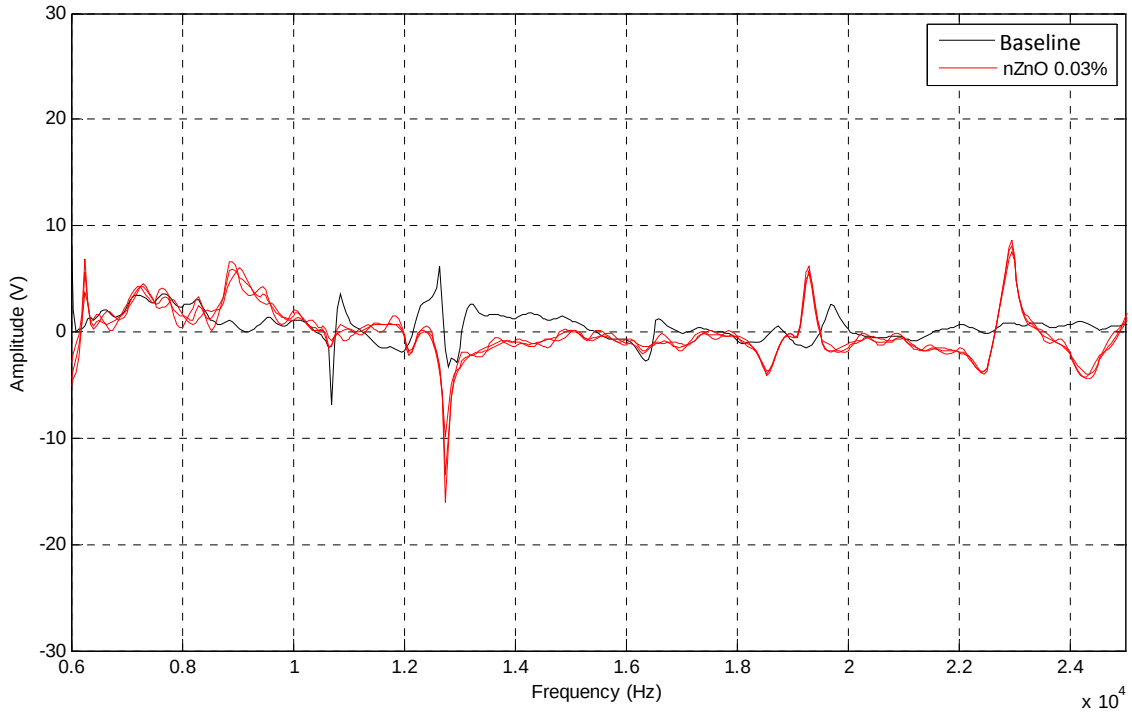

Figure 8.8. Residual signals from the differences of spectral response in water and in nZnO at 0.03%, of three repetitions of 1000 recordings averaged per repetition, compared to the average baseline residual signal.

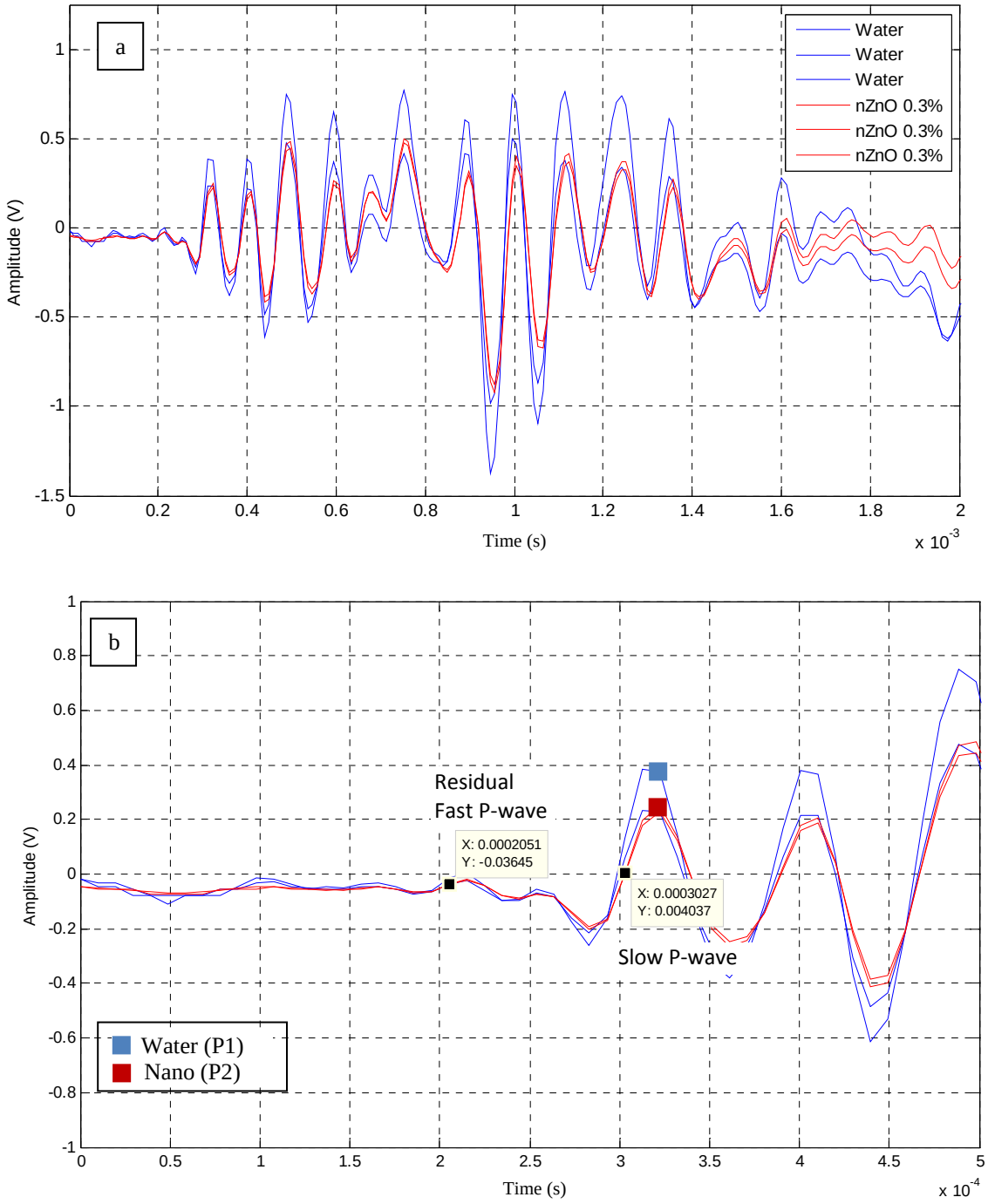

Figure 8.9. 8 kHz sine pulse with 200 Hz high-pass filter in saturated glass bead specimen for testing differences in compression with water and nZnO at 0.3% dispersion, showing three repetitions of 1000 recordings averaged per repetition.
a: Expanded view of entire received signal; note amplitude variation between the three repetitions of each trial
b: Detail view showing representative picks for characteristic amplitude points, residual fast P-waves and slow P-wave arrivals

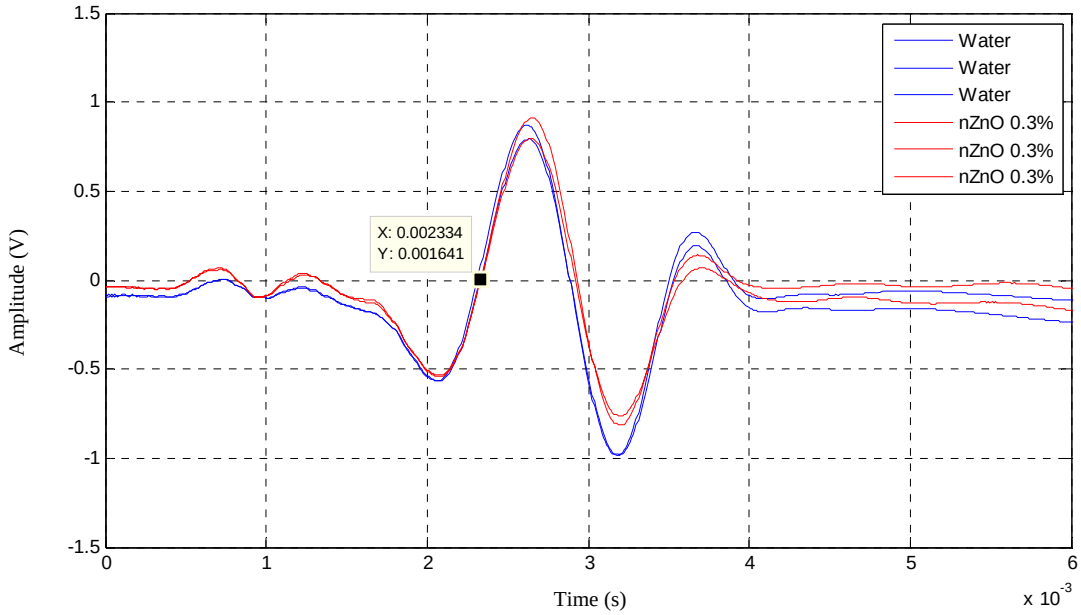

Figure 8.10. 1 kHz sine pulse with 200 Hz high-pass filter in saturated glass bead specimen for testing shear in the presence of water and nZnO at 0.3% dispersion, showing three repetitions of 1000 recordings averaged per repetition, and consistent first arrival pick.

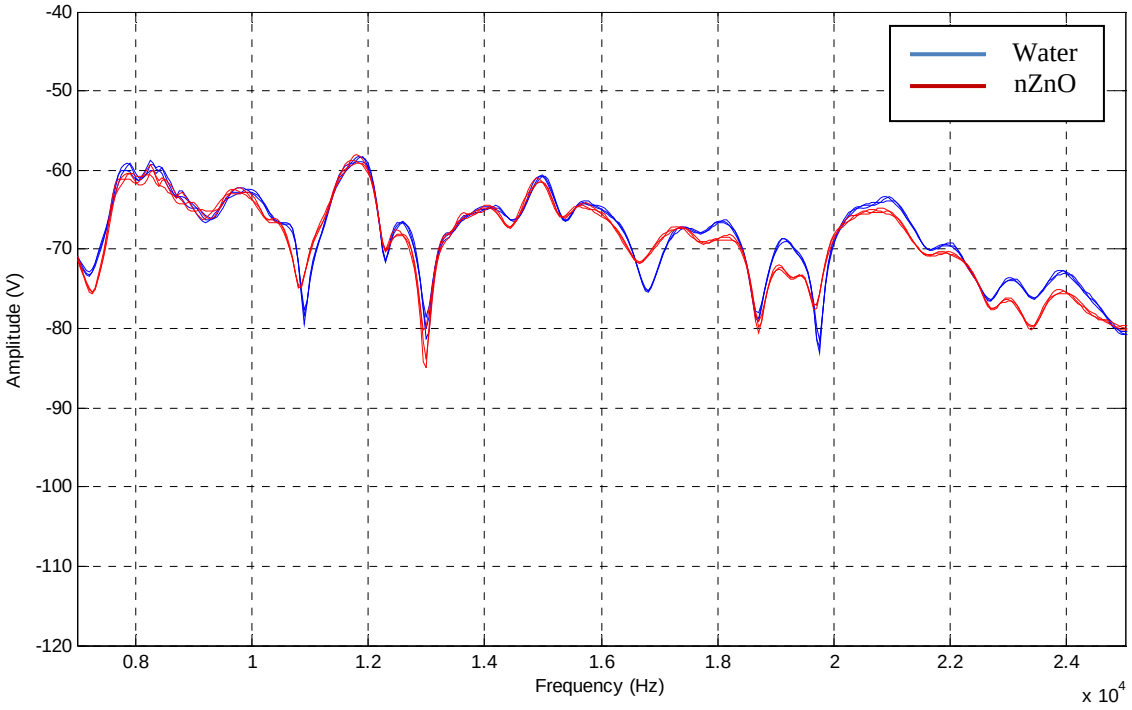

Figure 8.11. 30 kHz sweep with 200 Hz high-pass filter, testing spectral response in a saturated glass bead specimen in water and in the presence of nZnO at 0.3% dispersion, showing three repetitions of 1000 recordings averaged per repetition.

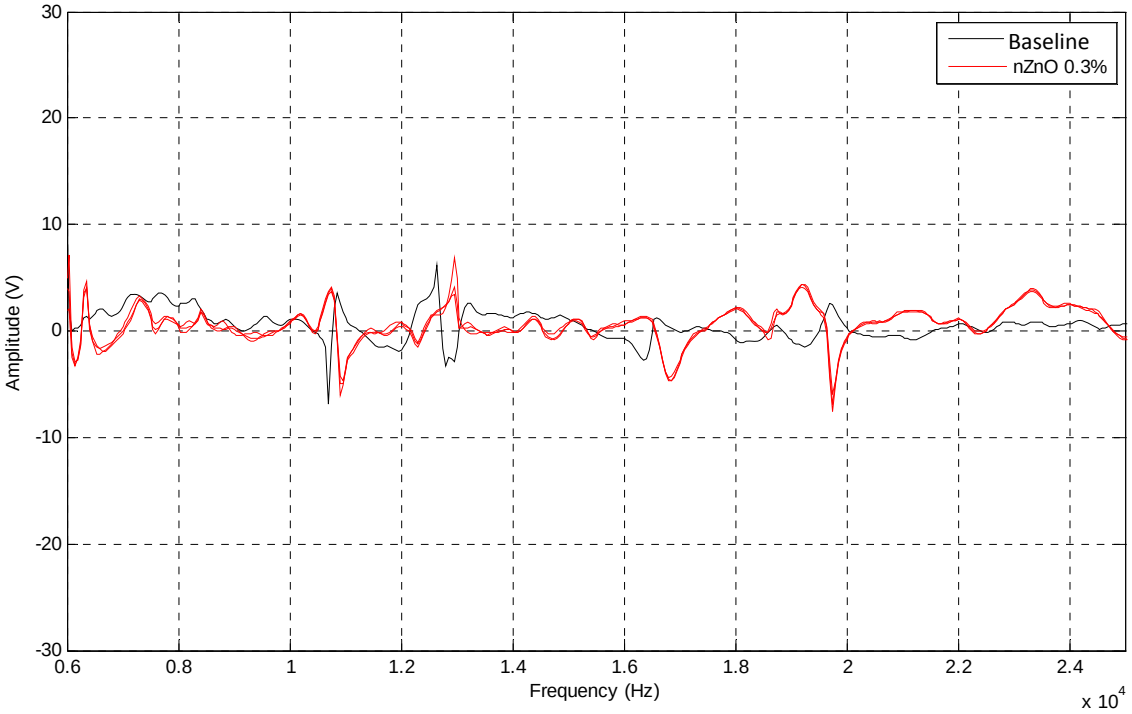

Figure 8.12. Residual signals from the differences of spectral response in water and in nZnO at 0.3%, of three repetitions of 1000 recordings averaged per repetition, compared to the average baseline residual signal.

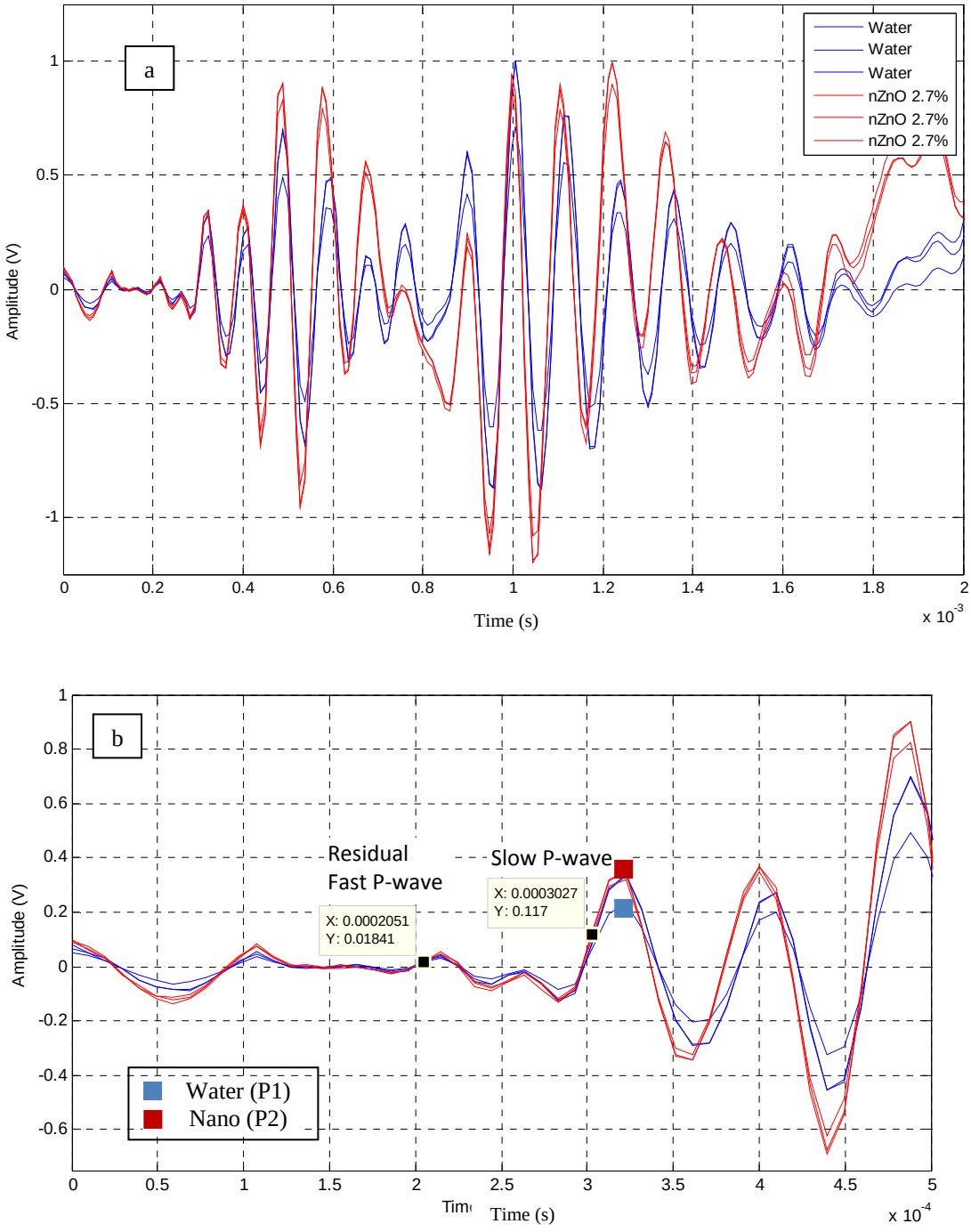

Figure 8.13. 8 kHz sine pulse with 200 Hz high-pass filter applied in saturated glass bead specimen for testing differences in compression with water and nZnO at 2.7% dispersion, showing three repetitions of 1000 recordings averaged per repetition.
a: Expanded view of entire received signal; note amplitude variation between the three repetitions of each trial
b: Detail view showing representative picks for characteristic amplitude points, residual fast P-wave and slow P-wave arrivals

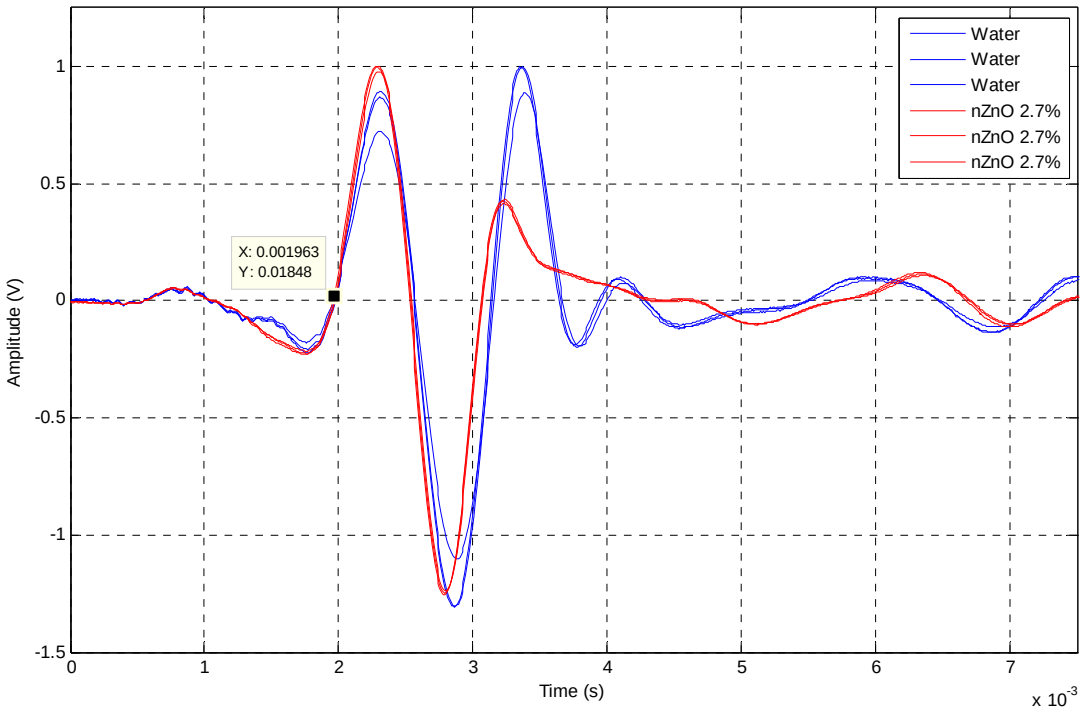

Figure 8.14. 1 kHz sine pulse with 200 Hz high-pass filter in saturated glass bead specimen for testing shear in the presence of water and nZnO at 2.7% dispersion, showing three repetitions of 1000 recordings averaged per repetition, and consistent first arrival pick.

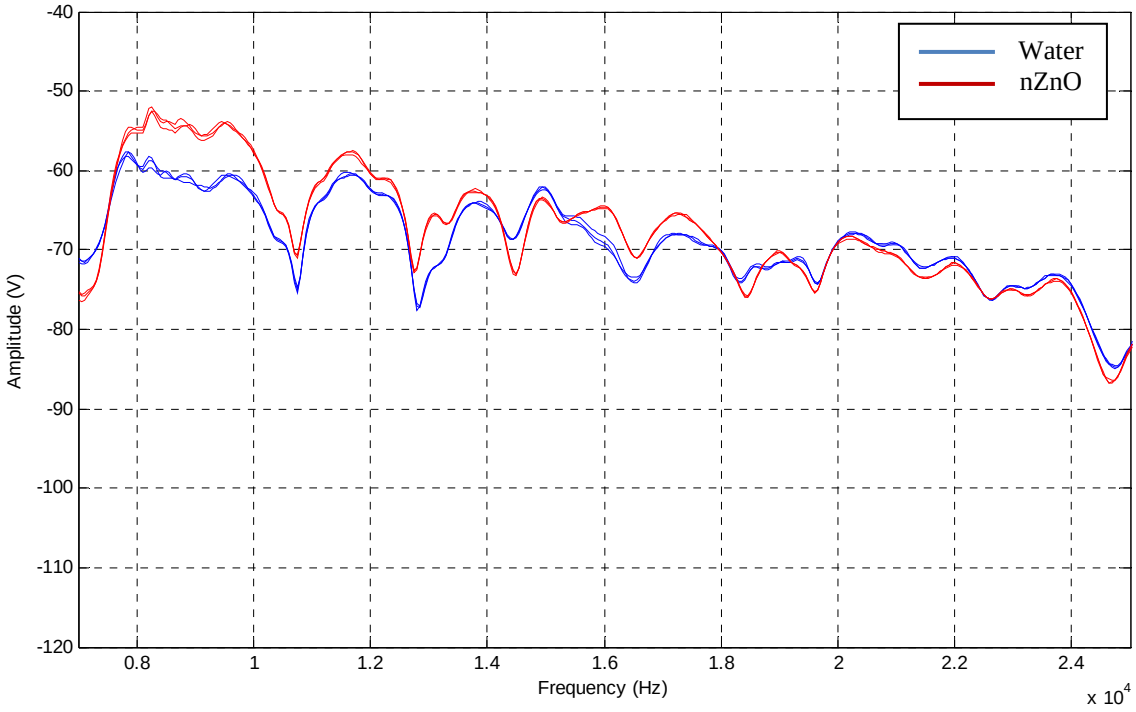

Figure 8.15. 30 kHz sweep with 200 Hz high-pass filter, testing spectral response in a saturated glass bead specimen in water and in the presence of nZnO at 2.7% dispersion, showing three repetitions of 1000 recordings averaged per repetition.

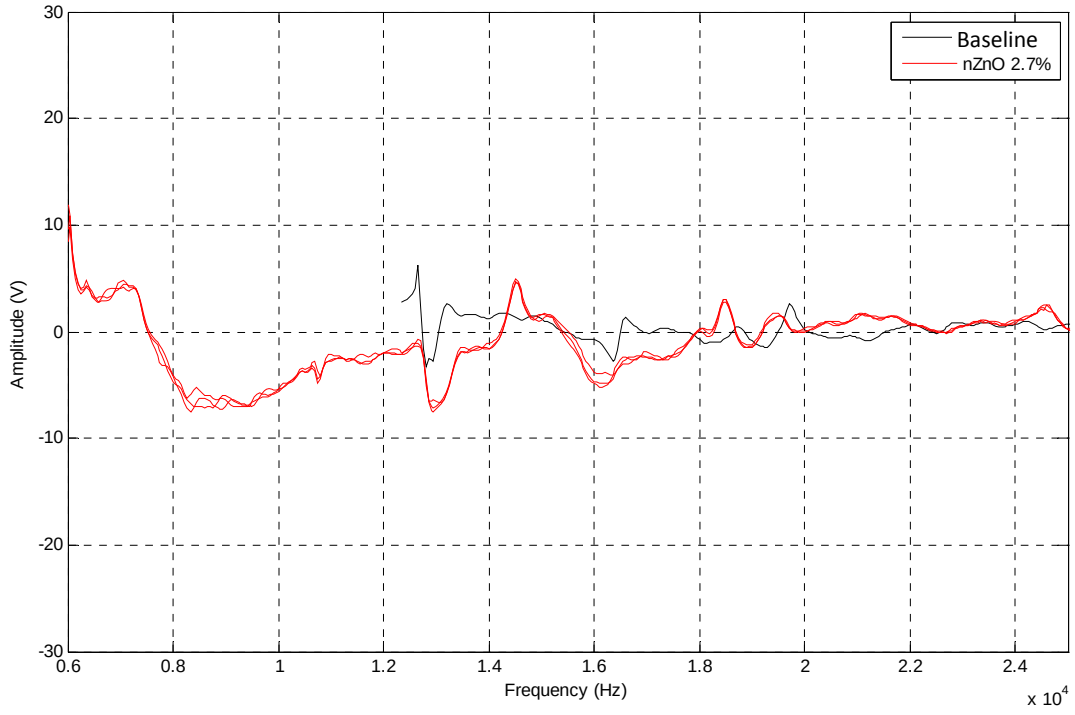

Figure 8.16. Residual signals from the differences of spectral response in water and in nZnO at 2.7%, of three repetitions of 1000 recordings averaged per repetition, compared to the average baseline residual signal.

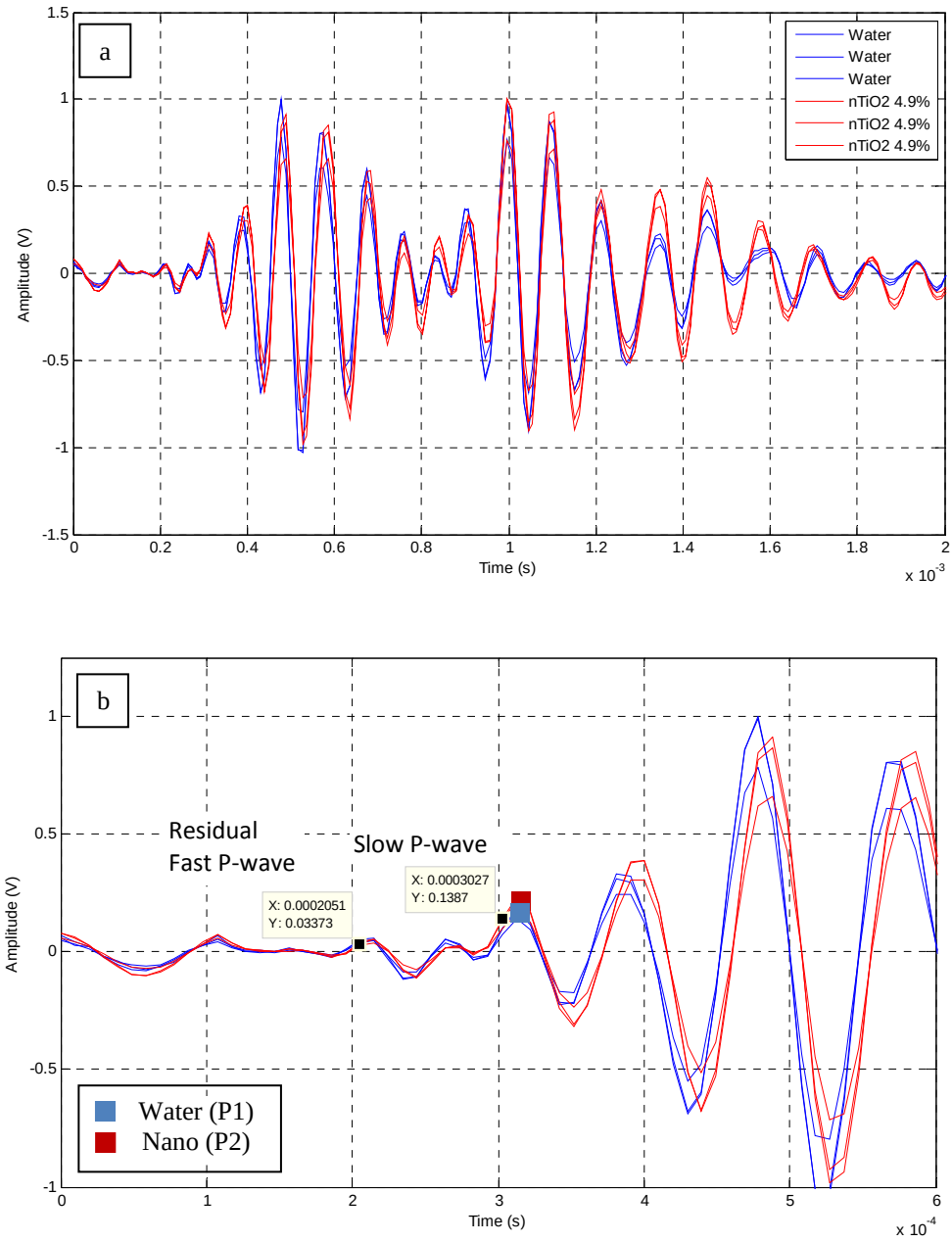

Figure 8.17. 8 kHz sine pulse with 200 Hz high-pass filter applied in saturated glass bead specimen for testing differences in compression with water and $nTiO_2$ at 4.9% dispersion, showing three repetitions of 1000 recordings averaged per repetition.

a: Expanded view of entire received signal; note amplitude variation between the three repetitions of each trial
b: Detail view showing representative picks for characteristic amplitude points, residual fast P-wave, and slow P-wave arrivals

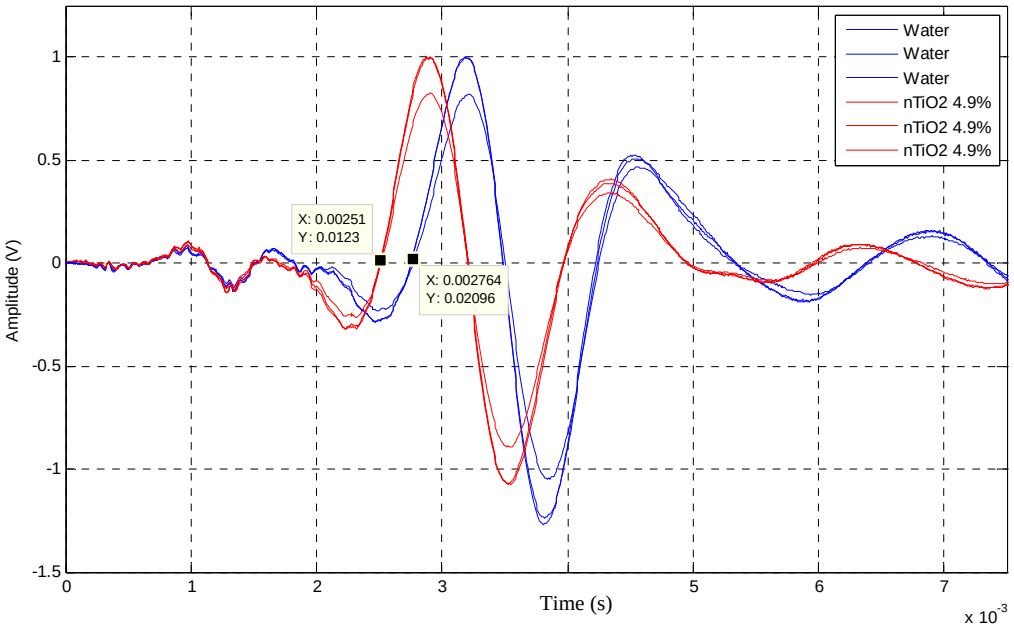

Figure 8.18. 1 kHz sine pulse with 200 Hz high-pass filter in saturated glass bead specimen for testing shear in the presence of water and $nTiO_2$ at 4.9% dispersion, showing three repetitions of 1000 recordings averaged per repetition, and first arrival pick for $nTiO_2$ coming in earlier than water.

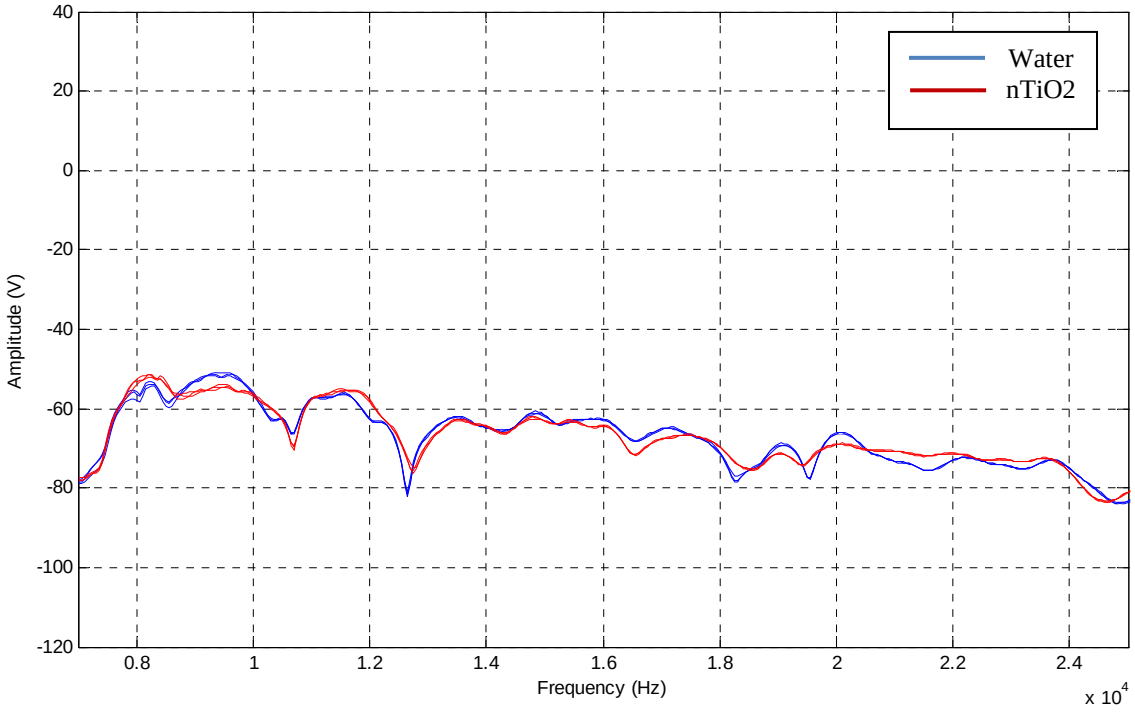

Figure 8.19. 30 kHz sweep with 200 Hz high-pass filter, testing spectral response in a saturated glass bead specimen in water and in the presence of $nTiO_2$ at 4.9% dispersion, showing three repetitions of 1000 recordings averaged per repetition.

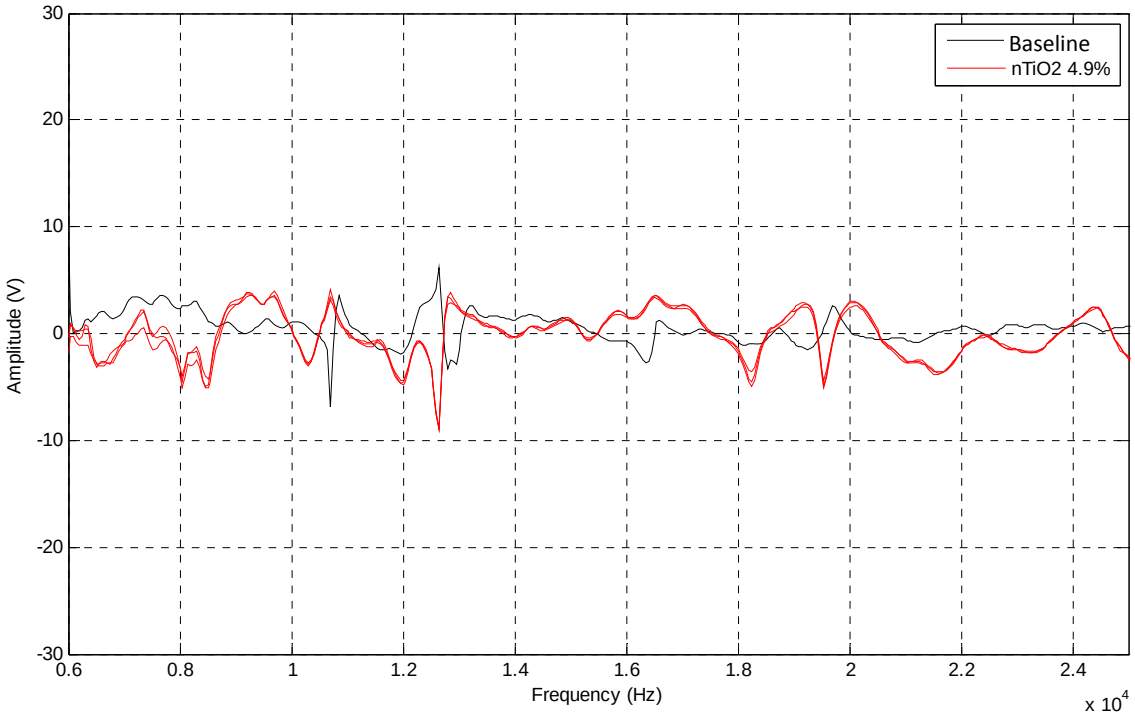

Figure 8.20. Residual signals from the differences of spectral response in water and in $nTiO_2$ at 4.9%, of three repetitions of 1000 recordings averaged per repetition, compared to the average baseline residual signal.

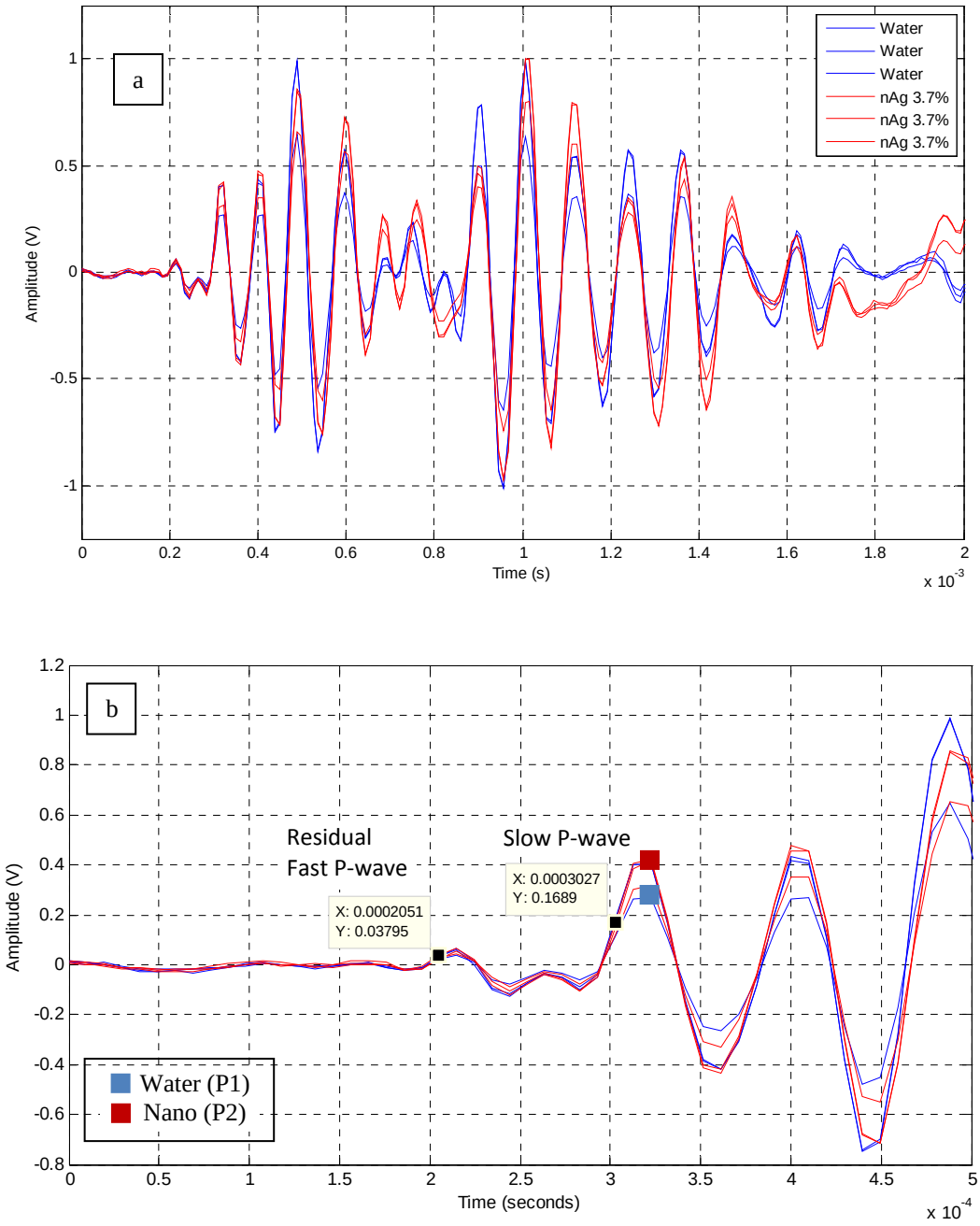

Figure 8.21. 8 kHz sine pulse with 200 Hz high-pass filter applied in saturated glass bead specimen for testing differences in compression with water and nAg at 3.7% dispersion, showing three repetitions of 1000 recordings averaged per repetition.

a: Expanded view of entire received signal; note amplitude variation between the three repetitions of each trial
b: Detail view showing representative picks characteristic amplitude points, residual fast P-wave, and slow P-wave arrivals

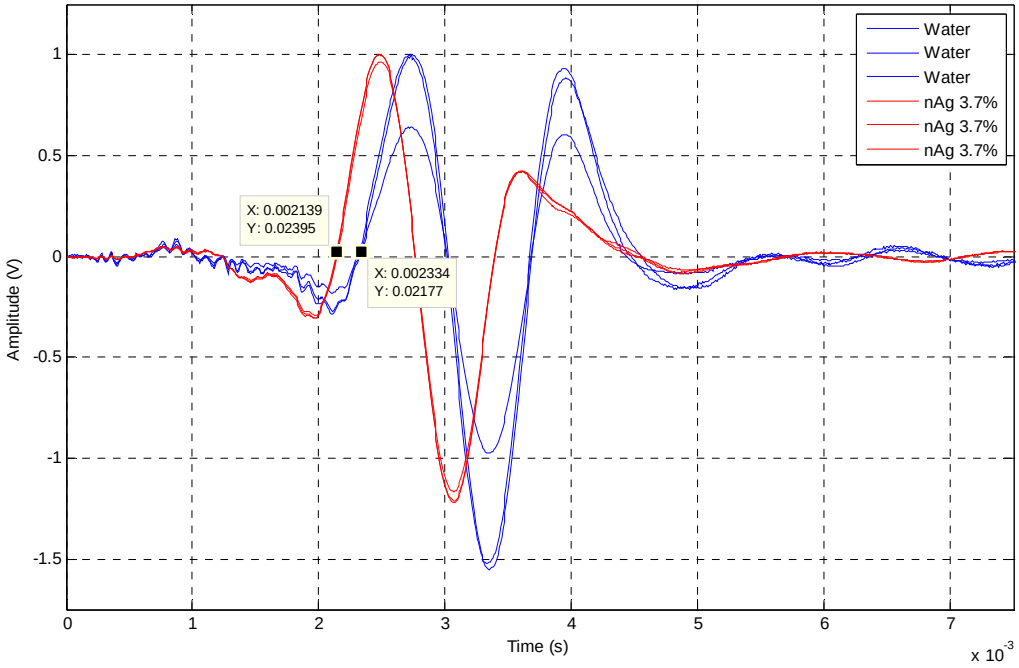

Figure 8.22. 1 kHz sine pulse with 200 Hz high-pass filter in saturated glass bead specimen for testing shear in the presence of water and nAg at 3.7% dispersion, showing three repetitions of 1000 recordings averaged per repetition, and first arrival pick for nAg coming in earlier than for water.

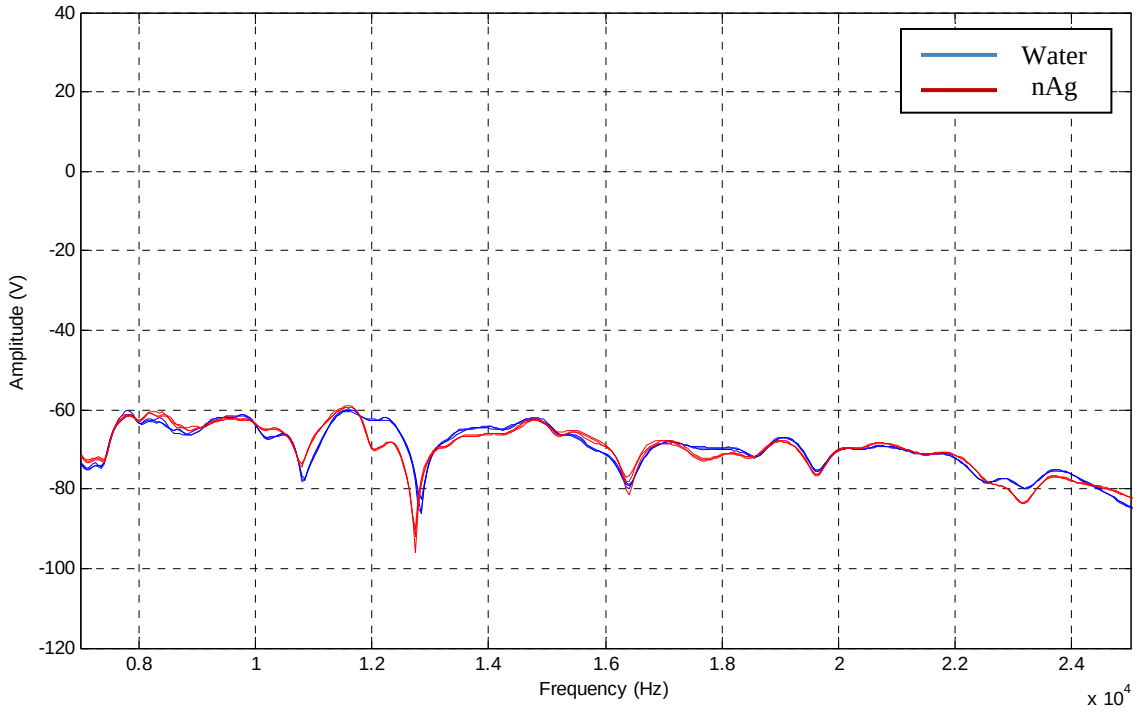

Figure 8.23. 30 kHz sweep with 200 Hz high-pass filter, testing spectral response in a saturated glass bead specimen in water and in the presence of nAg at 3.7% dispersion, showing three repetitions of 1000 recordings averaged per repetition.

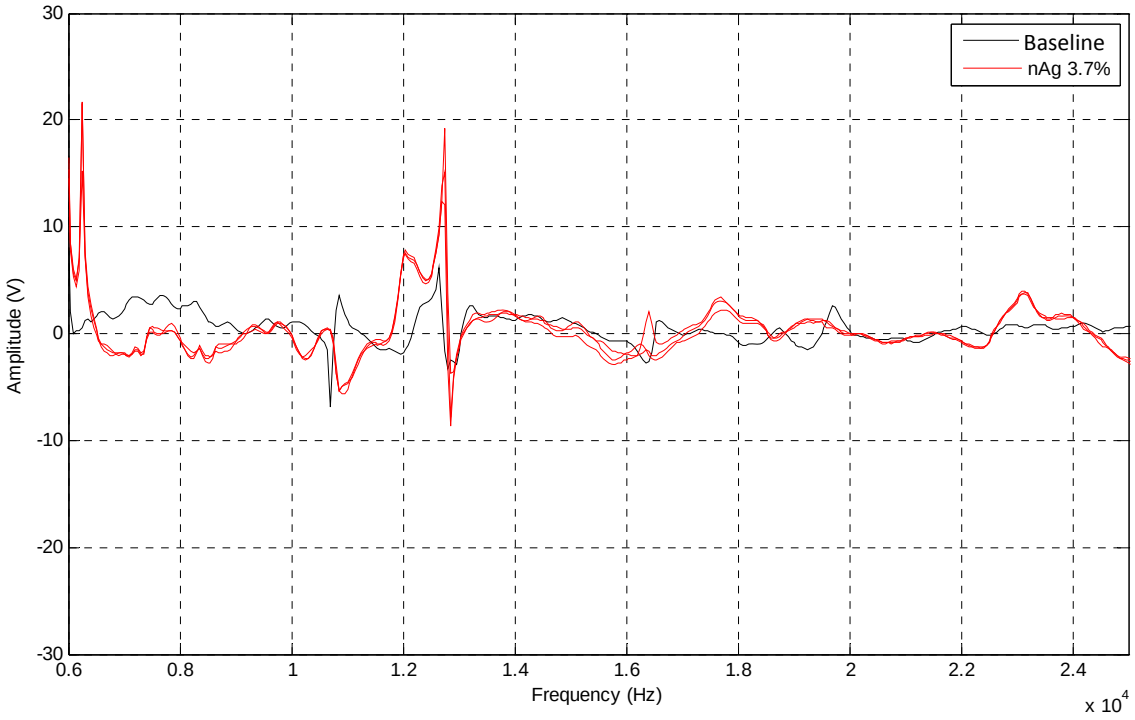

Figure 8.24. Residual signals from the differences of spectral response in water and in nAg at 3.7%, of three repetitions of 1000 recordings averaged per repetition, compared to the average baseline residual signal.

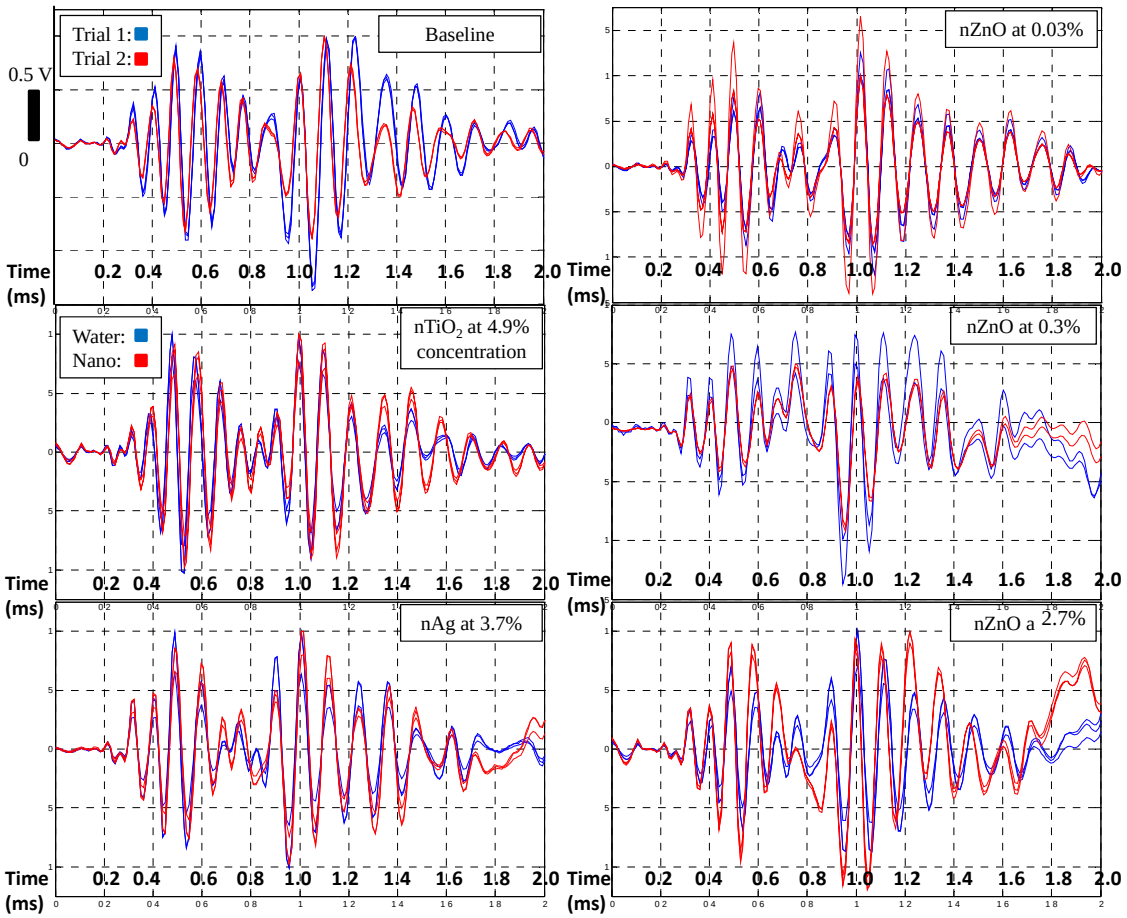

Figure 8.25. Signals from slow compression wave comparing response in the presence of nanoparticles to the baseline received signal.

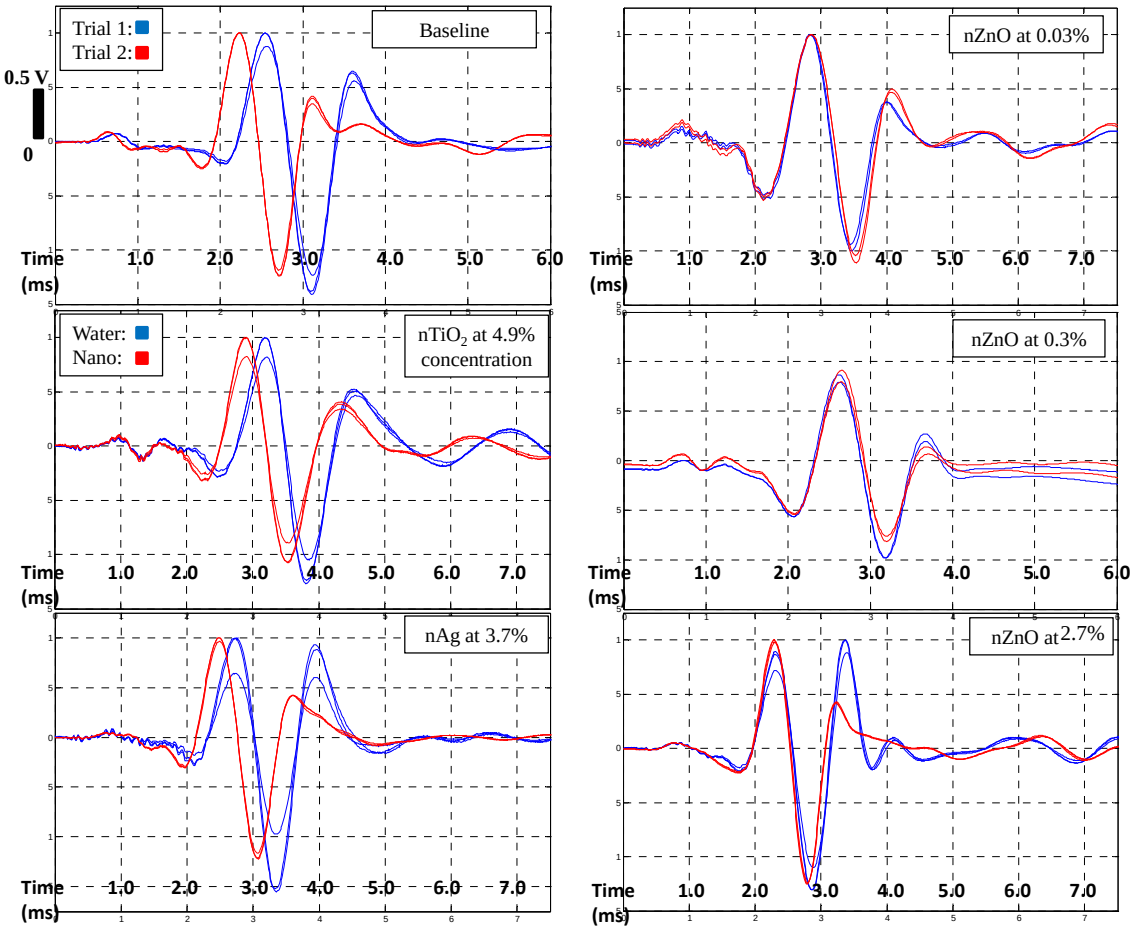

Figure 8.26. Signals from shear waves comparing response in the presence of nanoparticles to the baseline received signal.

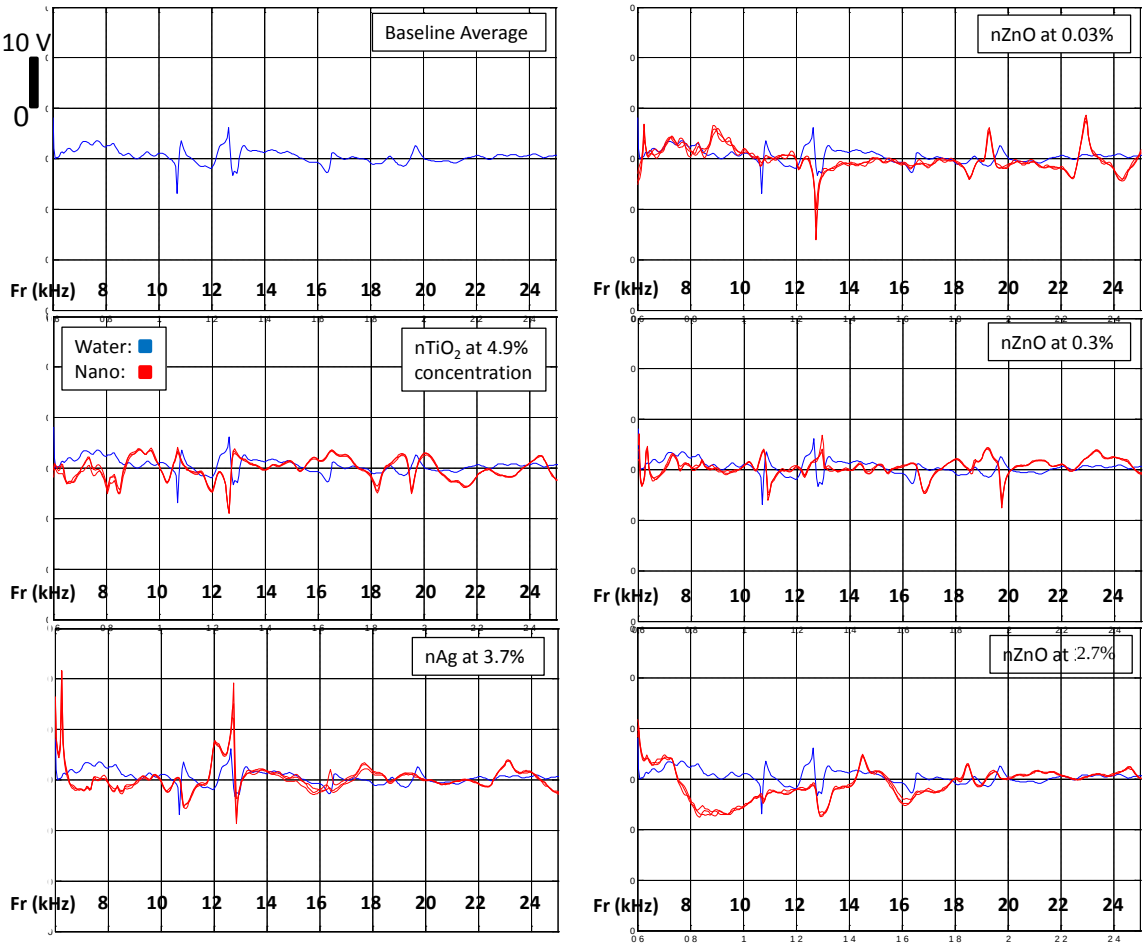

Figure 8.27. Signals from 30 kHz sweeps comparing response in the presence of nanoparticles to the baseline.

CHAPTER 9

CONCLUSIONS AND RECOMMENDATIONS

This chapter presents the conclusions and recommendations of the research, and also presents new research questions that arose due to this study.

9.1 Conclusions

A laboratory test system using bender elements was constructed for the study of seismic body wave propagation to address the response of nanoparticles dispersed in saturated granular media. The system was calibrated in air, water and water-saturated glass beads. Waveforms considered for testing were square waves and sine waves. Based on the literature, sine waves were judged to be better suited, mainly because near-field effects are less pronounced. Sine waves at different frequencies, optimized for transmission of shear and compression, were used in all testing described in this report.

Testing baselines for water-saturated glass bead specimens were established by analyzing the responses between consecutive tests on the same specimen, separated only by draining and refilling the pore fluid (trial 1 and trial 2). Baseline responses were established with respect to compression and shear waves in the time domain, and spectral response. Fast P-waves were not detectible with the experimental apparatus, but slow P-waves were. Tests for slow P-waves showed negligible difference between trials in arrival times, while characteristic-point amplitudes for trial 1 were larger than trial 2 by about 26%. Tests for S-waves showed arrival times for trial 1 were consistently 5 - 13%

slower than in trial 2. Differences are attributed to changes in consolidation state of the test specimen caused by draining and refilling pore spaces. Only S-wave amplitudes from trial 2 produced repeatable results, so these were used as the baseline. Spectral response testing showed good repeatability in the range of high coherence, 7 to 25 kHz.

An acceptability criterion was proposed to compare water trials of the nanoparticle dispersion tests against baseline; the S-wave velocity test for $nTiO_2$ failed to meet the criterion. Criteria were also proposed to evaluate the detectability of nanoparticle dispersions. Testing with nanoparticle dispersions showed that the system was capable of registering subtle changes in response caused by pore fluid content. Only the nZnO was tested at different concentrations, and detectabilities fluctuated between concentration levels. From the quantitative criteria, testing in the presence of nZnO showed uniform detectability for shear wave arrivals, fluctuating detectability for both shear and compression wave amplitudes, and no detectability for compression wave arrivals. nAg showed detectability only for compression amplitude, and $nTiO_2$ did not show detectability. From the qualitative criteria, testing in the presence of nZnO at 0.03%, 0.3% and 2.7%; nAg at 3.7%; and $nTiO_2$ at 4.9% showed detectability for spectral response, and no nanoparticles showed detectability for phase shift. Further tests for spectral response and phase shift would be needed to obtain quantifiable criteria from which detectability thresholds can be established.

Even though this report was performed in a controlled laboratory setting, the results suggest a potential for the seismic detectability of some nanoparticles in the natural environment. Since the seismic p-wave, s-wave, and spectral response was detectable for the above mentioned nanoparticles the application of surface seismic methods to directly

or indirectly detect nanoparticles in the natural environment may yield a measureable response. If an industrial nanoparticle leak, or transportation accident releases nanoparticles into the near subsurface resulting in detectable concentrations, then a non-invasive surface seismic survey may assist in the characterization and mapping of such a nanoparticle plume. This non-invasive geophysical mapping would then be utilized to target the plume for future investigations. Of course, for this to be fully realized, future research is required to understand the seismic response to nanoparticles within more complicated geologic settings as well as the biogeochemical reactions which are likely to occur from such a nanoparticle exposure. Regardless, the results from this study indicate that it is feasible to detect the alteration of seismic properties due to the presence of some nanoparticles within a glass bead matrix. Future research will expand upon these results by increase the complexity of the experimentation and improving the testing apparatus.

9.2 Recommendations

It was realized that the received signals achieved with this test system could be improved, and the following section gives recommendations on how to improve the test system.

1. Improve repeatability of the test by refining placement practices for the glass beads and modifying methods for soaking and seating the glass beads. The initial placement of the glass beads might be improved in terms of seating by using an orbital shaker or a vibration table.

2. The number of wetting and draining cycles prior to carrying out testing should be increased. The effects of the wetting and draining cycles can be observed with the shear wave velocities from the baseline tests, which showed consistently higher velocities for the second trial than the first trial, by 5 to 13%. This implies that the process of repetitive wetting and draining of the glass beads continually improved the seating of the glass beads.
3. The specimen height should be re-measured after each wetting and draining cycle to check for deviation in height from initial preparation state. The change in specimen height affects velocity (travel time), also amplitude to some extent.
4. The pulse signals were timed at 10-ms intervals; this restricted the quiet time between them. These effects can be nullified by lengthening testing intervals.
5. The precision of results can be improved by increasing sampling rates for recording received signals.
6. Consider testing different tip-to-tip distances (i.e. L value) depending on what types of waves are being analyzed. When P-waves are being focused on, the L value can be increased within limits dictated by signal attenuation so that fast P-wave arrivals are not influenced by crosstalk. When S-waves are being focused on, the L value can be decreased within limits dictated by near field effects to enhance the S-wave arrival and reduce effects of side reflections.
7. To further reduce the near-field effects on the S-wave arrivals, a distorted sine-wave can be considered for the input signal. This input was shown to reduce the near-field effects in research done by Arroyo et al. (2003) and Jovičić et al. (1996).

8. When testing in air, a lower cut off frequency for the high-pass filter should be explored; in this study a 1 kHz high-pass filter was used to remove a 32 Hz disturbance.
9. The reciprocity of the system should be tested to document accuracy by switching the transmitter from the base plate to the top cap element.
10. The effects of nanoparticle dispersions in the absence of a granular matrix could also be studied to further characterize them within the testing systems capabilities. A baseline for a test such as this would be distilled water in the absence of granular media.
11. For testing with the cross correlation method, filtering options and post processing procedures should be explored to remove transfer functions and effects of multiple reflections and other scattering on the received signal that dominate the wave train at later times.
12. Processing of unwrapped phase data by shifting traces to have a common starting point, where multiple traces would coincide with each other and lead to better analysis should be explored.
13. The presence of nZnO at low and medium concentrations was detectable by S-wave amplitudes, but it was not detectable at high concentration. This conflicting outcome is not understood and merits further study. Also, future testing with nanoparticle dispersions could be carried out at lower concentration levels to check for variations.

9.3 New Research Questions

1. Why do nZnO particles appear to be more detectible than $nTiO_2$ or nAg by this seismic method? Is it the substance being tested, or is it the testing method?
2. What are the effects of varying nanoparticle diameter?
3. What is the physical explanation at the nano scale for the observed results?
4. What are the effects of sample aging on detecting nanoparticle dispersions with seismic methods?

ACKNOWLEDGEMENTS

We appreciate all the facilities provided by the UNLV Applied Geophysics Center, and Department of Civil and Environmental Engineering and the U.S. The information in this document has been funded partly by the United States Environmental Protection Agency under student services contract EP09D000305 to M. Nihad Rajabdeen. It has been subjected to the Agency's peer and administrative review and has been approved for publication as an EPA document. Mention of trade names or commercial products does not constitute endorsement or recommendation by EPA for use.

A special thank you to Drs. Carlos Santamarina and Changho Lee at Georgia Institute of Technology; their advice on the design of the bender element testing system is greatly appreciated. Also the following individuals helped with the little things that made this research a success: Danney Glaser, John Zimmerman, Kim Rogers, Katrina Varner, Steve Gardner and Marion Edison (U.S. EPA); Chris Cothrun, Helena Murvosh, Suchan Lamichhane, Pinthep Kittipongdaja, Prajwol Tamrakar and Shawn Andersen (UNLV AGC); Allen Sampson, Levia Lanier, Stacey Fisher, Kristen Young and Lily Magana (UNLV).

APPENDIX 1 TABLES

Formulas used for calculations

1. Percentage Difference $= \frac{Anticipated - Experimental}{Anticipated} \times 100\%$

2. Percentage Difference $= \frac{Trial\ 1 - Trial\ 2}{Trial\ 1} \times 100\%$

3. Velocity $= \frac{Distance\ travelled}{Time\ taken}$

4. Moisture content (ω %) $= \frac{M_w}{M_{Gb}} = \frac{Mass\ of\ water}{Mass\ of\ glass\ beads}$

5. Void ratio (e) $= (\omega\ \%) \times G_S$

    - G_s : Specific gravity of glass beads = 2.5

6. Saturated unit weight (γ_{sat}) $= \left[\frac{G_S + e}{1 + e}\right] \times \gamma_W$

    - γ_W = 9.81 kN/m^3

Table A.1. Physical properties for glass bead specimens prepared with dumping method

Specimen	Glass beads (grams)	Water (grams)	ω (%)	e	γ_{sat} (kN/m^3)	Difference from Average
1	2256	543	24	0.60	19.0	0.41%
2	2193	555	25	0.63	18.8	0.51%
3	2216	543	24	0.61	18.9	0.09%
Average	2221	547	25	0.62	18.9	

- (ω) – Moisture content of the glass beads when fully soaked
- (e) – Void ratio
- γ_{sat} – Saturated unit weight

Table A.2. Physical properties for glass bead specimens prepared with stage fill method

Specimen	Glass beads (grams)	Water (grams)	ω (%)	e	γ_{sat} (kN/m^3)	Difference from Average
1	2194	566	26	0.65	18.8	0.02%
2	2200	574	26	0.65	18.7	0.17%
3	2193	562	26	0.64	18.8	0.15%
Average	2196	568	26	0.65	18.7	

- (ω) – Moisture content of the glass beads when fully soaked
- (e) – Void ratio
- γ_{sat} – Saturated unit weight

Table A.3. Physical properties for tested water-saturated glass bead specimens

Specimen	Glass beads (grams)	Physical state	Volume (ml)*	ω (%)	e	γ_{sat} (kN/m^3)
1	1951	Initial wetting	995	51	1.28	16.3
		Drained state 1	234	12	0.30	21.1
		Trial 1	351	30	0.75	18.2
		Drained State 2	234	12	0.30	21.1
		Trial 2	351	30	0.75	18.2
2	1961	Initial wetting	981	50	1.25	16.4
		Drained state 1	235	12	0.30	21.1
		Trial 1	392	32	0.80	18.0
		Drained State 2	255	13	0.33	20.9
		Trial 2	373	32	0.80	18.0
3	1951	Initial wetting	976	50	1.25	16.4
		Drained state 1	254	13	0.33	20.9
		Trial 1	332	30	0.75	18.2
		Drained State 2	234	12	0.30	21.1
		Trial 2	351	30	0.75	18.2

*Volume associated with drained state is volume retained in the column, and volume associated with trials is volume required to saturate the specimen

- Trial 2 represents duplicate tests following drainage and rewetting of test specimen.
- (ω) – Moisture content of the glass beads when fully soaked
- (e) – Void ratio
- γ_{sat} – Saturated unit weight

Table A.4. Characteristics for specimens during nanoparticle dispersion testing

Specimen (concentration)	Mass of glass beads (grams)	Physical state	Volume (ml)*	ω (%)	e	γ_{sat} (kN/m^3)
nZnO (0.03%)	1960	Initial wetting	950	48	1.20	16.5
		Drained state 1	333	17	0.43	20.1
		Water trial	290	32	0.80	18.0
		Drained state 2	347	18	0.45	20.0
		Nano trial	185	27	0.68	18.6
nZnO (0.3%)	1960	Initial wetting	958	49	1.23	16.4
		Drained state 1	238	12	0.30	21.1
		Water trial	383	32	0.80	18.0
		Drained state 2	277	14	0.35	20.7
		Nano trial	213	25	0.63	18.9
nZnO (2.7%)	1971	Initial wetting	986	50	1.25	16.4
		Drained state 1	237	12	0.30	21.1
		Water trial	394	32	0.80	18.0
		Drained state 2	246	13	0.33	20.9
		Nano trial	375	32	0.80	18.0
$nTiO_2$ (4.9%)	1958	Initial wetting	960	49	1.23	16.4
		Drained state 1	157	8	0.20	22.1
		Water trial	392	28	0.70	18.5
		Drained state 2	156	8	0.20	22.1
		Nano trial	370	27	0.68	18.6
nAg (3.7%)	1966	Initial wetting	964	49	1.23	16.4
		Drained state 1	216	11	0.28	21.4
		Water trial	374	30	0.75	18.2
		Drained state 2	246	13	0.33	20.9
		Nano trial	347	30	0.75	18.2

*Volume associated with drained state is volume retained in the column, and volume associated with trials is volume required to saturate the specimen

- Nano Trial represents duplicate tests following drainage and rewetting of test specimen.
- (ω) – Moisture content of the glass beads when fully soaked
- (e) – Void ratio
- γ_{sat} – Saturated unit weight

Table A.5. Direct (L) and reflected (D1+D2) travel path lengths used to calculate velocities

Specimen	**L (mm)**	**D1 + D2 (mm)**
Water-saturated 1	62.3	164.6
Water-saturated 2	60.7	164.0
Water-saturated 3	61.0	164.2
nZnO at 0.03% concentration	61.6	164.4
nZnO at 0.3% concentration	62.3	164.6
nZnO at 2.7% concentration	61.1	164.2
$nTiO_2$ at 4.9% concentration	60.9	164.1
nAg at 3.7% concentration	61.1	164.2

APPENDIX 2 FIGURES

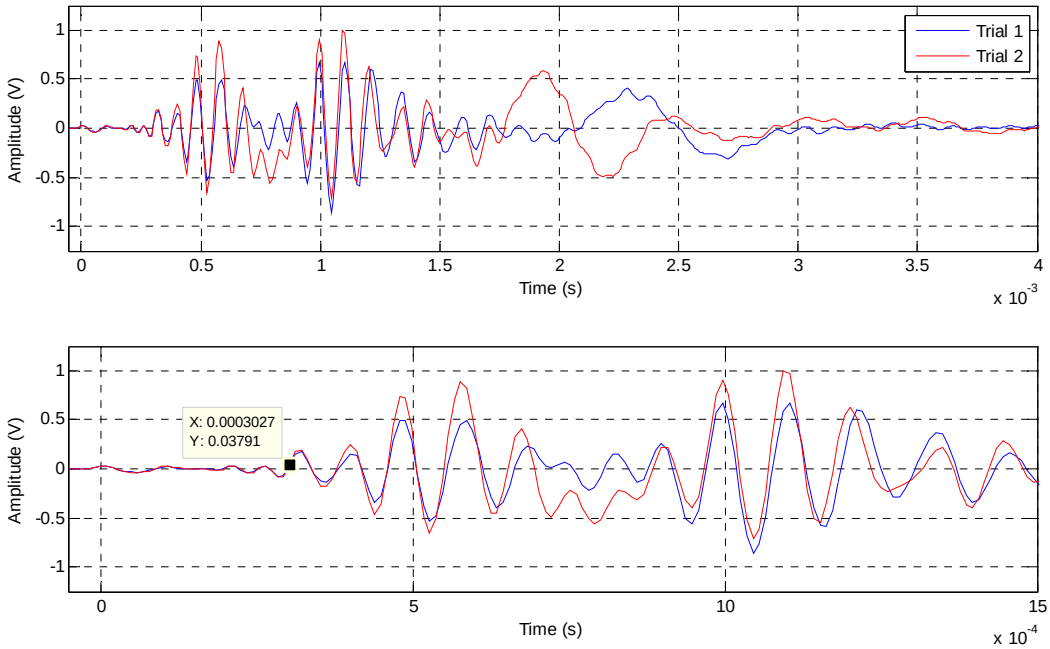

Figure A.1. Water-saturated glass bead specimen 1: comparison of 8 kHz pulse signal used to highlight slow compression wave arrivals, showing repetition 1 of trials 1 and 2; 1000 recordings averaged per repetition.

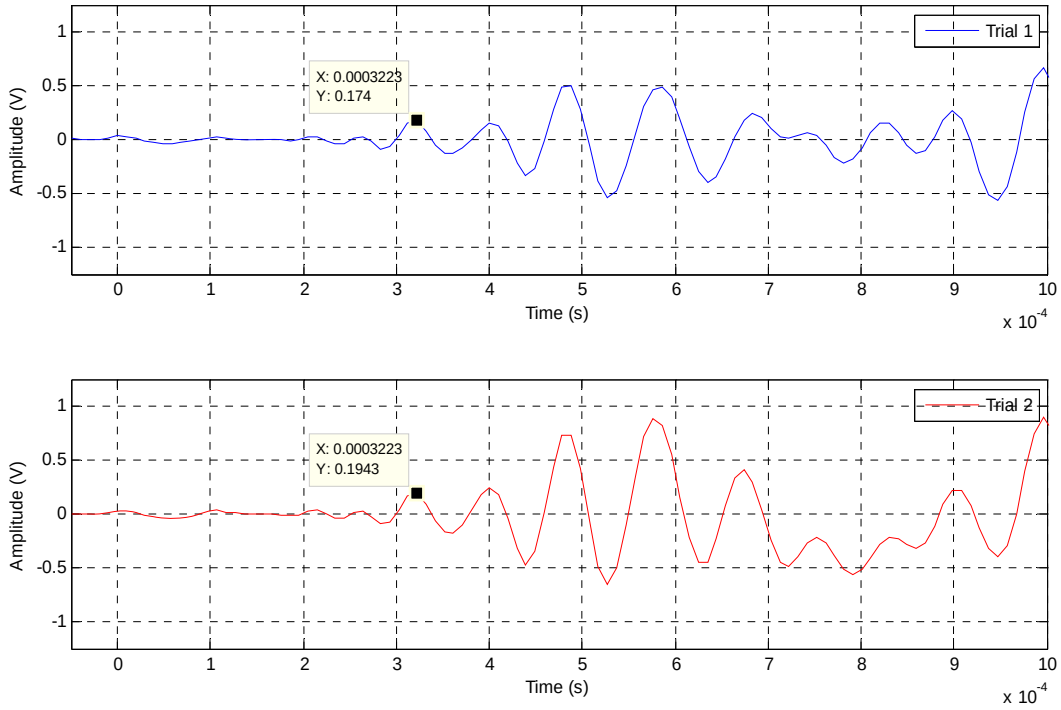

Figure A.2. Water-saturated glass bead specimen 1: comparison of 8 kHz pulse signal used to highlight slow compression wave amplitude, showing repetition 1 of trials 1 and 2; 1000 recordings averaged per repetition.

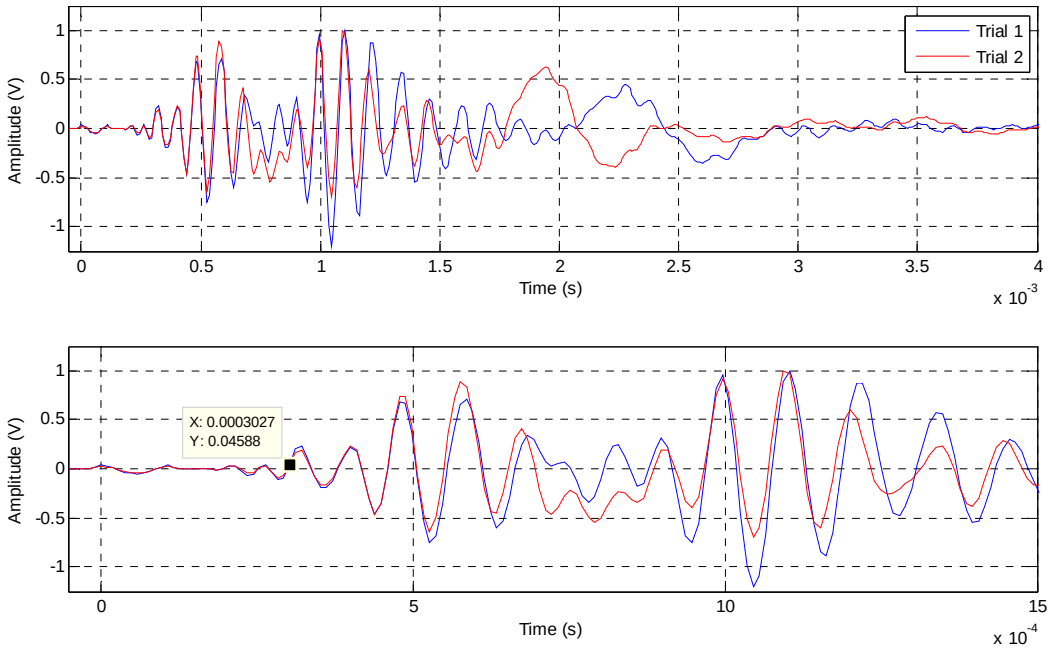

Figure A.3. Water-saturated glass bead specimen 1: comparison of 8 kHz pulse signal used to highlight slow compression wave arrivals, showing repetition 2 of trials 1 and 2; 1000 recordings averaged per repetition.

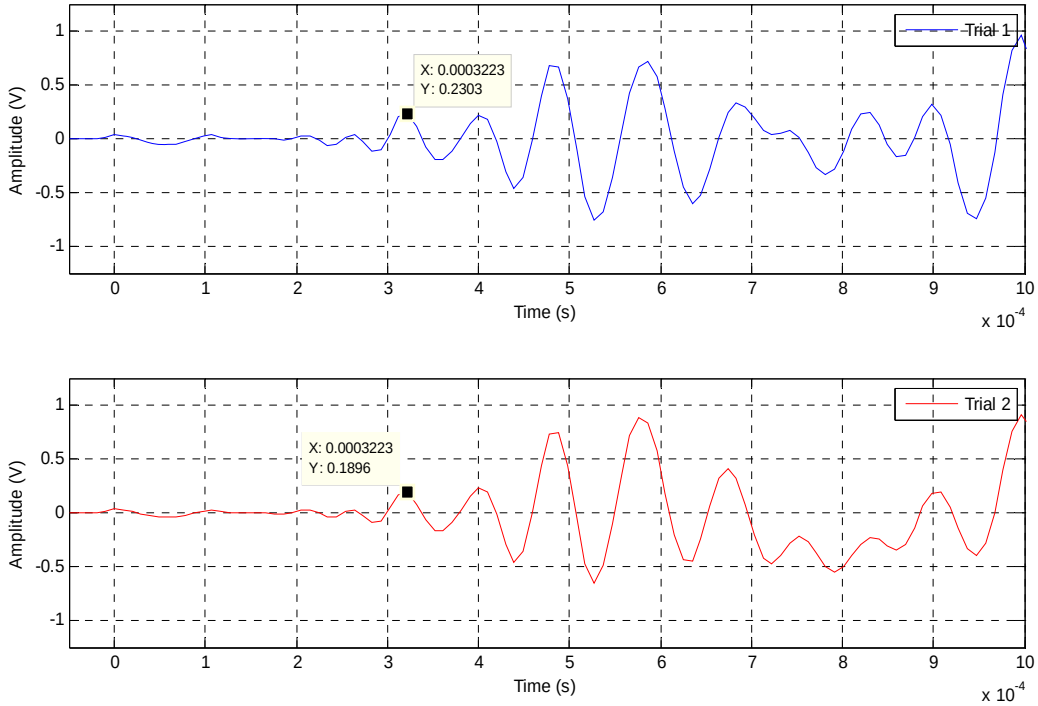

Figure A.4. Water-saturated glass bead specimen 1: comparison of 8 kHz pulse signal used to highlight slow compression wave amplitude, showing repetition 2 of trials 1 and 2; 1000 recordings averaged per repetition.

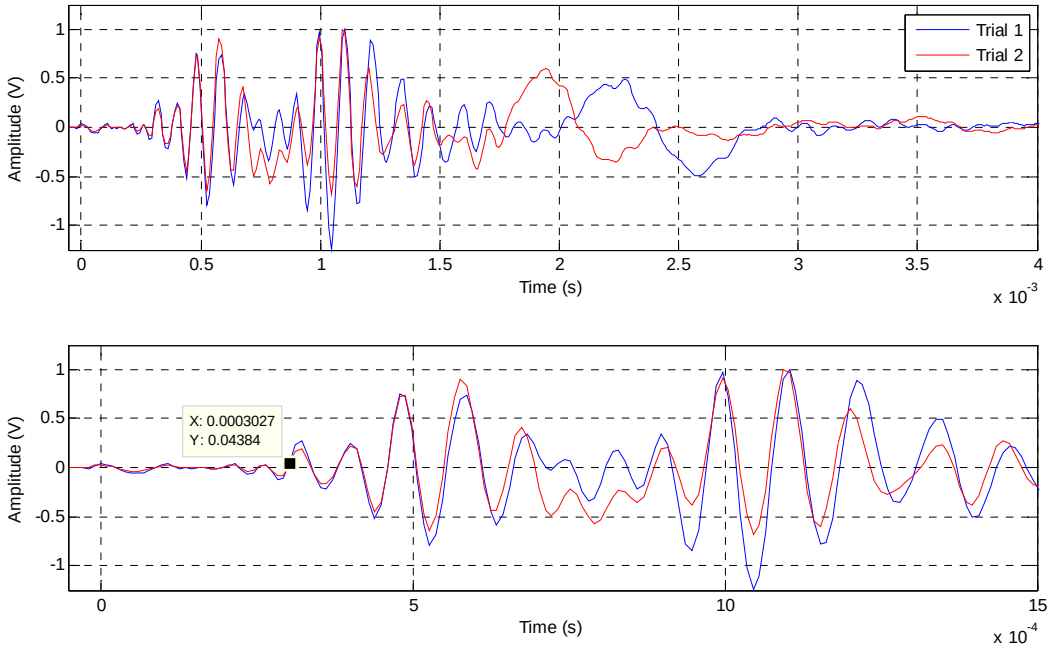

Figure A.5. Water-saturated glass bead specimen 1: comparison of 8 kHz pulse signal used to highlight slow compression wave arrivals, showing repetition 3 of trials 1 and 2; 1000 recordings averaged per repetition.

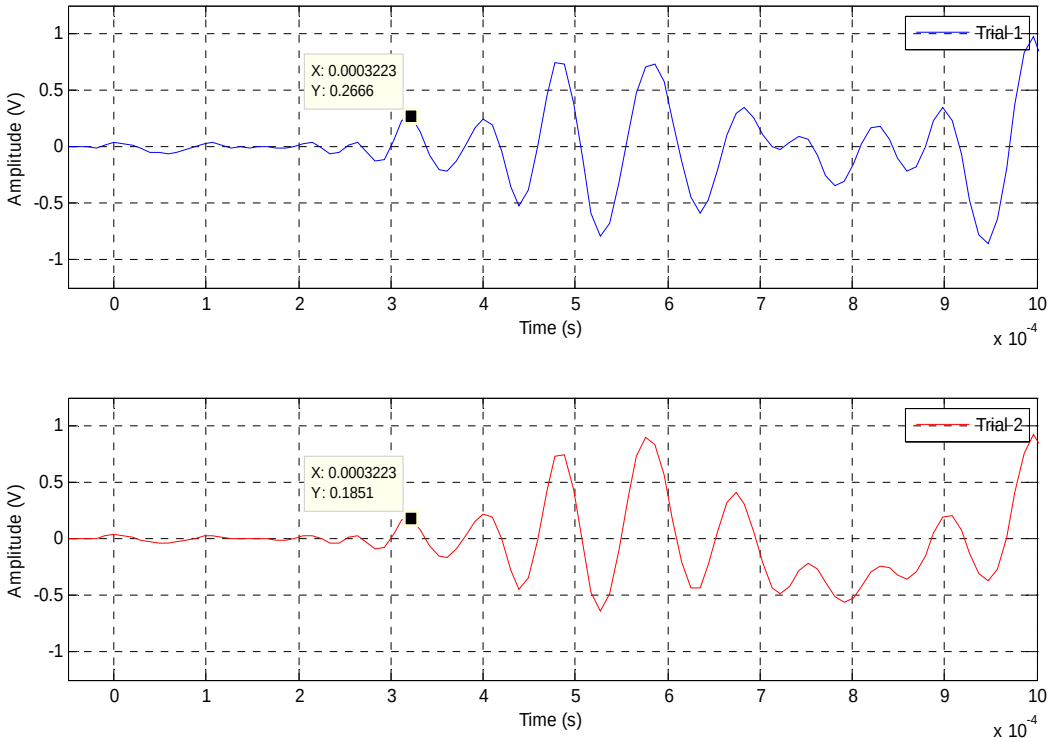

Figure A.6. Water-saturated glass bead specimen 1: comparison of 8 kHz pulse signal used to highlight slow compression wave amplitude, showing repetition 3 of trials 1 and 2; 1000 recordings averaged per repetition.

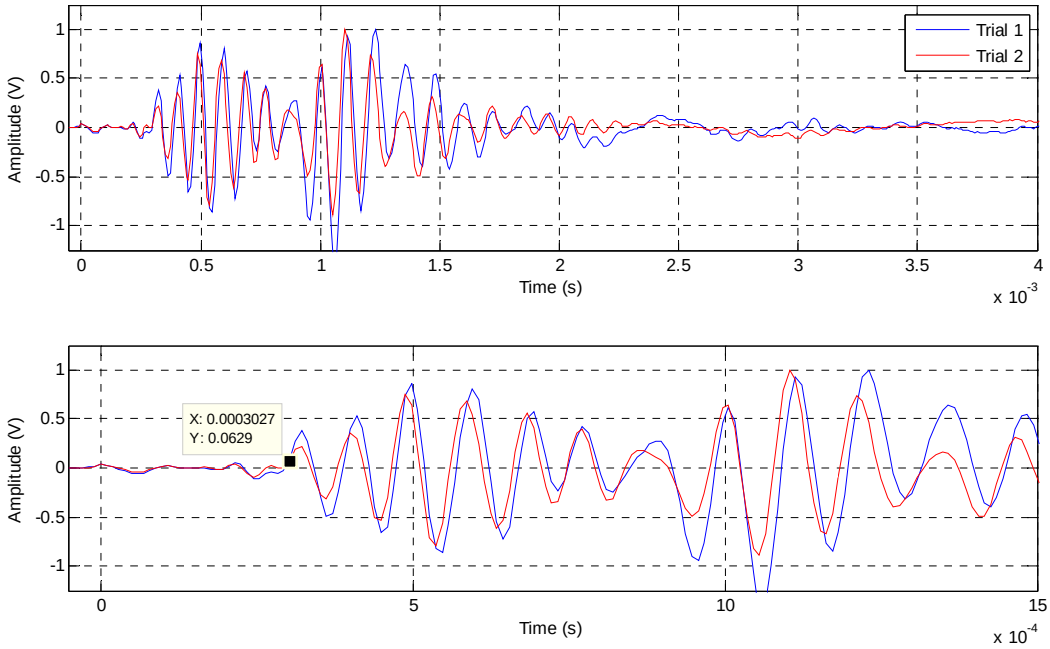

Figure A.7. Water-saturated glass bead specimen 2: comparison of 8 kHz pulse signal used to highlight slow compression wave arrivals, showing repetition 1 of trials 1 and 2; 1000 recordings averaged per repetition.

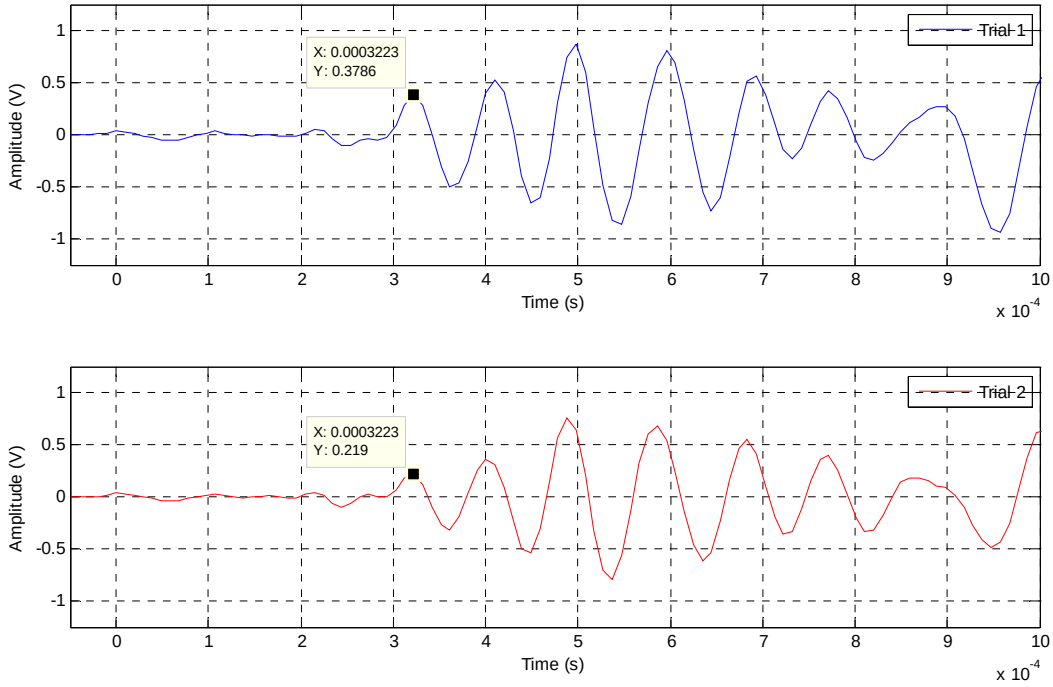

Figure A.8. Water-saturated glass bead specimen 2: comparison of 8 kHz pulse signal used to highlight slow compression wave amplitude, showing repetition 1 of trials 1 and 2; 1000 recordings averaged per repetition.

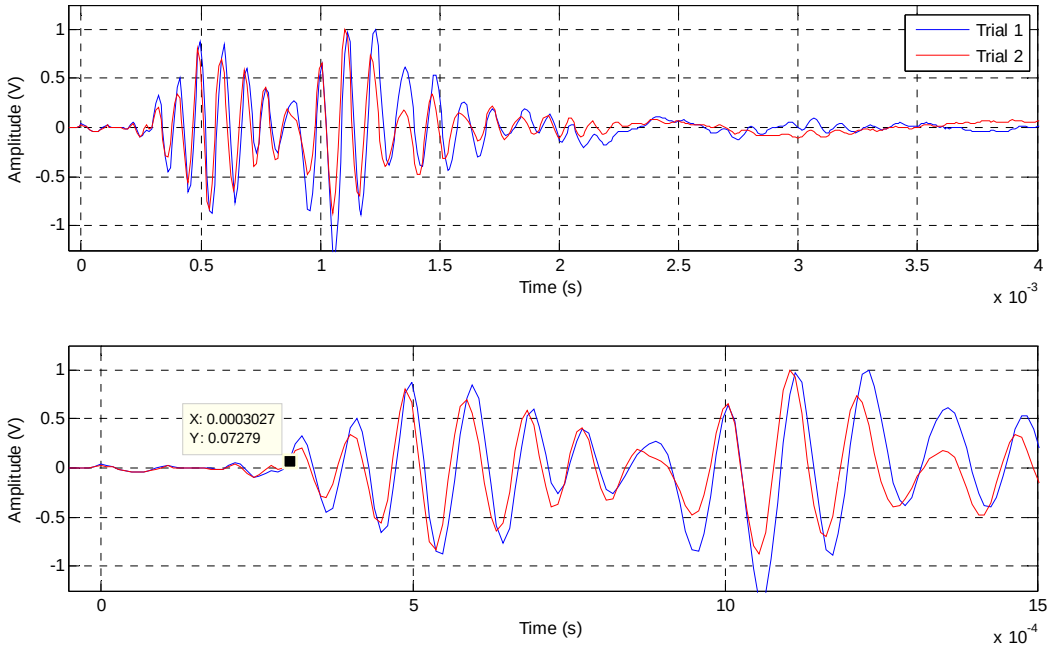

Figure A.9. Water-saturated glass bead specimen 2: comparison of 8 kHz pulse signal used to highlight slow compression wave arrivals, showing repetition 2 of trials 1 and 2; 1000 recordings averaged per repetition.

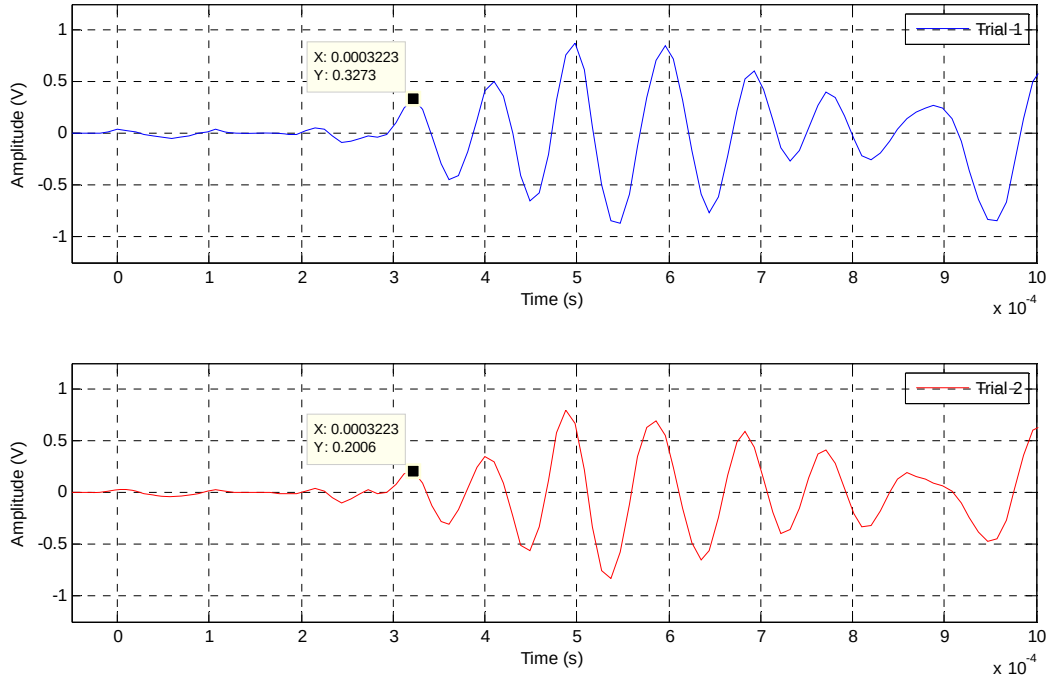

Figure A.10. Water-saturated glass bead specimen 2: comparison of 8 kHz pulse signal used to highlight slow compression wave amplitude, showing repetition 2 of trials 1 and 2; 1000 recordings averaged per repetition.

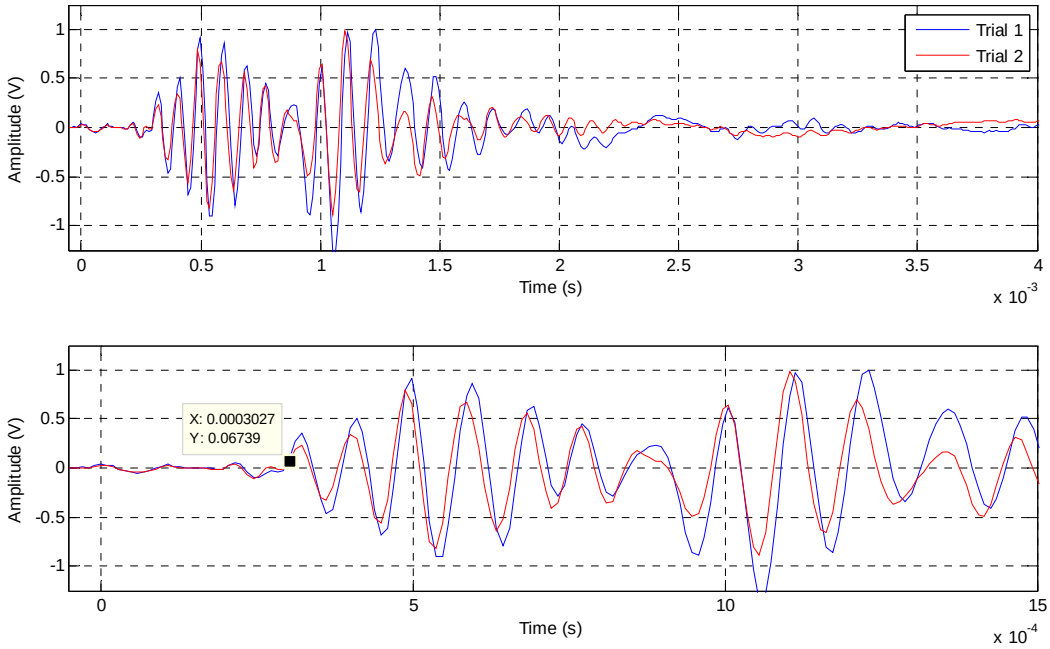

Figure A.11. Water-saturated glass bead specimen 2: comparison of 8 kHz pulse signal used to highlight slow compression wave arrivals, showing repetition 3 of trials 1 and 2; 1000 recordings averaged per repetition.

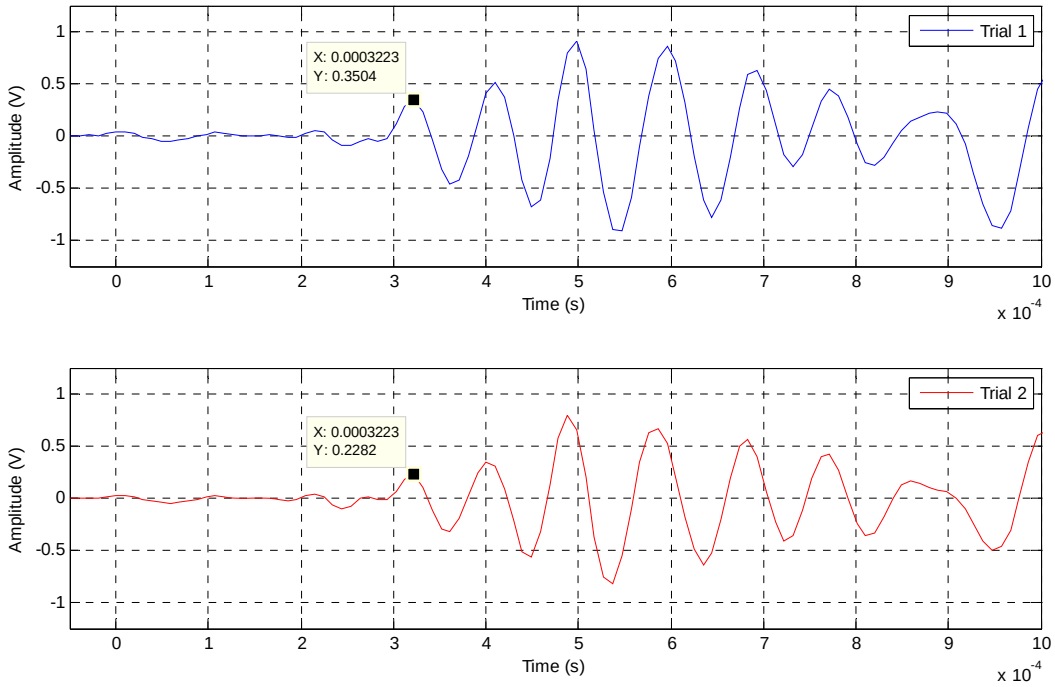

Figure A.12. Water-saturated glass bead specimen 2: comparison of 8 kHz pulse signal used to highlight slow compression wave amplitude, showing repetition 3 of trials 1 and 2; 1000 recordings averaged per repetition.

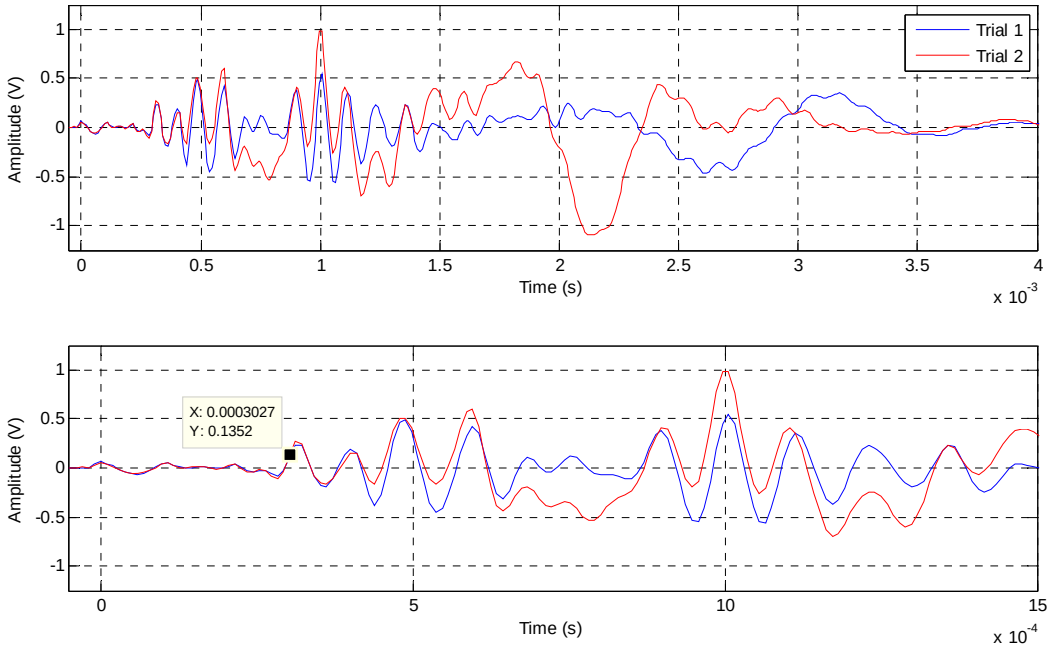

Figure A.13. Water-saturated glass bead specimen 3: comparison of 8 kHz pulse signal used to highlight slow compression wave arrivals, showing repetition 1 of trials 1 and 2; 1000 recordings averaged per repetition.

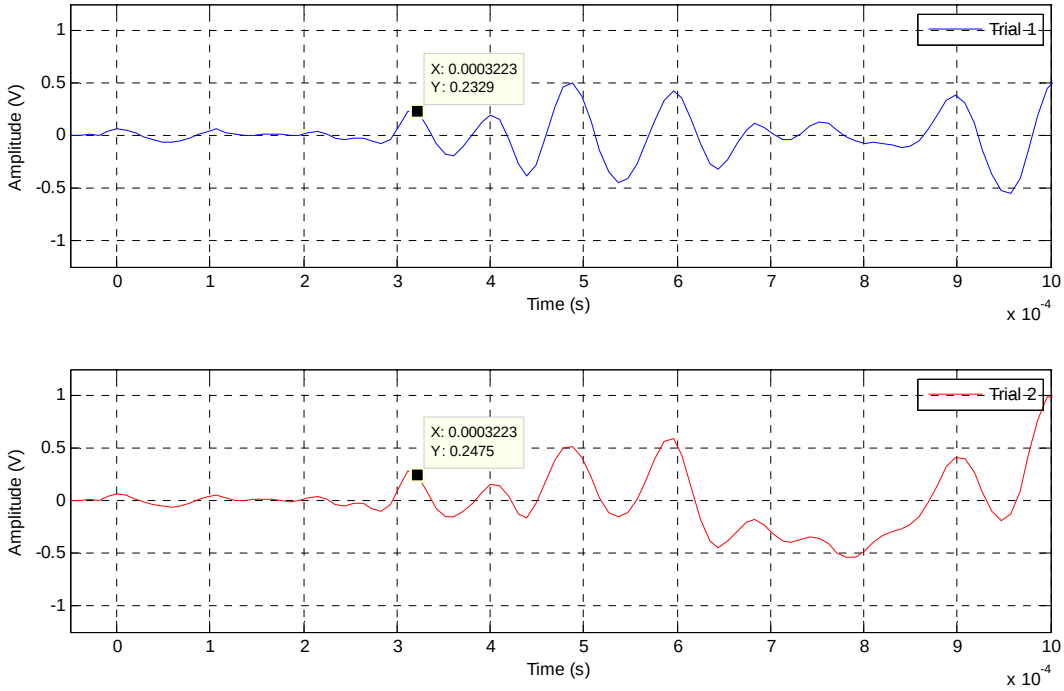

Figure A.14. Water-saturated glass bead specimen 3: comparison of 8 kHz pulse signal used to highlight slow compression wave amplitude, showing repetition 1 of trials 1 and 2; 1000 recordings averaged per repetition.

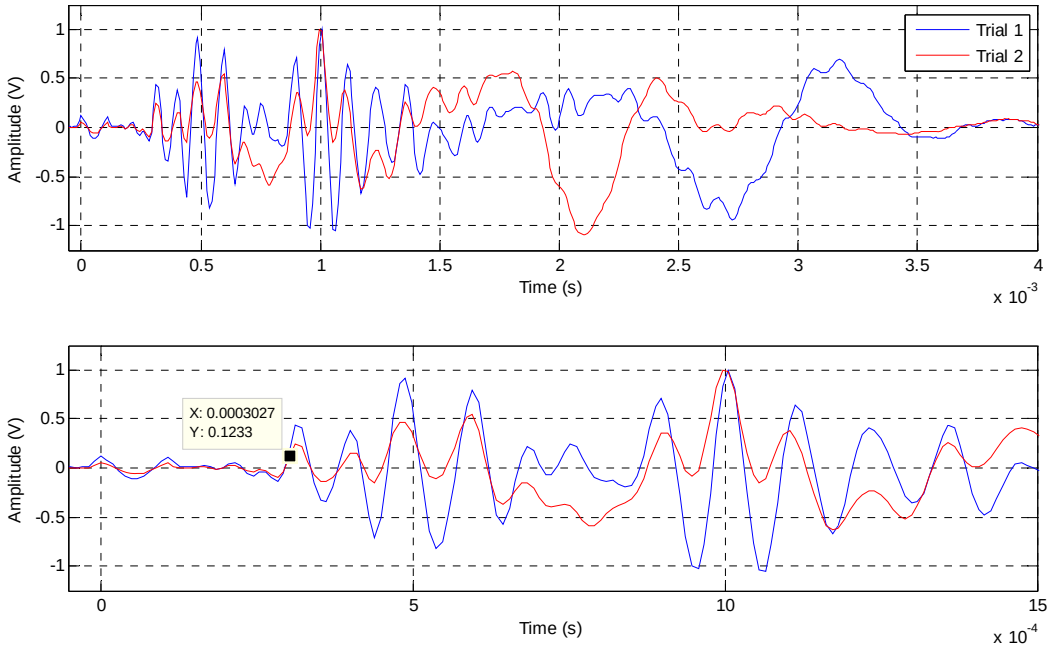

Figure A.15. Water-saturated glass bead specimen 3: comparison of 8 kHz pulse signal used to highlight slow compression wave arrivals, showing repetition 2 of trials 1 and 2; 1000 recordings averaged per repetition.

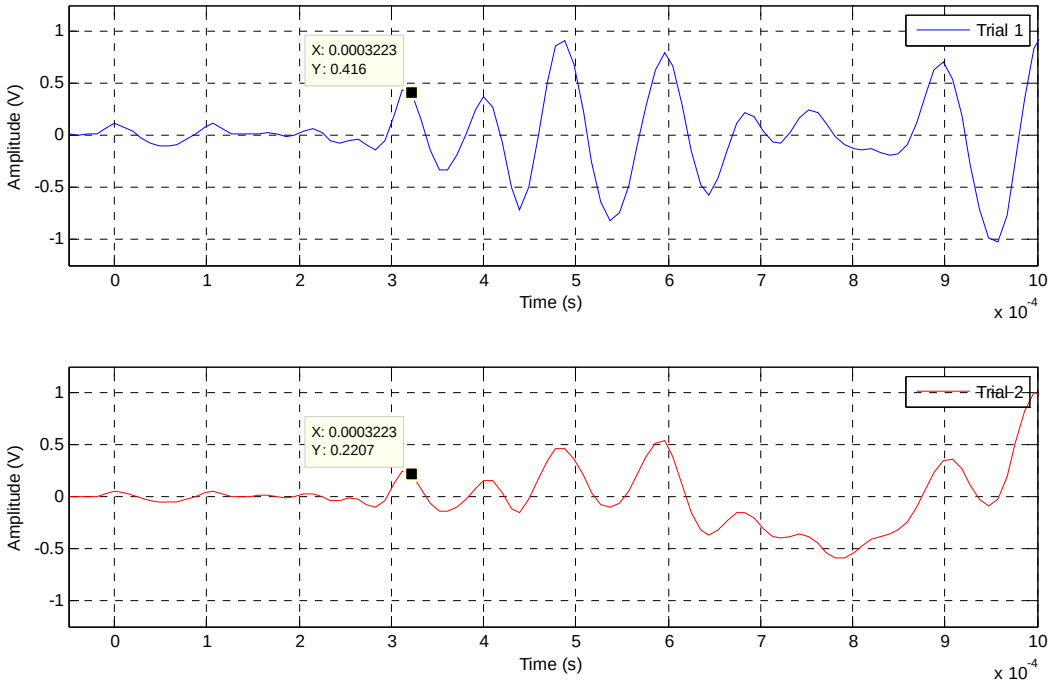

Figure A.16. Water-saturated glass bead specimen 3: comparison of 8 kHz pulse signal used to highlight slow compression wave amplitude, showing repetition 2 of trials 1 and 2; 1000 recordings averaged per repetition.

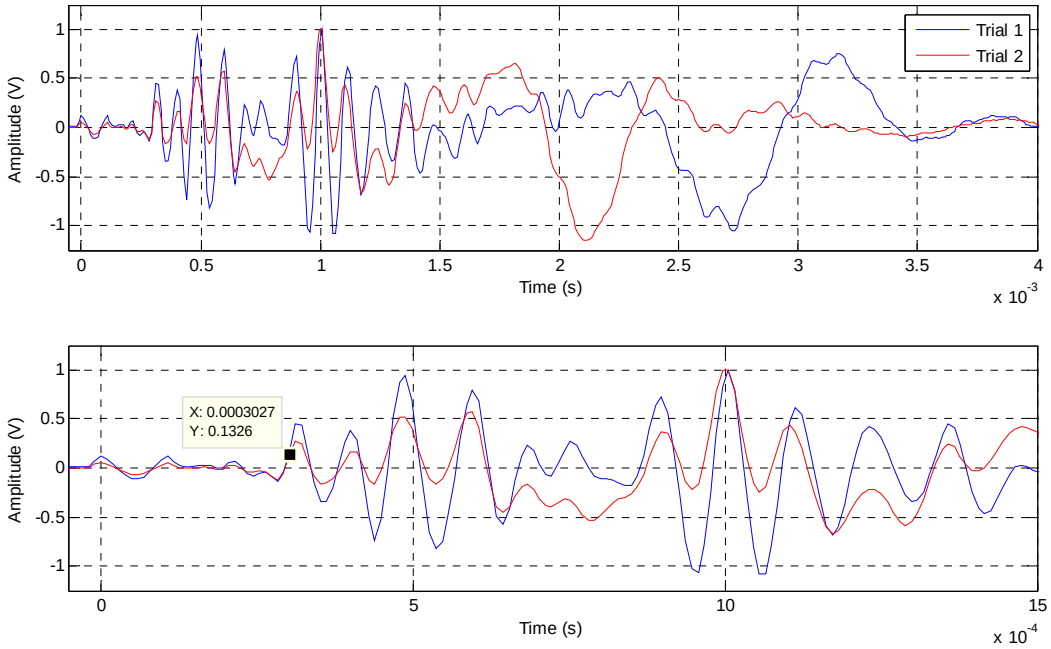

Figure A.17. Water-saturated glass bead specimen 3: comparison of 8 kHz pulse signal used to highlight slow compression wave arrivals, showing repetition 3 of trials 1 and 2; 1000 recordings averaged per repetition.

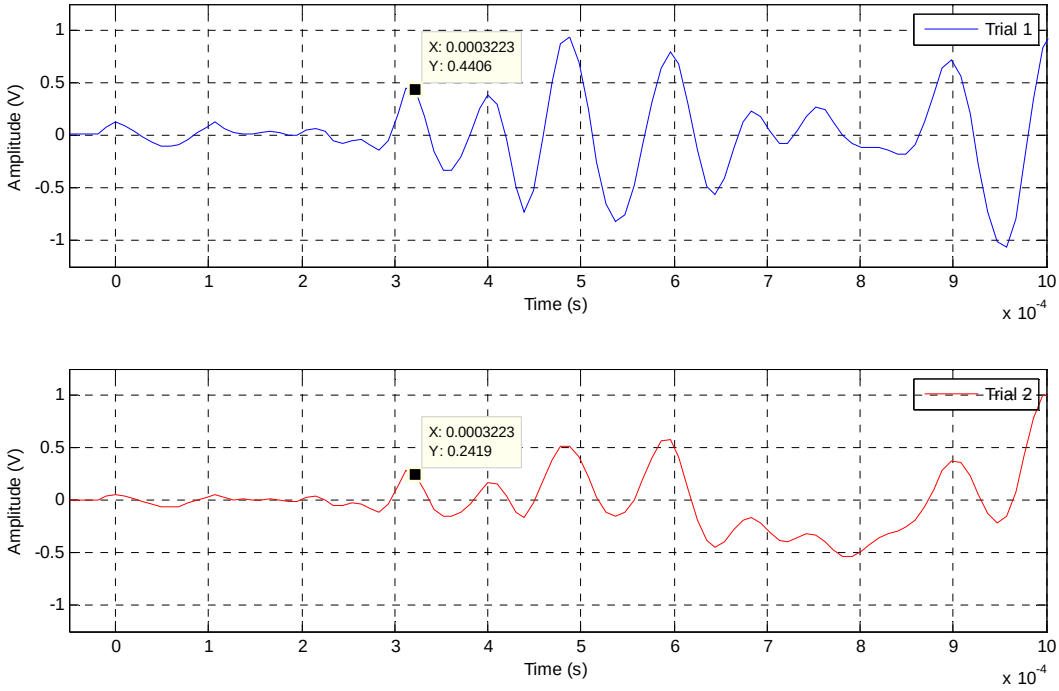

Figure A.18. Water-saturated glass bead specimen 3: comparison of 8 kHz pulse signal used to highlight slow compression wave amplitude, showing repetition 3 of trials 1 and 2; 1000 recordings averaged per repetition.

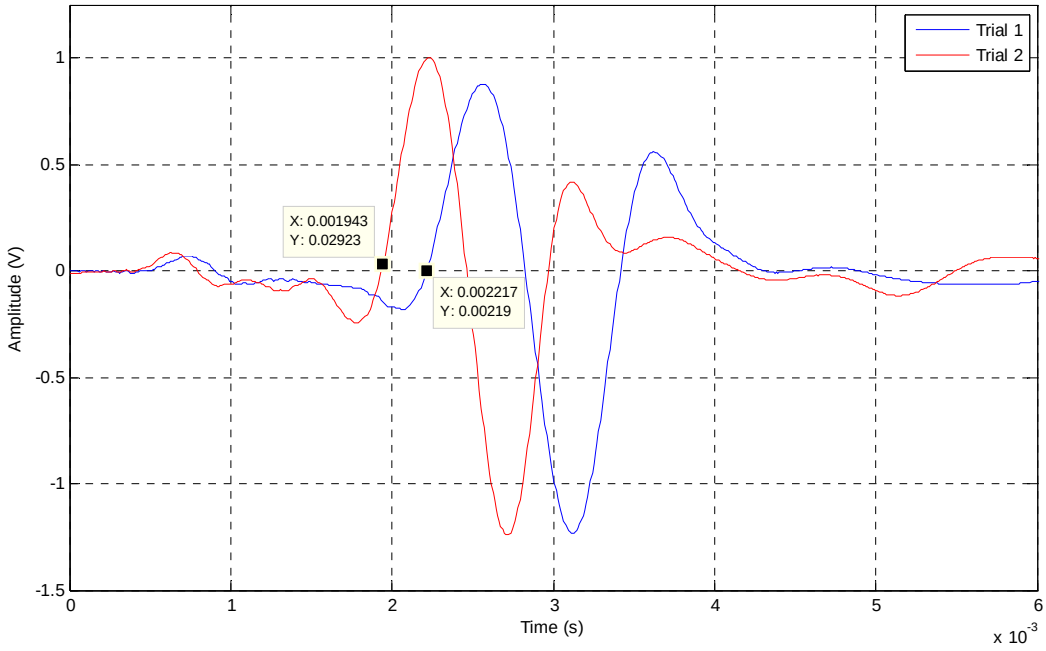

Figure A.19. Water-saturated glass bead specimen 1: comparison of 1 kHz pulse signal used to highlight shear, showing repetition 1 of trials 1 and 2; 1000 recordings averaged per repetition.

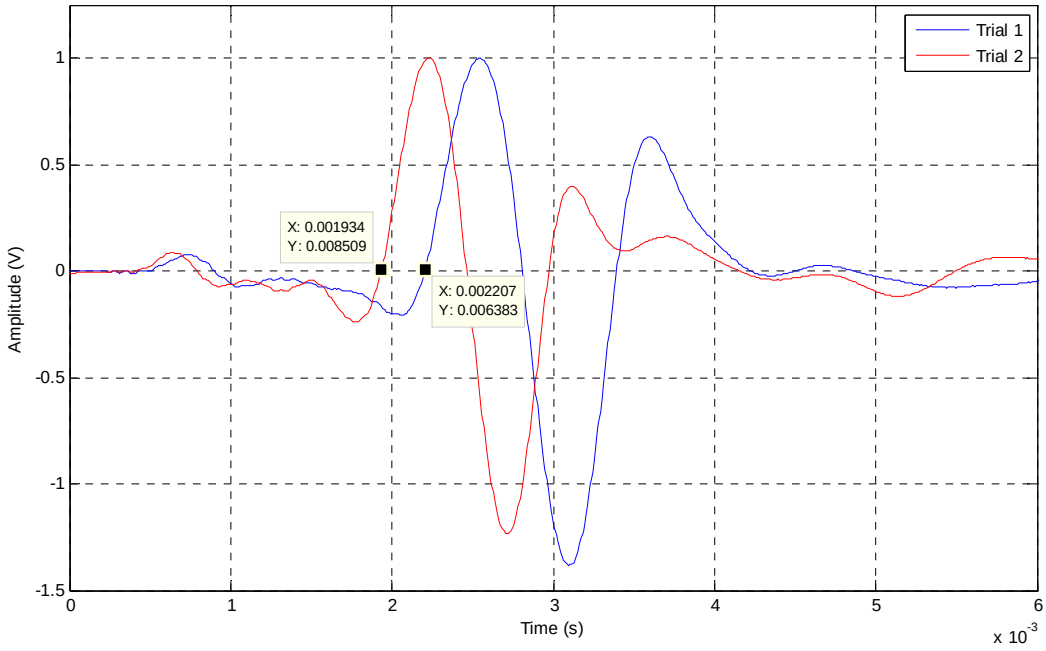

Figure A.20. Water-saturated glass bead specimen 1: comparison of 1 kHz pulse signal used to highlight shear, showing repetition 2 of trials 1 and 2; 1000 recordings averaged per repetition.

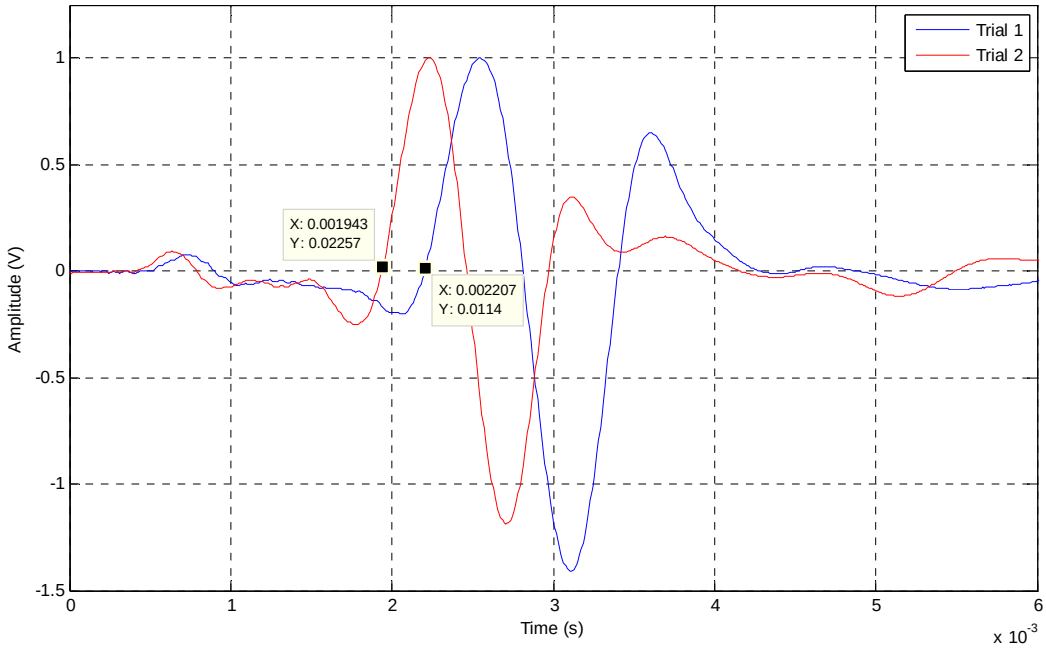

Figure A.21. Water-saturated glass bead specimen 1: comparison of 1 kHz pulse signal used to highlight shear, showing repetition 3 of trials 1 and 2; 1000 recordings averaged per repetition.

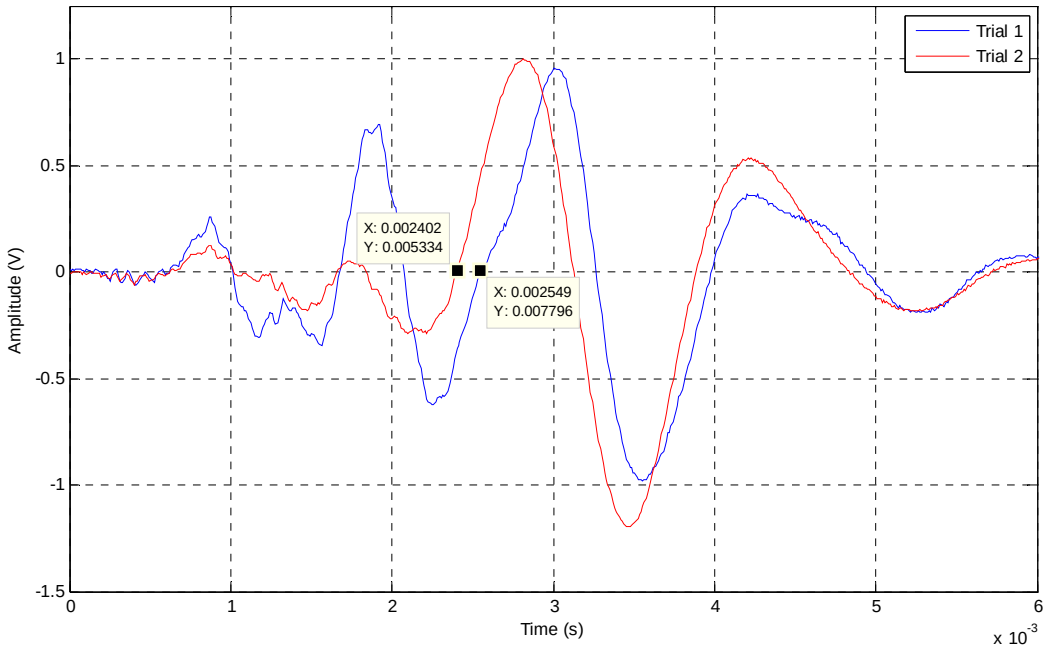

Figure A.22. Water-saturated glass bead specimen 2: comparison of 1 kHz pulse signal used to highlight shear, showing repetition 1 of trials 1 and 2; 1000 recordings averaged per repetition.

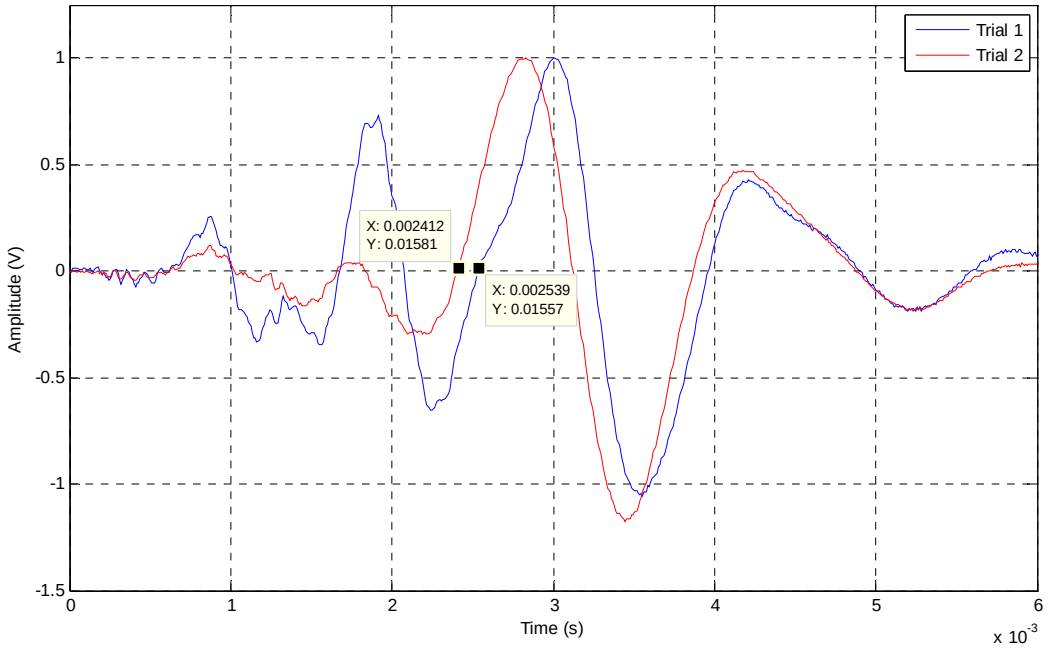

Figure A.23. Water-saturated glass bead specimen 2: comparison of 1 kHz pulse signal used to highlight shear, showing repetition 2 of trials 1 and 2; 1000 recordings averaged per repetition.

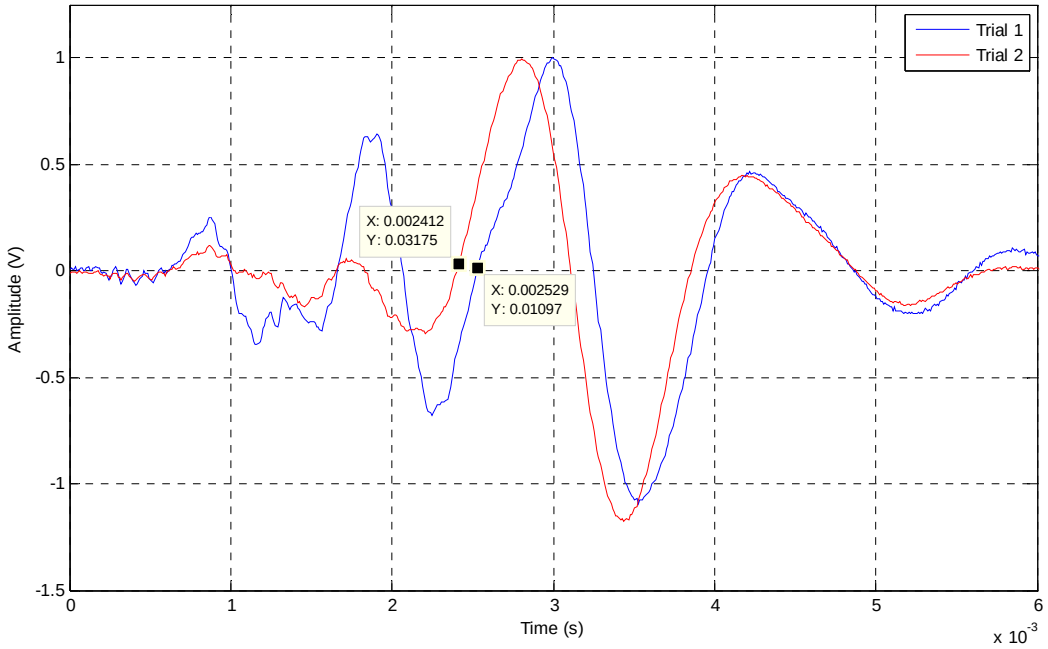

Figure A.24. Water-saturated glass bead specimen 2: comparison of 1 kHz pulse signal used to highlight shear, showing repetition 3 of trials 1 and 2; 1000 recordings averaged per repetition.

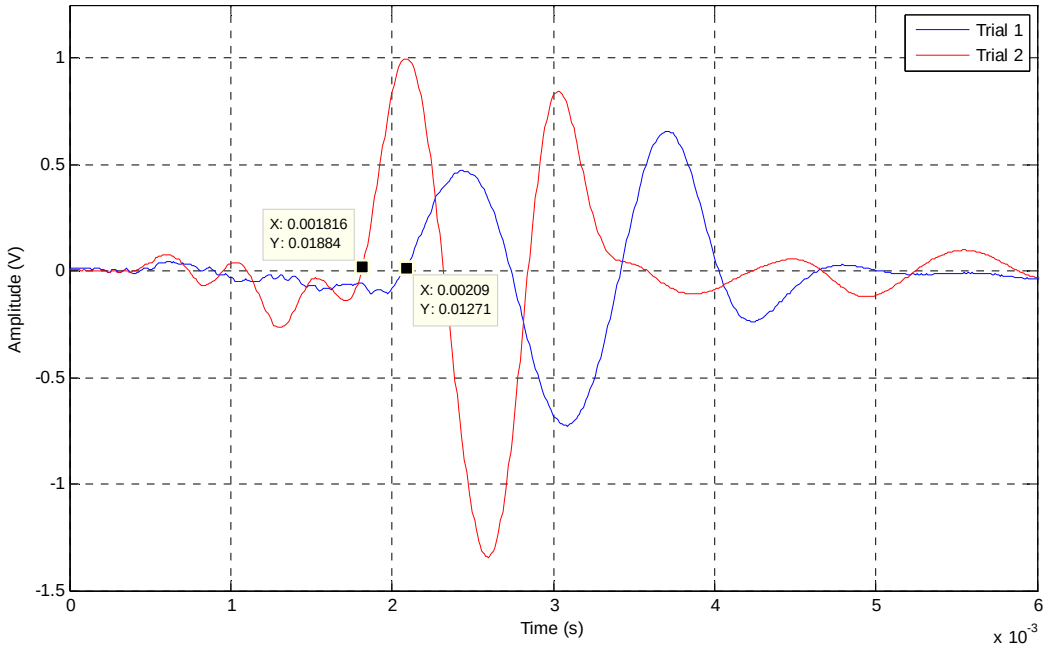

Figure A.25. Water-saturated glass bead specimen 3: comparison of 1 kHz pulse signal used to highlight shear, showing repetition 1 of trials 1 and 2; 1000 recordings averaged per repetition.

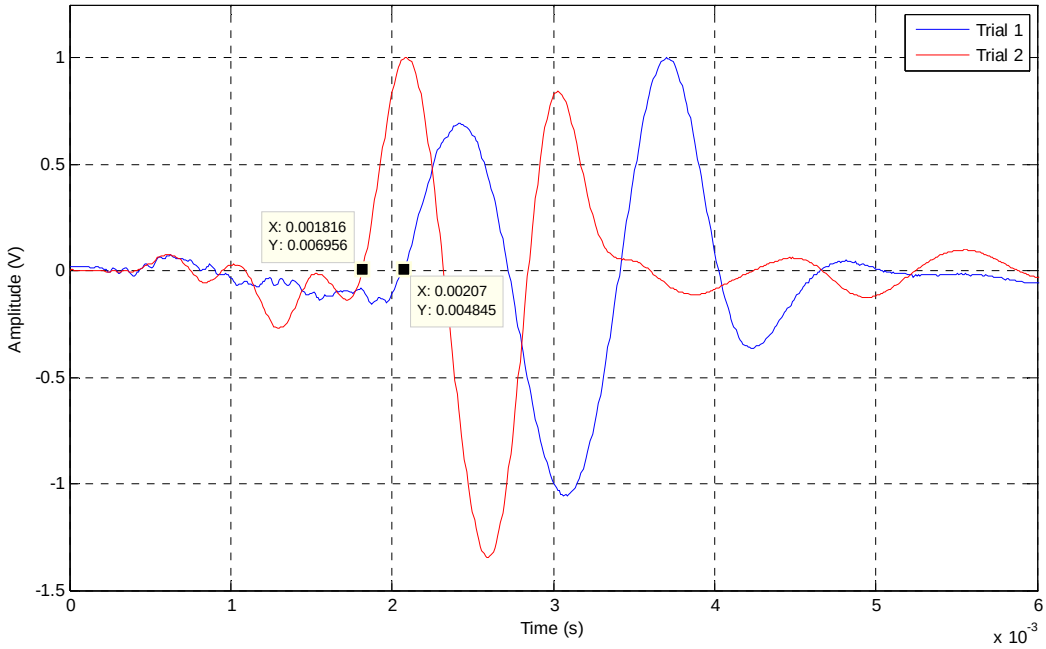

Figure A.26. Water-saturated glass bead specimen 3: comparison of 1 kHz pulse signal used to highlight shear, showing repetition 2 of trials 1 and 2; 1000 recordings averaged per repetition.

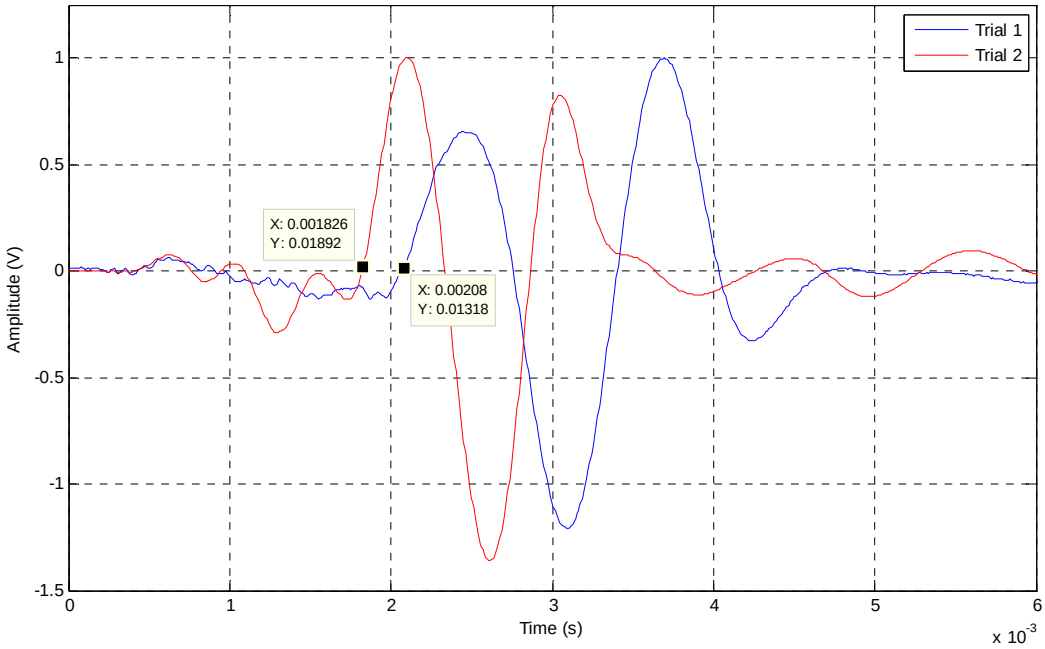

Figure A.27. Water-saturated glass bead specimen 3: comparison of 1 kHz pulse signal used to highlight shear, showing repetition 3 of trials 1 and 2; 1000 recordings averaged per repetition.

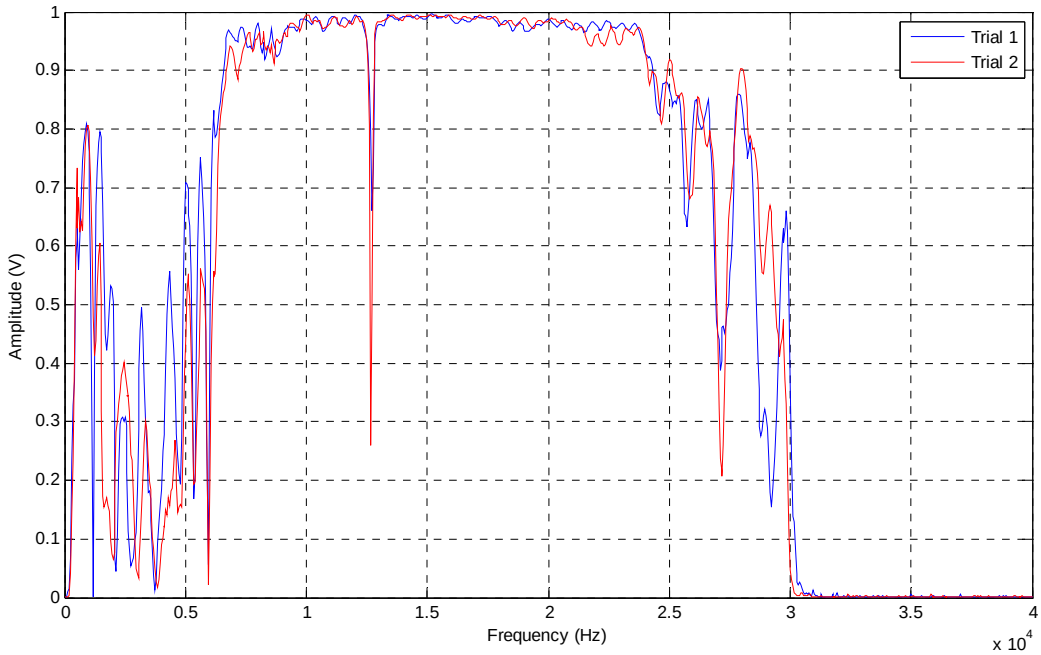

Figure A.28. Water-saturated glass bead specimen 2: analysis of coherence for frequency sweep of 0 - 30 kHz used to find high coherence range, showing a repetition of trials 1 and 2; 1000 recordings averaged per repetition.

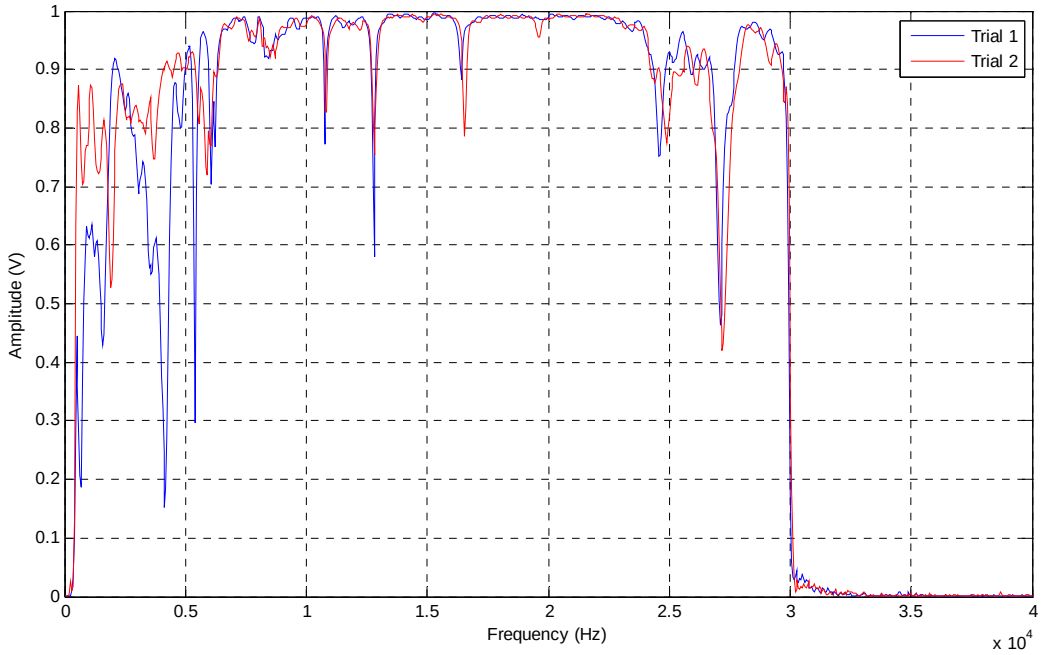

Figure A.29. Water-saturated glass bead specimen 3: analysis of coherence for frequency sweep of 0 - 30 kHz used to find high coherence range, showing a repetition of trials 1 and 2; 1000 recordings averaged per repetition.

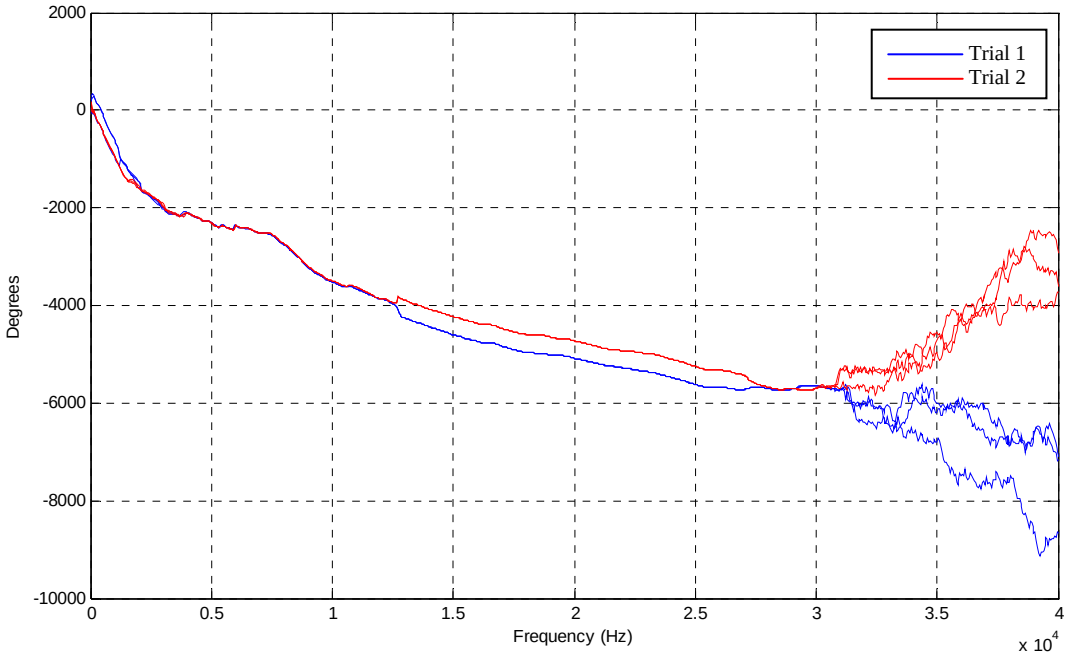

Figure A.30. Water-saturated glass bead specimen 2: analysis of unwrapped phase angles of 0 - 30 kHz sweep, showing three repetitions each for trials 1 and 2; 1000 recordings averaged per repetition.

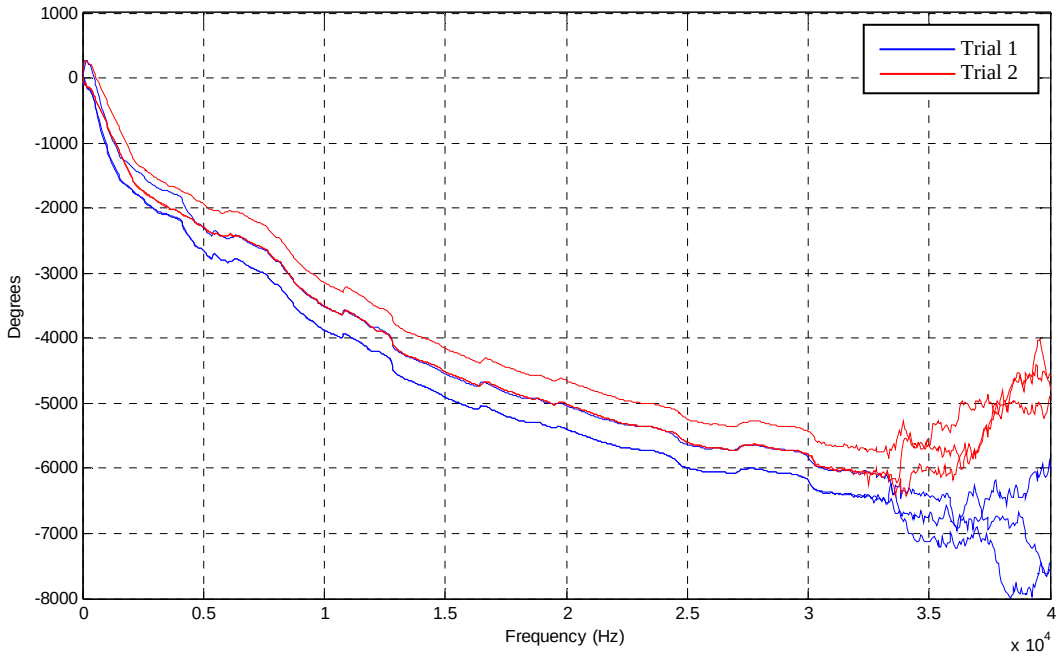

Figure A.31. Water-saturated glass bead specimen 3: analysis of unwrapped phase angles of 0 - 30 kHz sweep, showing three repetitions each for trials 1 and 2; 1000 recordings averaged per repetition.

APPENDIX 3 BACKGROUND SIGNAL ANALYSIS

The background signal in the absence of any actuated pulse signal was recorded to quantify the extent to which the residual energy from a preceding pulse would affect the onset of the following pulse. This was demonstrated by comparing the quiet time in-between pulses to the background signal in the absence of any pulse.

To record the background signal, the equipment was connected in the same manner as described in section 2.5, except the coaxial cable connected to the BNC cable from the receiver bender element was disconnected. Therefore with no receiver bender element connected to the dynamic signal analyzer, what was received was the background signal (noise) within the wires and equipment of the system. It should be noted that this background study was not conducted with the same bender elements used for the testing; these bender elements were the same type as those used for the testing, but were newly wired and prepared.

The isolated background signals were recorded for three repetitions, with 1000 recordings averaged per repetition. The received signals from the baseline testing with essentially saturated glass bead trials presented in Chapter 7 were used for comparison with the isolated background signals. Figure A3.1 shows the received 8 kHz pulse signals (shown in Fig. 7.3) and Figure A3.2 shows the received 1 kHz pulse signals (shown in Fig. 7.4), each overlaid on the background signal to compare the difference in amplitude, where the impact of the residual energy from the preceding pulse on the onset of the following can be visualized.

To quantify the differences present between the background and the effects of the residual pulse energy, the signal amplitudes from the data points of the three repetitions were compared from time 10 ms to 15 ms; 10 ms is the midpoint between the two pulses and time 15 ms is the point of actuation of the second pulse. Table A3.1 presents average and maximum amplitude differences between the isolated background signal and the background signal in-between actuated 8 kHz pulses and 1 kHz pulses for the above mentioned interval. The results show the maximum difference recorded for the 8 kHz pulse was 6.69E-1 V and the maximum difference recorded for the 1 kHz pulse was 8.81E-1 V. The average amplitude difference for both the 8 kHz and 1 kHz pulses ranged from 7.86E-5 V to 8.86E-5 V.

The maximum amplitude difference established for the 8 kHz pulse is larger than the amplitudes of the slow P-wave arrival picks that were made during testing. The differentiation between the background noise and a slow P-wave arrival was made by considering the change in frequency which led to the amplitude gain, and showed deviation from the background signal. The maximum amplitude difference established for the 1 kHz pulse is minuscule when compared to the S-wave arrival; the S-wave arrival was also differentiable by its shape.

The difference in amplitude between the isolated background signal and the background signal in-between pulses can be reduced by increasing the interval between pulses, and further refining signal filtering and processing as mentioned in the recommendations section of the report to minimize these effects on received signals.

Table A3.1. Difference between isolated background signal and background signal in-between actuated pulse signals

Signal	Difference	Δ R1 (V)	Δ R2 (V)	Δ R3 (V)
8 kHz	Average	8.80E-05	8.86E-05	7.86E-05
	Maximum	6.69E-01	7.00E-01	6.82E-01
1 kHz	Average	8.80E-05	8.86E-05	7.86E-05
	Maximum	8.75E-01	8.81E-01	8.61E-01

ΔR1, 2 and 3 indicate the difference between amplitudes of the isolated background signal and the background signal in the presence of actuated signals for three repetitions.

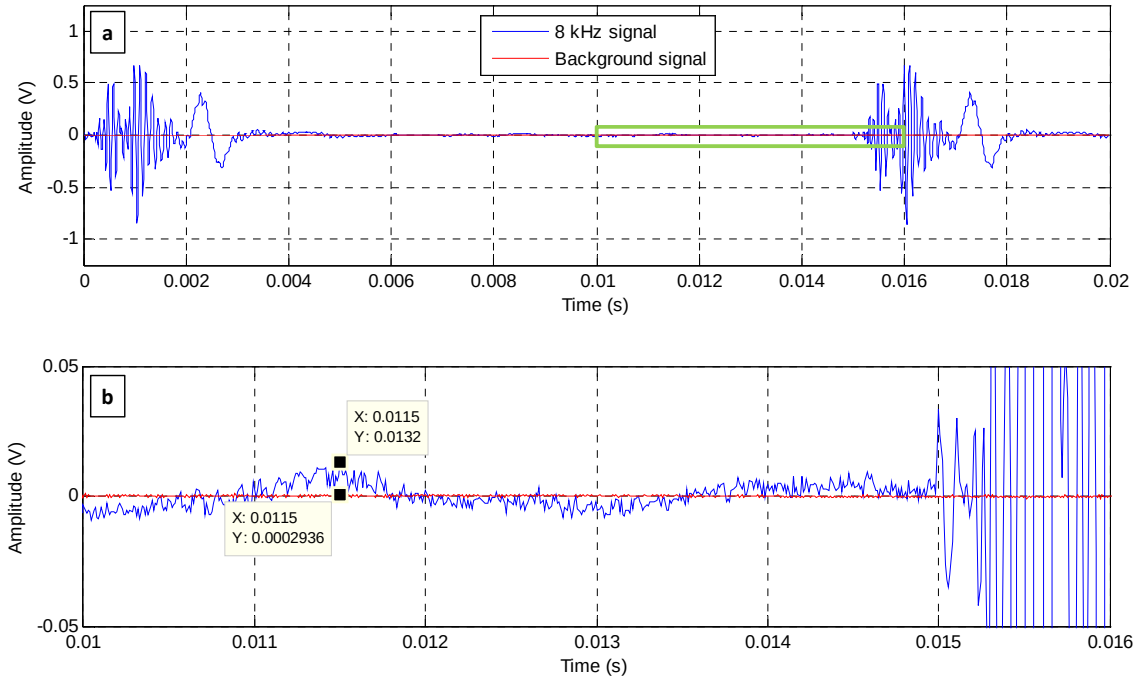

Figure A3.1. 8 kHz sine pulses (200 Hz high pass filter) overlaid on the isolated background signal (no filter). Each signal is a single repetition of 1000 recordings averaged.
a. Received signals showing two consecutive pulses and quiet time between pulses;
b. Detailed view of residual effects on the isolated background signal

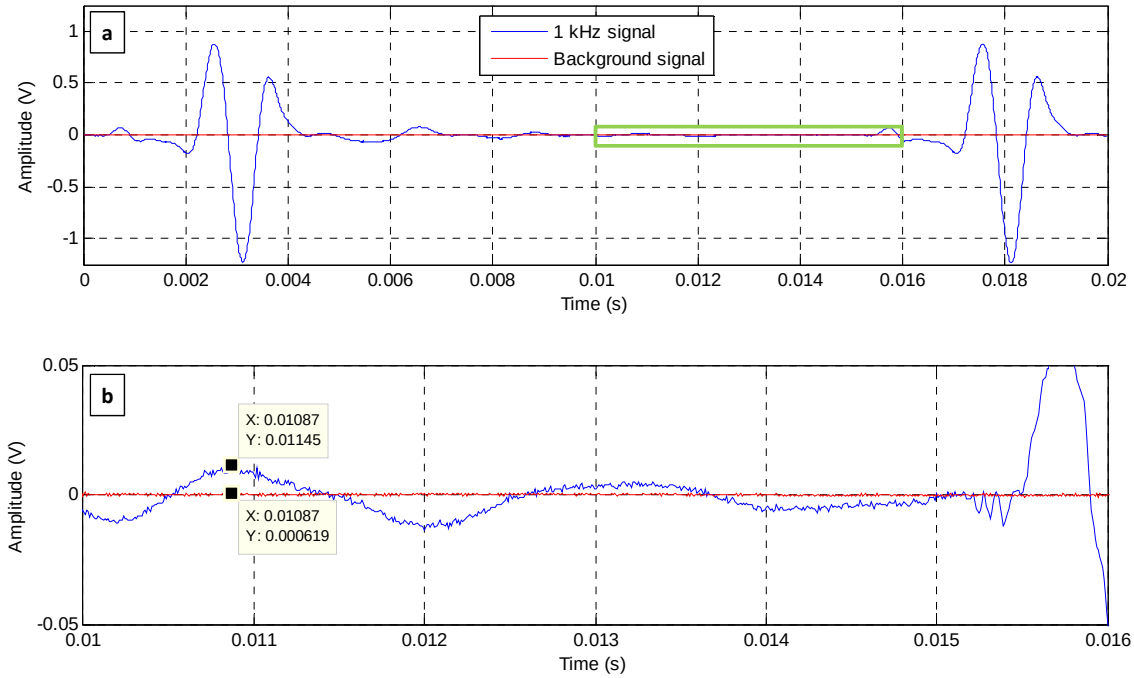

Figure A3.2. 1 kHz sine pulses (200 Hz high-pass filter) overlaid on the isolated background signal (no filter). Each signal is a single repetition of 1000 recordings averaged.
a. Received signals showing two consecutive pulses and quiet time between pulses;
b. Detailed view of residual effects on the isolated background signal

REFERENCES

Arroyo, M., Wood, D. M., and Greening, P. D. (2003). Source near-field effects and pulse tests in soil samples. Geotechnique, 53(3), 337-345.

Arulnathan, R., Boulanger, R. W., and Riemer, M. F. (1998). Analysis of bender element tests. Geotechnical Testing Journal, 21(2), 120-131.

Biot, M. A. (1956). Theory of propagation of elastic waves in fluid saturated porous solid. Journal of the Acoustical Society of America. 28(2), 168-191.

Birkholz, M. (1995). Crystal-field induced dipoles in heteropolar crystals II: Physical significance. The European Physical Journal B, 96(3), 333-340.

Blewett, J., Blewett, I. J., and Woodward, P. K. (1999). Measurement of shear-wave velocity using phase-sensitive detection techniques. Canadian Geotechnical Journal, 36(5), 934-939.

Brignoli, E. G. M., Gotti, M., and Stokoe, K. H. (1996). Measurement of shear waves in laboratory specimens by means of piezoceramic transducers. Geotechnical Testing Journal, 19 (4), 384-397.

Clayton, C. R. I., Theron, M., and Best, A. I. (2004). The measurement of vertical shear-wave velocity using side-mounted bender elements in the triaxial apparatus. Geotechnique, 54(7), 495-498.

Conlon, M., (2009). EPA science in action: Nanotechnology research program, National Exposure Research Laboratory, EPA Office of Research and Development. Retrieved 11/30/09, from http://www.epa.gov/nanoscience/quickfinder/pdf/nanotech_nanomaterials.pdf

Da Fonseca, A. V., Ferreira, C., and Fahey, M. (2008). A framework interpreting bender element tests, combining time-domain and frequency-domain method. Geotechnical Testing Journal, 32(2), 91-107.

Deniz, R. O. (2008). Bender elements and bending disks for measurement of shear and compression wave velocities in large sand specimens. Master's Thesis, Northeastern University, Boston, MA.

Dyvik, R., and Madshus, C. (1986). Lab measurements of Gmax using bender elements. Publication - Norwegian Geotechnical Institute, 161 pp.

Dyvik, R., and Olsen, T. S. (1991). G_{max} measured in oedometer and DSS tests using bender elements. Publication - Norwegian Geotechnical Institute, 181 pp.

Greening, P. D., and Nash, D. F. T. (2004). Frequency domain determination of G0 using bender elements. Geotechnical Testing Journal, 27(3), 288-294.

Jovičić, V., Coop, M. R., and Simić, M. (1996). Objective criteria for determining Gmax from bender element tests. Geotechnique, 46(2), 357-362.

Joyce,R.A., Glaser,D.R., Werkema Jr.,D.D., Atekwana,E.A., Spectral induced polarization response to nanoparticles in a saturated sand matrix, *Journal of Applied Geophysics*, doi:10.1016/j.jappgeo.2011.11.009, 2011.

Lee, J., and Santamarina, J. C. (2005). Bender elements: Performance and signal interpretation. Journal of Geotechnical and Geoenvironmental Engineering, 131(9), 1063-1070.

Lee, C., Lee, J.S., Lee, W., and Cho, T. H. (2007). Experiment setup for shear wave and electrical resistance measurements in an oedometer. Geotechnical Testing Journal, 31(2).

Leong, E. C., Yeo, S. H., and Rahardjo, H. (2005). Measuring shear wave velocity using bender elements. Geotechnical Testing Journal, 28(5), 488-498.

Nakagawa, K., Soga, K., and Mitchell, J. K. (1996). Pulse transmission system for measuring wave propagation in soils. Journal of Geotechnical Engineering, 122(4), 302-308.

Nakagawa, K. Soga, K. and Mitchell, J. K. (1997). Observation of Biot compressional wave of the second kind in granular soils. Geotechnique, 47(1), 133-147.

National Nanotechnology Initiative (2009). What is nanotechnology? Retrieved 12/04/09, from http://www.nano.gov/html/facts/whatIsNano.html

Patel, A., Bartake, P.P., and Singh, D.N. (2009). An empirical relationship for determining shear wave velocity in granular materials accounting for grain morphology. Geotechnical Testing Journal, 32(1), 1-10.

Piezo Systems, I. (2009). History of piezoelectricity. Retrieved 11/20/09, from http://www.piezo.com/tech4history.html

Plona, T. J. (1980). Observation of a second bulk compressional wave in a porous medium at ultrasonic frequencies. Applied Physics Letters, 36, 259-261.

Plona, T. J., D'Angelo, R., and Johnson, D. L. (1990). Velocity and attenuation of fast, shear and slow waves in porous media. Ultrasonics Symposium Proceedings, Institute of Electrical and Electronics Engineers Inc. (IEEE), Piscataway, NJ, 3, 1233-1239.

Rajabdeen, M. N., Luke, B., Werkema, D., and Glaser, D. (2011). Application of piezoceramics in characterizing granular media. Engineering Geology and Geotechnical Engineering Symposium, eds. Biggar, N., Luke, B., and Werle, J. Idaho State University, Pocatello, 490-496.

Reynolds, G. (2000). The fundamentals of signal analysis. Agilent Technologies. Application note 243.

Rio, J. F. M. E. (2006). Advances in laboratory geophysics using bender elements. Dissertation, University College London, UK.

Santamarina, J. C., Klein, K. A., and Fam, M. A. (2001). Soils and waves – particulate materials behavior, characterization and process monitoring, John Wiley and Sons, New York.

Sengpiel, E. (2010). Sengpielaudio, Speed of sound in air calculation and temp – air. Retrieved 11/04/10, from http://www.sengpielaudio.com/calculator-speedsound.htm

Viggiani, G., and Atkinson, J. H. (1995). Interpretation of bender element tests. Geotechnique, 45(1), 149-154.

Wang, Y. H., Lo, K. F., Yan, W. M., and Dong, X. B. (2007). Measurement biases in the bender element test. Journal of Geotechnical and Geoenvironmental Engineering, 133(5), 564-574.

Williams, K. H., Ntarlagiannis, D., Slater, L. D., Dohnalkova, A., Hubbard, S. S., and Banfield, J. F. (2005). Geophysical imaging of stimulated microbial biomineralization. Environmental Science and Technology, 39(19), 7592-7600.

Zeng, X., and Ni, B. (1998). Measurement of G_{max} under anisotropic loading condition using bender elements. Geotechnical Earthquake Engineering and Soil Dynamics III, ed. P. Dakoulas and M. Yegian. Geotechnical Special Publication 75(1), 189-200. American Society of Civil Engineers, Reston, VA.

Zhihai, X., Ping, T., Zhidong, J., Zhicheng, G., and Liming, W. (2008). Eliminate corrosion on grounding system by a conductive RTV silicone coating. Annual Report - Conference on Electrical Insulation and Dielectric Phenomena 49-51, Institute of Electrical and Electronics Engineers Inc. (IEEE), Piscataway, NJ.

United States
Environmental Protection
Agency

Office of Research
and Development (8101R)
Washington, DC 20460

Official Business
Penalty for Private Use
$300

EPA/600/R-12/547
June 2012
www.epa.gov

Please make all necessary changes on the below label, detach or copy and return to the address in the upper left hand corner.

If you do not wish to receive these reports CHECK HERE ☐; detach, or copy this cover, and return to the address in the upper left hand corner.

PRESORTED STANDARD
POSTAGE & FEES PAID
EPA PERMIT No. G-35